EXPERIMENTAL STUDIES ON RESISTIVE-WALL INSTABILITY AND DEVELOPMENT OF BEAM DIAGNOSTICS FOR THE UNIVERSITY OF MARYLAND ELECTRON RING FACILITY

by

Yun Zou

Dissertation submitted to the Faculty of the Graduate School of the
University of Maryland at College Park in partial fulfillment
of the requirements for the degree of
Doctor of Philosophy
2000

Advisory Committee:
Professor Martin Reiser, Chair/ Advisor
Professor Patrick O'Shea, Co-Advisor
Professor Chuan Liu
Professor Derek Boyd
Professor Jon Orloff

Abstract

Title of Dissertation: EXPERIMENTAL STUDIES ON RESISTIVE-WALL INSTABILITY AND DEVELOPMENT OF BEAM DIAGNOSTICS FOR THE UNIVERSITY OF MARYLAND ELECTRON RING FACILITY

Yun Zou, Doctor of Philosophy, 2000

Dissertation directed by: Professor Martin Reiser

Professor Patrick O'Shea

Electrical and Computer Engineering Department

In this thesis, experimental studies are presented on the resistive-wall instability in space-charge dominated beams. Localized perturbations are used to produce the space-charge waves. The growth rate or decay rate of the longitudinal energy width associated with the space-charge waves is studied using retarding voltage energy analyzers. The energy width is measured at both the entrance and exit of the resistive transport channel and the two measurements are compared to calculate the growth or decay rate of the space-charge waves. The experiments are performed in both linear and nonlinear regimes. In the linear regime, we observed that the energy width of the slow wave grows while the energy width of the fast wave decays. In the nonlinear regime, we found that the decay rate of the energy width associated with the fast wave depends on the perturbation strength. The

decay rate gets smaller with larger perturbation. If the perturbation is large enough, this decay rate crosses the zero point and becomes positive, which means that the energy width of the fast wave increases. The experiments are also double-checked with a conducting tube in place of the resistive tube, in which case no growth or decay of the space-charge waves occurs, as expected.

Energy spread measurements of the electron beams in the range of several keV are very difficult and tricky. If not well taken, divergence in the beam trajectories will lead to poor resolution of the energy analyzer. In this thesis, we report about the design and performance of a new energy analyzer with significantly improved resolution compared to the analyzer used earlier. The energy spread of electron beams emitted from an electron gun have been measured and compared to the theory of Coulomb scattering, the major source of energy spread increase in such electron beams. Much better agreement was achieved than in previous experiments with the first analyzer.

We also report on work performed to develop a capacitive beam position monitor (BPM), which will be used to measure and correct the beam centroid motion in the University of Maryland Electron Ring (UMER) under construction. A prototype capacitive BPM has been built and bench tested. The results show that this kind of BPM can meet the requirements of the UMER.

Lastly, we present design studies of a low-inductance, fast rise-time dipole for rapid single-turn beam injection into UMER. A prototype dipole has been built.

The test of the prototype agrees with the simulation and theory very well. It provides valuable information for the final engineering design of this device.

Dedication

To my lovely wife

Acknowledgements

My Ph.D. dissertation work would not be successful without the contributions from many people. I would like to thank them there.

First of all, I would like to thank Professor Martin Reiser for his professional advice and guidance during my tenure as a graduate student. His enthusiasm and encouragement have greatly motivated me to finish my Ph.D. work. I would also like to thank Dr. JG Wang for his tremendous help in both the theoretical and experimental part of my dissertation. I would like to thank Professor Patrick O'Shea. He became my co-advisor at the final stage of my Ph.D. project and has contributed with valuable advice and criticism to my work. I would like to express my thanks to Dr. Rami Kishek, the assistant manager for UMER, for useful discussions. I am thankful to Dr. Santiago Bernal for his valuable help in my experiment and in the final polishing of my dissertation. I would like to thank Dr. Hyyong Suk, the former graduate student whose work I continued, for transferring his knowledge of the facility and of the resistive-wall experiment to me. I am also grateful to Victor Yun, who, with his professional expertise, provided invaluable help in the mechanical design of the energy analyzer and the BPMs.

I am also grateful to Prof. Chuan Liu, Prof. Derek Boyd, Prof. Jon Orloff for serving on the advisory committee. I would thank Dr. Irving Haber at NRL, Drs. David Kehne and Terry Godlove at FMT for their helpful advice and

discussions about the resistive-wall experiment and the development of the diagnostic tools.

Table of Contents

List of Tables

List of Figures

Chapter 1

Introduction

1.1 Historical Background

Charged-particle beams have been used in many diverse applications, such as in electron microscopes, cathode ray tubes (CRT) and accelerators [1]. Unlike electrons in solids, charged particles in vacuum cannot be contained unless there are external applied magnetic or electric focusing forces. The divergence of charged-particles beams is due to the thermal energy, characterized by the emittance in the beam physics and the repulsive space-charge force between beam particles. The particle beams in these traditional devices mentioned above are in the emittance-dominated regime, which means that the thermal energy in the beam is larger than space-charge energy of the beam. On the other hand, recent applications, such as induction linacs for heavy-ion fusion (HIF) [2], free electron lasers [3], spallation neutron sources and high power microwave tubes, are in the space-charge dominated regime. The quantitative definition of this concept will be given in the next section.

The physics of low intensity beams, or electron optics, dates back to the early 1920's and the theory is very well known. However, the physics in space-

charge dominated beams is relatively new and much more complex. Due to the nonuniform density of the beams and other nonlinearity of the devices used in the beam line, a non-linear, self-consistent theory has to be developed to model the beam.

At the University of Maryland, theoretical and experimental work has been carried out for some time to study the space-charge dominated beams. Prof. Reiser's book covers extensively the studies during the last three decades on the physics of space-charge dominated beams [1]. Many graduate students have conducted pioneering research work, such as the experiments on matched and mismatched beams, on longitudinal dynamics and instability in space-charge dominated electron beams, where Dr. J.G. Wang has played an important role as Research Scientist. [4-7].

Even though significant progress has been made in the past years, many interesting topics still require new experimental and theoretical research. The resistive-wall instability is one example. It was first studied by Birdsall for the application of microwave generation [8]. Recently, because this instability may cause beam deterioration in the linear induction accelerators for HIF, new research has been conducted to study it. In this dissertation, experimental work has been carried out to study the interaction of localized space-charge waves with a resistive wall in both linear and nonlinear regimes for electron beams with energies of 2-10 keV and beam currents of 10-100 mA. The parameters of these electron beams

scale with those required for heavy ion fusion drivers. The main advantage of using electron beams is the fact that the growth or decay rates for the slow and fast space-charge waves can be measured over a distance of about 1 m while the e-folding distance in a heavy ion fusion driver would be hundreds of meters.

Energy spread of the charged particle beam is another interesting topic and has many applications. For example, in ion microscopy, large energy spread will prevent the beam from being focused into a small spot [9]. Cold electron beams are used to cool ion beams so that their energy spread and transverse temperature becomes very low[10-12]. Photoemission from semiconductors is also a promising technique to produce this kind of beam. However, the longitudinal cooling of electron beams (as well as ion beams) during acceleration results in a significant increase of the energy spread due to thermal equipartitioning via Coulomb collisions. Two effects are responsible for this increase of the longitudinal beam energy spread. One is the Boersch effect, which transfers thermal energy from the transverse direction into the longitudinal direction. Another effect is longitudinal-longitudinal relaxation, which is related to nonadiabatic acceleration. In this dissertation, we report about the results of experiments to measure the energy spread increase of an electron beam and compare the results with the theory. A new energy analyzer, which has much better resolution than the previous one, has been designed and tested in this work.

Besides the pure physics, good engineering design is needed for the successful implementation of the theory. At the University of Maryland, a small electron ring (UMER) is being built for beam physics studies in the space-charge dominated regime of a circular machine. As a part of this dissertation, a prototype capacitive beam position monitor (BPM) has been designed and tested. Also, work has been performed to study a low-inductance, fast rise-time dipole for rapid injection of the electron beam into the ring.

1.2 Terminology and Basic Theory of Beam Physics

1.2.1 K-V (Kapchinsky-Vladimirsky) Distribution

The K-V model has been one of the most important concepts in accelerator theory and design. In this model, the space-charge force is linear and the beam phase-space area remains constant. For the forces to be linear in the transverse direction, an electron beam must be in paraxial motion and the changes in the beam size occur slowly so that the longitudinal forces be negligible.

Under this condition, the beam envelope equation in the focusing channel can be written as

$$\frac{d^2R}{dz^2} + k_0(z)R - \frac{K}{R} - \frac{e^2}{R^3} = 0. \qquad (1.1)$$

Here, z is the axial distance and R is the beam envelope. K is the generalized beam perveance defined by

$$K = \frac{I}{I_0}\frac{2}{(bg)^3}, \qquad (1.\ 2)$$

where I is the beam current and I_0 is the characteristic current given by

$$I_0 = \frac{4pe_0mc^3}{q}. \qquad (1.3)$$

Here, m is the particle mass, c is the speed of light and q is the particle charge. For electrons, $I_0 \cong 17000$ A.

In (1.1), $\kappa_0(z)$ is the external focusing function, which for the solenoids used in our experiments is given by

$$k_0(z) = \left(\frac{qB_z(z)}{2mcbg}\right)^2. \qquad (1.\ 3)$$

The K-V model does not make any assumption about whether the beam is space-charge dominated or emittance dominated. So we can use this as a means to determine which force is stronger. In equation (1.1), the K/R term is related to the space-charge force and ε^2/R^3 represents the defocusing force due to beam emittance (temperature). Taking the ratio of these two terms, we have

$$D = \frac{e^2/R^3}{K/R} = \frac{e^2}{KR^2}. \qquad (1.\ 4)$$

If D>1, then the beam is emittance dominated, if D<1, it is space-charge dominated.

1.2.2 Beam Emittance

When electron particles are emitted from the source, they are emitted with different initial magnitude and direction of the velocity. This random thermal motion of the electrons in the beam causes an intrinsic beam energy spread. When the beam is accelerated and transported through a focusing channel, the transverse and longitudinal velocity spread will increase further and the beam quality will deteriorate due to Coulomb collision or nonlinear forces. The figure of merit for the transverse beam quality is the emittance.

The motion of each particle in the beam is characterized by the trajectory in 6-dimensional phase space, as defined by the three spatial coordinates (x, y, z) and three mechanical momentum coordinates (P_x, P_y, P_z) as a function of time. For a charged particle beam in accelerators and transport channels, it is convenient to separate the four-dimensional transverse phase space from the two-dimensional longitudinal phase space. Furthermore, the transverse motion of the particles is commonly defined by the positions x(z), y(z) and the slopes x'(z) and y'(z), where $x'=v_x/v_z$. In a K-V distribution, all forces on the particles are linear and the projection of the 4-D beam trace space on any 2-D plane, i.e. x-y, x-x', y-y' and x'-y' plane, is an ellipse with uniform particle density. The area of the ellipse

$$A_x = \iint dx dx' \qquad (1.5)$$

is related to the beam emittance by

$$e_x = x_m (x')_m = A_x / p \qquad (1.6)$$

Here, x_m and $(x')_m$ are the maximum particle position and divergence in an upright ellipse, respectively. Identical relations hold for the y-y' plane. The ideal emittance of a K-V beam is convenient to use. However, this model does not characterize the beam quality well if the beam trace space is distorted or the beam edge is not well defined due to nonlinear forces. In this case, the rms emittance gives better information on the beam quality. The rms emittance $\tilde{e}_x$ is defined by

$$\tilde{e}_x = (\overline{x^2}\,\overline{x'^2} - \overline{xx'}^2)^{1/2}. \qquad (1.7)$$

Here, the bar on the top of the terms indicates second moments of the distribution, e.g. $\overline{x^2} = \int x^2 f(x, y, x', y') dx dy dx' dy'$. The second term $\overline{xx'}^2$ in the bracket enters into the relation when the trace space ellipse is tilted (expanding or converging beam). From the equation, we can see that the rms emittance is directly related to the second moments of the beam distribution. If the beam is described by the K-V model, then the K-V emittance and the rms emittance are simply related by

$$e_x = 4\tilde{e}_x. \qquad (1.8)$$

Because of this relation for a K-V beam, it is useful to adopt the four-times rms emittance also for other beam models as well as for real beams in experiments. The emittance e_x is therefore defined as the "effective" emittance [1]. In a K-V beam,

the effective emittance comprises all particles. In most other distributions, typically more than 90% of the particles are within the effective emittance.

1.3 Organization of the Dissertation

This dissertation consists of two main parts. The first part describes the study of the longitudinal instability in a resistive-wall environment. Chapter 2 describes the facility setup of the experiment for the resistive-wall instability. Chapter 3 presents the theory and background of the resistive-wall instability and the experimental results in both linear and nonlinear regimes.

In the second part of the dissertation, the development of diagnostic tools for the University of Maryland Electron Ring (UMER) is presented. Chapter 4 describes the design, simulation and beam test of a retarding voltage energy analyzer. The general theory for designing this kind of device is also presented in this chapter. The energy spread of electron beams emitted from an electron gun is measured at different beam energies and the results are compared to the predictions from the Boersch effect and longitudinal-longitudinal relaxation. In Chapter 5, a prototype beam position monitor (BPM) is designed and bench tested. In this chapter, the principle of developing a fast rise-time dipole is also discussed.

Chapter 2

Facility for the Resistive-Wall Instability Experiments

2.1 Experimental Setup

Figure 2.1 shows the experimental setup for the resistive-wall instability experiment. The facility consists of an electron gun, three matching solenoids, a long solenoid channel and two diagnostic chambers. The beam is emitted from the electron gun with various beam energies. The beam pulse shape is controllable, either rectangular or parabolic. Usually we use a rectangular profile. On the flat top of the beam, a localized perturbation can be launched by the method which will be described in the next section. Three matching solenoids can be adjusted so that the beam is matched into the long solenoids. Inside the long solenoids there is a resistive tube for the study of the resistive wall instability. There are several diagnostic tools employed in this experiment. They are beam current monitors, phosphor screens, a Rogowski coil and energy analyzers.

2.2 Electron Gun

The electron gun used in the experiment is a variable-perveance gridded gun developed and constructed at the University of Maryland [13]. The electron has a Pierce type geometry and a planar configuration consisting of the heater, cathode

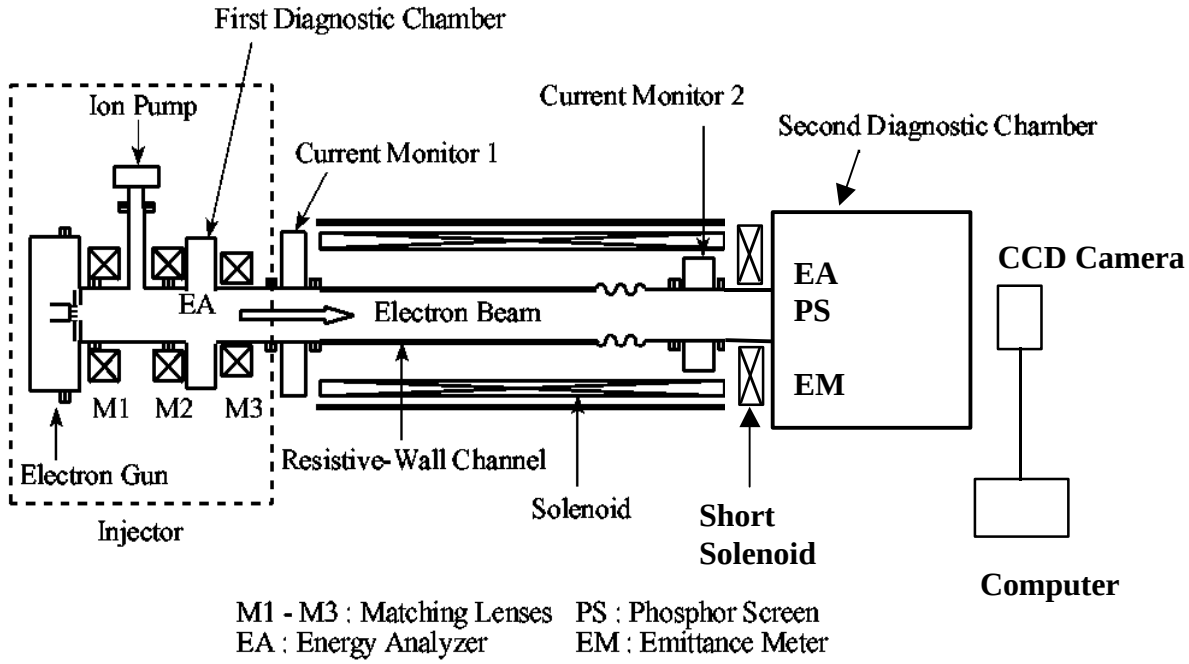

Figure 2. 1. Setup of resistive-wall experiment.

and grid. The cathode is indirectly heated and the heating area is around 0.8 cm^2. Because the heating area is relative small, the heating inhomogeneity is not a problem. The cathode could be heated from room temperature to the working condition in about an hour. The normal heating voltage is around 6.4 V and the heating current is about 1.4 A, which yields a heating power of 4.5 W. The normal heating voltage is suggested by the manufacturer and has to be calibrated for each new cathode. This is critical, because if the temperature is too high, too much material will be evaporated and if the temperature is too low, the emission is decreased. The grid wire is made of tungsten, with diameter of 0.025mm. The screening fraction of the grid is 25.6%. The grid-cathode spacing is 0.11mm, which has small enough capacitance to guarantee a fast rise time.

Figure 2.2 shows the mechanical drawing of the electron gun. The whole cathode assembly is mounted to a support through a bellow. The distance between the cathode and anode is adjustable accurately between 0.93 cm and 2.30 cm, resulting in a beam perveance of 0.22 to 1.35 $\mu A\ V^{-3/2}$. The anode and the field-shaping electrodes form a Pierce geometry. The diameter of the anode aperture is 1 cm. A molybdenum mesh is used to cover the anode aperture to reduce the defocusing effect. The screening factor of the mesh is 14.3%, smaller than the cathode grid. An aperture plate follows down-stream of the anode for the purpose of beam profiling.

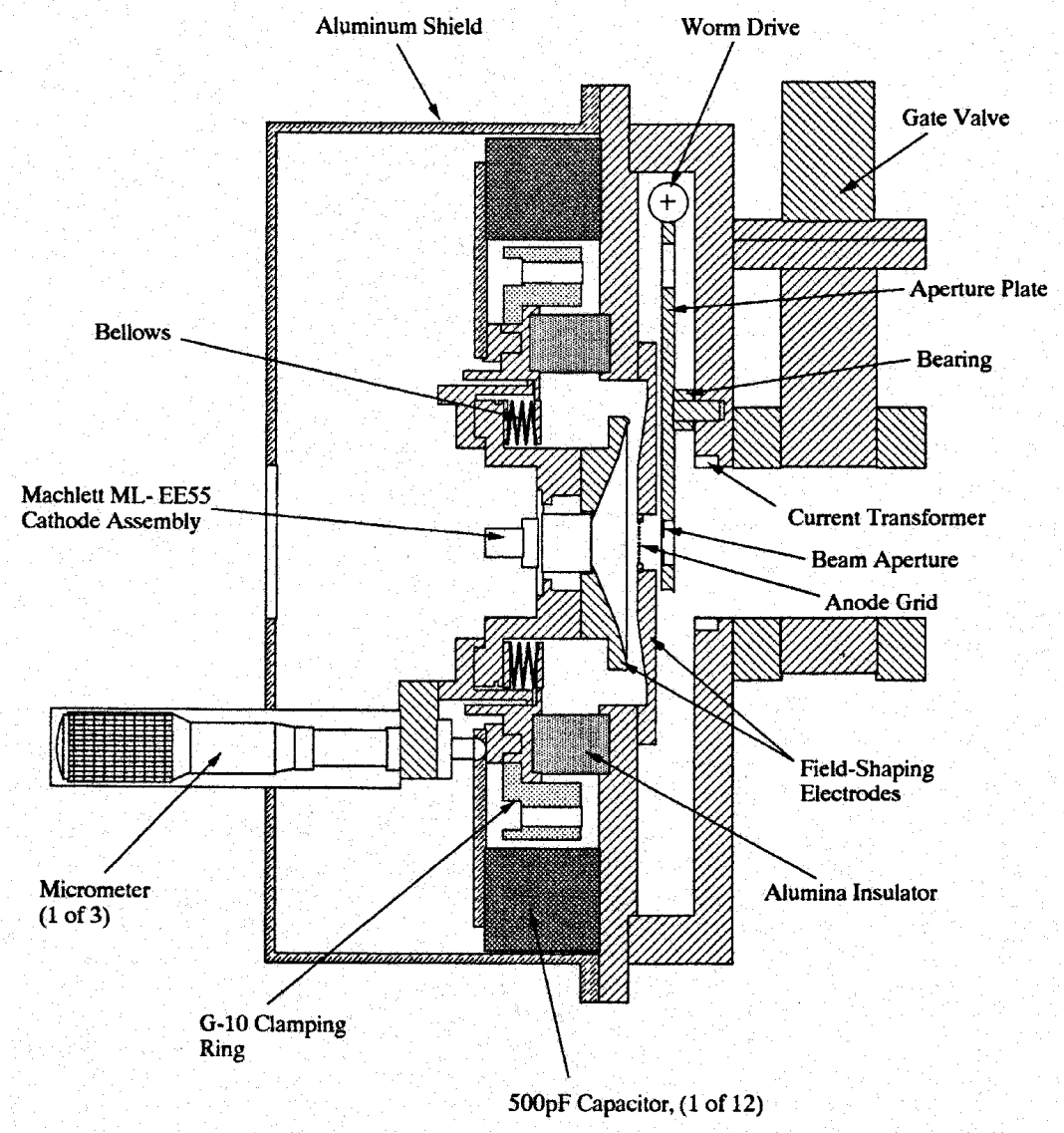

Figure 2. 2. Schematics of gridded electron gun.

It consists of eight circular holes, one pepper-pot, one slit and two multiple-beamlet configurations. A simple, built-in current transformer (Rogowski Coil) is located after the aperture plate. It is very useful in the gun commissioning and emission testing. This gun also has a gate valve to isolate the cathode from the rest of the system. During experiments, the gate valve is open; while after experiment or during the system installation, the gate valve is closed to protect the cathode.

Figure 2.3 shows the circuit diagram of the gun controller. The electronics consists of a high voltage power supply for anode-grid voltage, a DC bias power supply to supply voltage between the cathode and grid to suppress the beam, an AC power supply to heat the cathode and finally, a grid-cathode pulse generator. All the electronics is located in a high voltage deck, which is isolated from the ground up to -10KV. It has a connection to the low voltage electronics via fiber optics and insulated transformer. The cathode is usually biased by positive DC voltage relative to the grid to cut off the beam current. During the emission, the pulse generator produces a negative pulse between the cathode and grid to turn on the beam.

The grid-cathode pulse system is very critical to guarantee a desirable beam waveform. It consists of a charging transmission line, a fast transformer and an avalanche transistor. Careful attention must be taken to choose the parameters of the transformer and the transistor to have fast rise-time pulse. The length of the

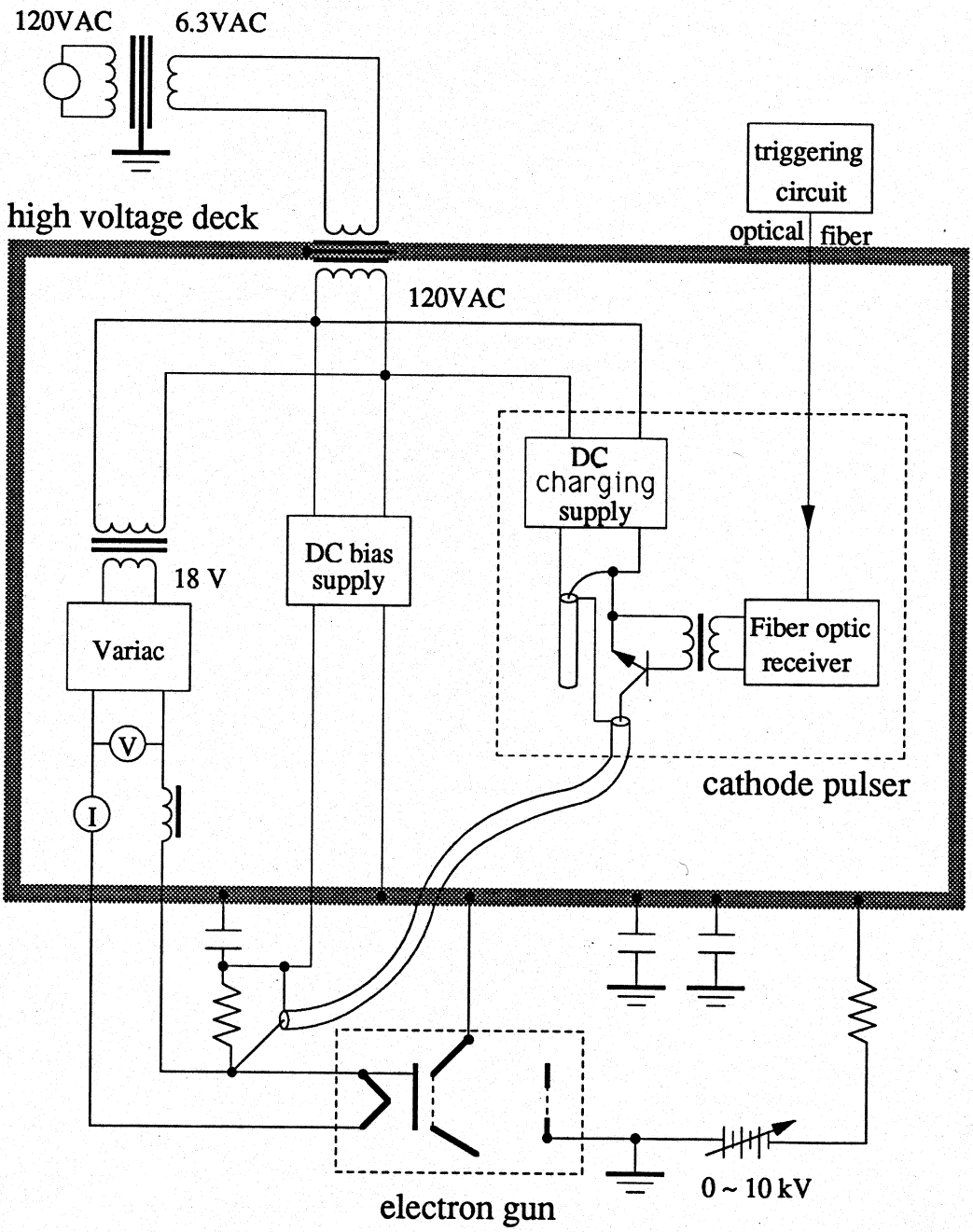

Figure 2. 3. Circuit diagram for electron gun.

transmission line is about 5 m long for a 100 ns long pulse. The transmission line length is variable to produce different length of beam pulse. The actual transmission line consists of two coaxial cables of equal length. The two parts are connected by a T connector and a short transmission line can be added to the T. The purpose of this configuration is to introduce a localized perturbation to the beam current, beam velocity and beam energy. The strength of the perturbation voltage is adjustable by changing the length of the short transmission line. By varying the cathode temperature and A-K distance, one can produce slow or fast localized space-charge waves, which will propagate on the beam and can be used to investigate the interaction with the resistive environment. Figure 2.4 gives a typical grid-cathode pulse with a perturbation in the middle.

The avalanche transistor is triggered by an external pulse, which is produced by a pulse generator and is transmitted to the high voltage deck through a fiber cable. The external trigger can either work in 60 Hz repetition rate or in CW mode for different purposes of experiment. To save the cathode life-time, we usually run it in 60 Hz. Another thing worth noting is that synchronization must be made between the pulse and the AC line voltage such that the beam is emitted when the line voltage is at zero crossing. This can avoid the magnetic field produced by the heating current from affecting the beam.

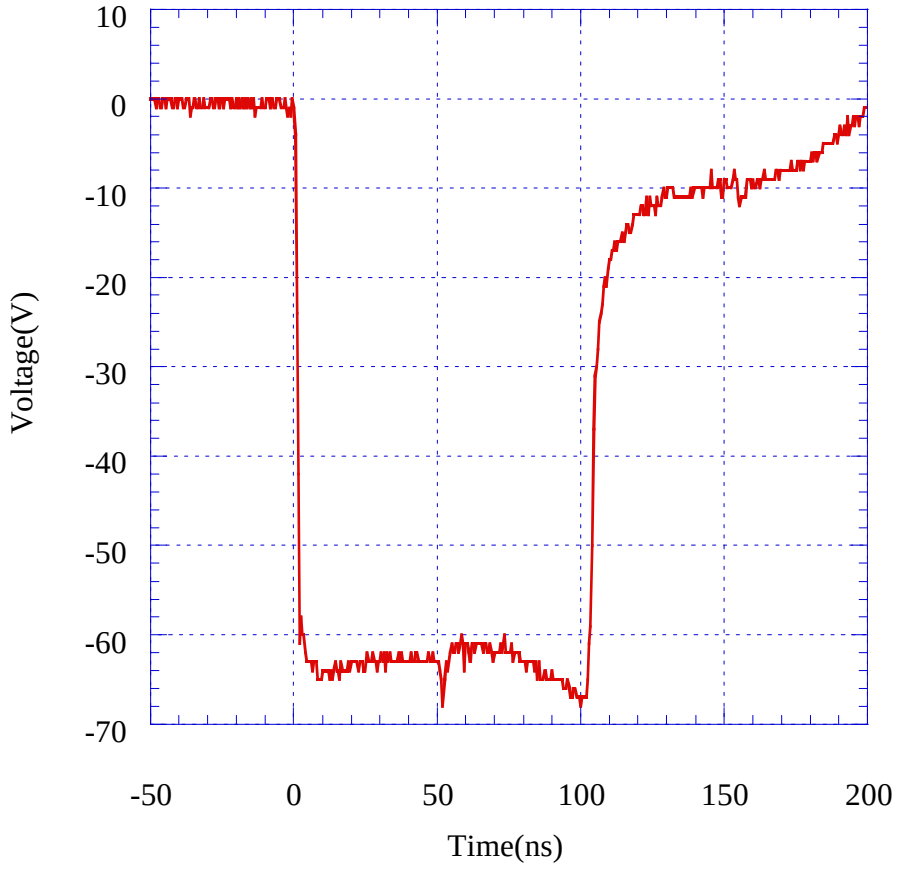

Figure 2. 4. Typical grid-cathode pulse in the electron gun. The bump in the middle is the perturbation introduced intentionally.

2.3 Matching Lenses and Long Solenoid Transport

Downstream of the electron gun are there three matching lenses. The first two solenoids have the same inner diameter of 7.6 cm and the third one has inner diameter of 4.7 cm. Each solenoid has thickness of 6.8 cm. Three DC power supplies are used to power each solenoid so that each of them can be adjusted individually.

These three solenoids are characterized previously [14]. A single formula could be used to represent these lenses. The formula is

$$B_{z0}(z) = B_0 \frac{e^{-\frac{(z-z_0)^2}{2d^2}}}{1+\frac{(z-z_0)^2}{a^2}}. \qquad (2.1)$$

Here, B_0 is the maximum axial magnetic field. z_0 is the center position of the solenoids. d and a are parameters to control the field profile. They are different for each solenoid. Table 2.1 shows all the parameters for three solenoids. In the table, M1, M2 and M3 represent the first, second and third solenoids respectively. B_0 is the peak magnetic field in Gauss per ampere. Figure 2.5 shows the axial magnetic field profile of the first solenoid. In the figure, two lines indicate the physical edge of the solenoid. The fields drop to about 40% at the physical edge and almost zero at 11 cm.

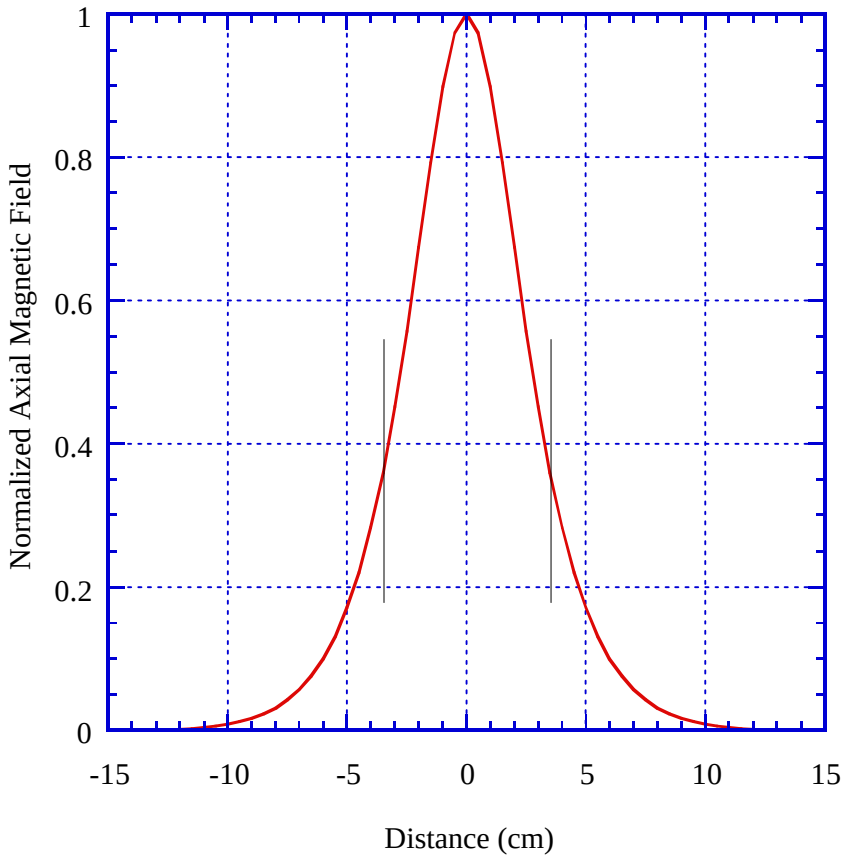

Figure 2. 5. Axial magnetic field profile for the first solenoid. Two lines indicate the physical edges of the solenoid.

Table 2. 1. Parameters for three matching solenoids

Solenoids	B_0 (Gauss/A)	d (cm)	a (cm)
M1	17	4.475	3.422
M2	17	4.168	3.592
M3	20	2.82	3.36

It is worth noting that the field produced by a short solenoid is not a perfect uniform field across the beam section area. Due to the higher order field, the peak magnetic field changes with the radius. If the zero order of the magnetic field is given by Equation (2.1), then the total axial magnetic field including up to forth order could be represented as

$$B_{z4} = B_{z0}(z) - B''_{z0}(z)\frac{r^2}{4} + B''''_{z0}(z)\frac{r^4}{64}. \qquad (2.2)$$

Note that B_{z4} is radius dependent and usually increases with the radius. Figure 2.6 shows the dependence of the peak magnetic field on the radius. In the figure, the field is normalized by B_{z0} at z=0. At r=0, the field is equal to B_{z0}, and it increases by about 5% in one centimeter. This nonlinear effect will change the beam envelope calculation slightly.

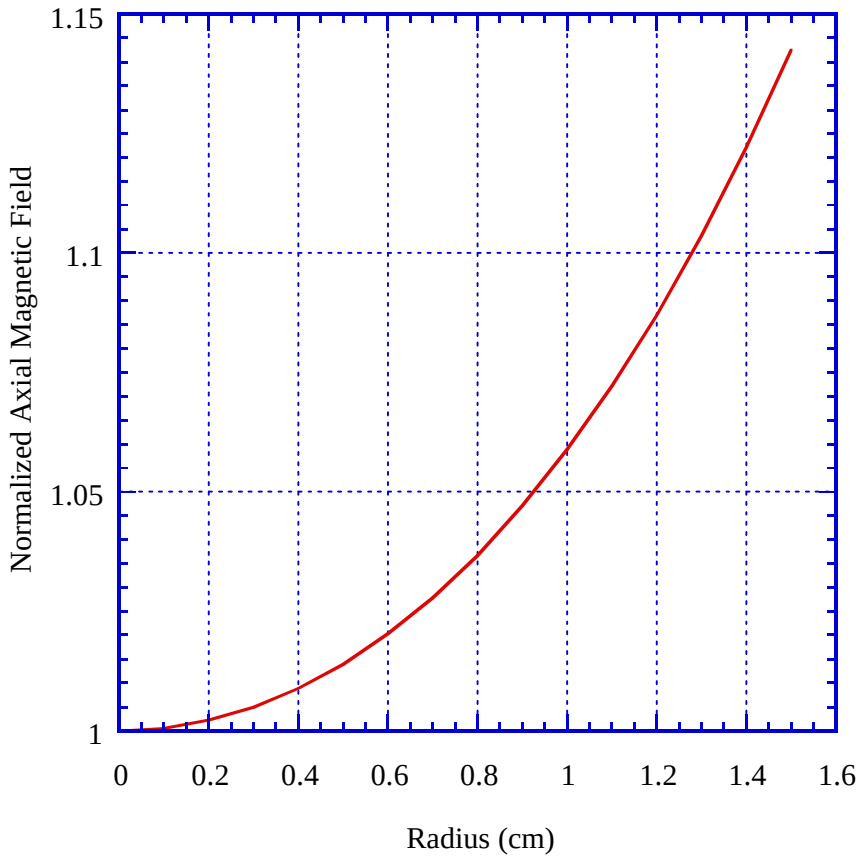

Figure 2. 6. Solenoid axial field vs. radius including upto 4th term.

After three matching lenses is a long solenoid, which offers uniform focusing to the beam. The solenoid is 138.7 cm long. It is made of copper windings on an aluminum tube with diameter of 11.5 cm. There is an iron tube at the outside of the copper windings to restrict the field lines. The axial magnetic field is uniform inside the solenoid. However, at the edges, the fields decay with the distance. For the purpose of simulating the beam envelope, we have to measure the field profile at the edges. The fields are measured by a Bell gaussmeter with a longitudinal Hall probe. Figure 2.7 shows the measured axial magnetic field profile along the axis. The horizontal axis is the distance along the solenoid and zero position is the physical edge of the solenoid. The circles represent measurement points. Fitting curve is also shown in the figure. The fitted formula for the field profile is

$$B_z(z) = B_0 c\left(\frac{z}{(z^2 + a^2)^{1/2}} - \frac{z-l}{((z-l)^2 + a^2)^2}\right). \qquad (2.3)$$

Here, c, a and l are empirical parameters for best fitting. Their numbers are c=0.5027, a=5.0408 cm and l=137.08 cm respectively for this long solenoid. B_0 corresponds to the uniform field inside the solenoid. It depends on the beam current and the solenoid winding. Figure 2.8 shows the dependence of B_0 on the solenoid current. The round points are the measurement data and the line is the fitting curve. The fitted formula for B_0 is

$$B_0 = -0.1296 + 7.4152 \times I. \qquad (2.4)$$

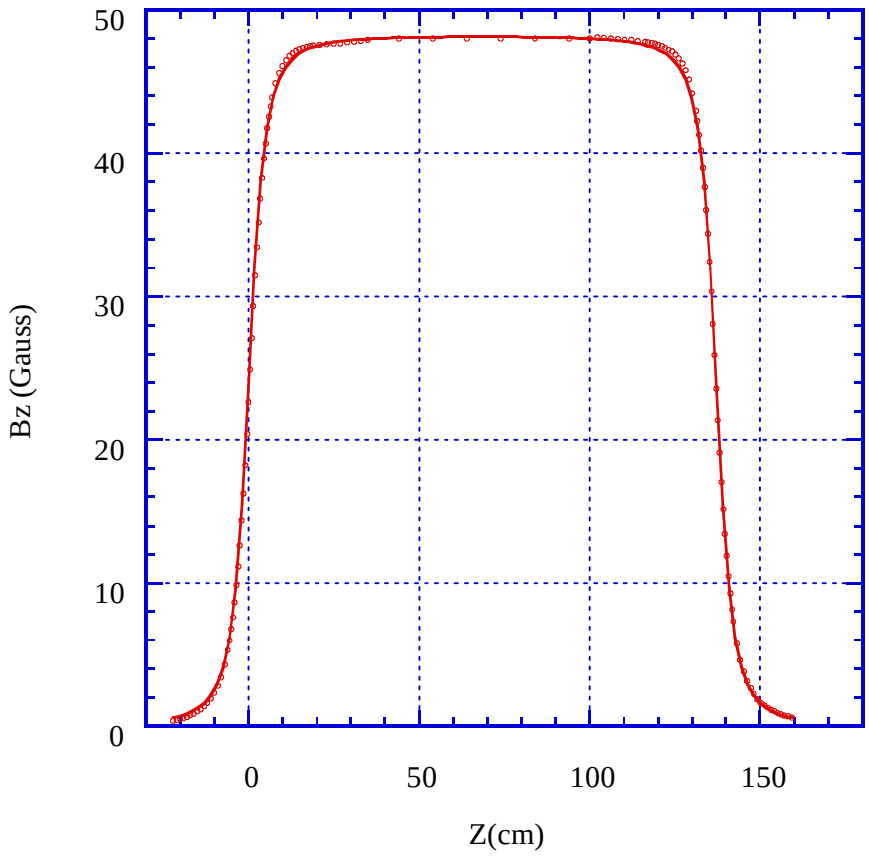

Figure 2. 7. Axial magnetic field produced by the long solenoid.

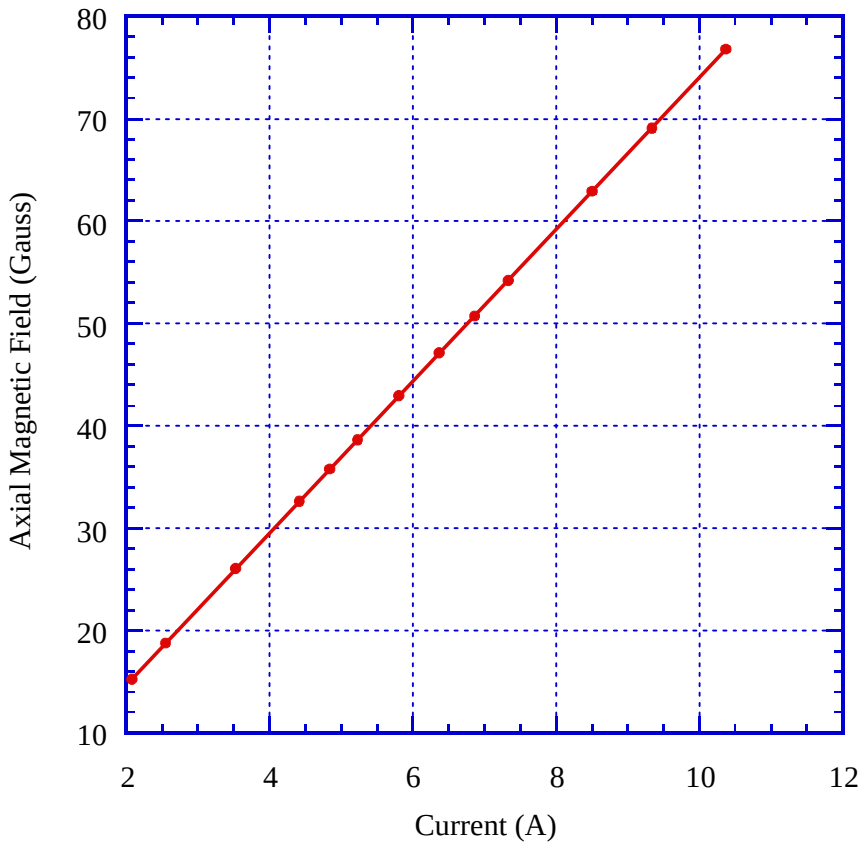

Figure 2. 8. Peak axial magnetic field of the long solenoid vs current.

Here the unit for B_0 is Gauss and I is the solenoid current, in amperes.

Due to the physical limitation, there is a gap between the exit of the long solenoid and the entrance of the diagnostic chamber. To prevent the beam from blowing up, a short coil is added to produce magnetic fields to focus the beam. For simplicity, this coil is wound on an aluminum tube without iron around it. Fields are smaller without the iron, but they are still large enough to focus the beam. The physical length of the coil is 5.6 cm. Figure 2.9 is the measured magnetic field profile along the axis. Two lines indicate the physical edges of the solenoid. Note that due to lack of the iron, the field extends much longer than in the previous case and the peak field is also much smaller. Curve fitting gives the formula of the field profile as

$$B_z(z) = B_0 c\left(\frac{z+\frac{l}{2}}{((z+\frac{l}{2})^2+a^2)^{1/2}} - \frac{z-\frac{l}{2}}{((z-\frac{l}{2})^2+a^2)^2}\right). \qquad (2.5)$$

Here, c=1.4237, l=4.5322 cm and a=6.0416 cm. B_0 is the peak axial magnetic field and its dependence on the wire current is given by

$$B_0 = 0.39107 + 5.688 \times I. \qquad (2.6)$$

Again, B_0 is in the unit of Gauss, and I is the current, in amperes. Figure 2.10 shows the measurement points for this formula.

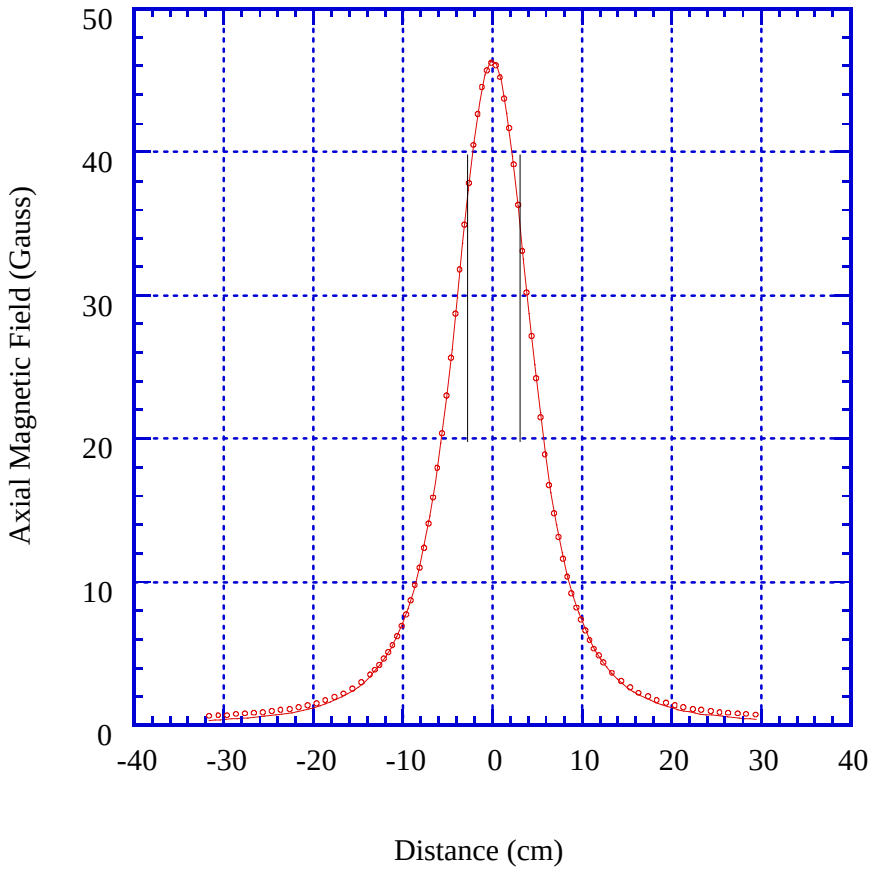

Figure 2. 9. Axial magnetic filed produced by a short coil. The two lines indicate the physical edge of the coil.

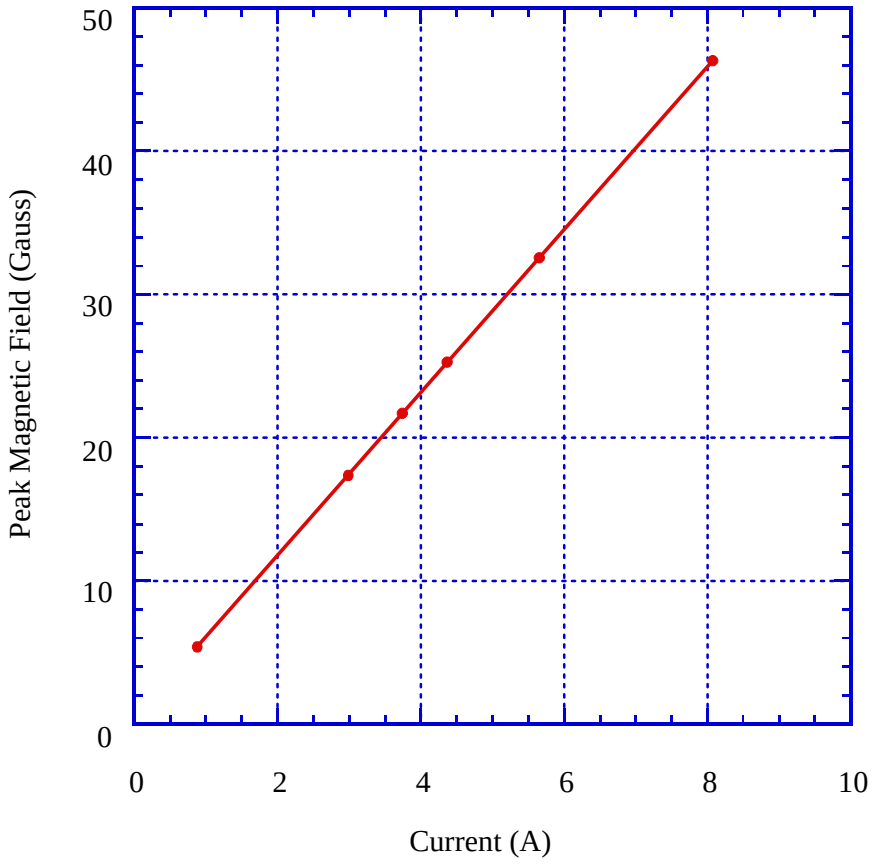

Figure 2. 10. Solenoid's peak magnetic field vs. current.

2.4 Resistive-Wall Tubes

The key component in the resistive-wall channel is a glass tube coated with resistive material. The resistive material in the inner surface is Indium-Tin-Oxide (ITO). Total resistance of the tube is 10.1 kΩ. The resistive part of tube is 0.99 m long and has inner diameter of 3.8 cm, which corresponds to an area resistivity of 1.22 kΩ per square. It has bellows and metal parts with flanges at both ends to connect to other components. Silver paste is used to make good contact between the resistive material and the metal parts. Total length of the tube including metal parts is 123 cm. These glass tubes were custom made for us at the Institute of Vacuum Electronics, Beijing, China.

2.5 Diagnostics

The diagnostic tools installed in the experiment include energy analyzers, current monitors and a phosphor screen. The main tool is the energy analyzer. The energy analyzer was developed by Hyyong Suk, the former Ph.D. student. The geometry of the energy analyzer is illustrated in Figure 2.11 [7]. As shown in the figure, it consists of two parallel plates and one collector. Two plates have a hole with diameter of 4.8 mm. The holes are covered with wire meshes to produce a uniform electric field. The collector is connected to 50 Ω channel of a digital signal analyzer (Tektronix DSA 602A) through vacuum feedthrough. Chapter 4 will explain the principle of the energy analyzer in detail.

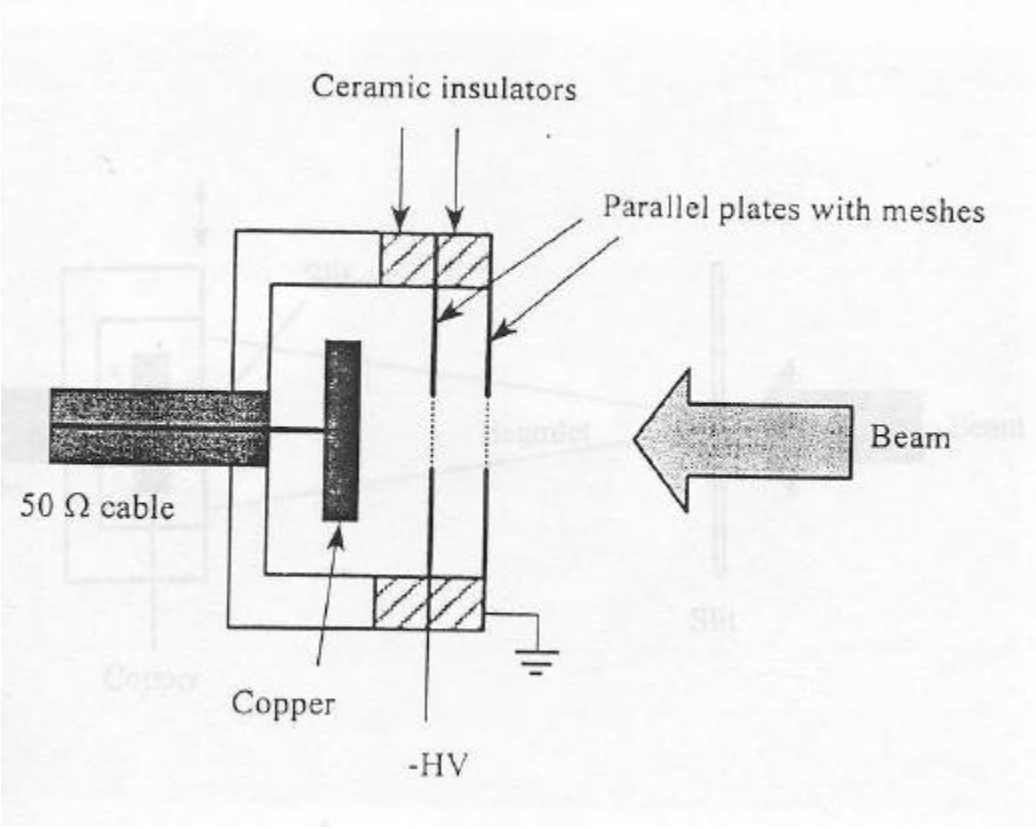

Figure 2. 11. Structure of the energy analyzer.

There are two resistive-wall type current monitors in the system. The total resistance for each current monitor is 1.1 Ω so the sensitivity is 1.1V/A.

Another tool in the experiment is phosphor screen. With a CCD camera and a computer, the beam image on the phosphor screen can be digitized and processed later by a computer program.

There are two diagnostics chambers in the system. The first chamber is located between the second and third solenoids. It contains a retarding voltage energy analyzer. The position of the energy analyzer could be accurately adjusted by a linear and rotation feedthrough. When we measure the energy of the beam, the energy analyzer is laid down to the center of the pipe. When we do the measurement downstream, the energy analyzer is lifted up to let the beam pass by.

The second diagnostic chamber is located after the resistive wall. This chamber has a phosphor screen, a retarding voltage analyzer and a slit-slit emittance meter in it. All of the diagnostics are adjustable and can move inside the chamber independently.

2.6 Vacuum System

Vacuum is very important to the experiment. Due to the scattering between the beam and the residual gas, poor vacuum will cause beam emittance growth and other beam quality deterioration [1]. In this experiment, because the cathode is getting old, it also requires good vacuum (10^{-9} Torr) to have good emission.

Tremendous attention was taken to obtain high vacuum. Every new component has to be cleaned using alconox, deionized water, methanol, acetone and TCE.

The vacuum system consists of a turbo-molecular roughing pump and five ion pumps. The ion pump speeds are 8 l/s, 60 l/s, 40 l/s and 30 l/s respectively. The 8 l/s pump is located on top of the electron gun. The 60 l/s pump is located between the first and second solenoids. It is about two feet away from the beam line to avoid the magnetic field from affecting the electron beam. The 40 l/s and 30 l/s pumps are connected to the second diagnostic chamber. To pump down the vacuum, we first use the turbo-molecular pump to pump down to 10^{-7} Torr range. This step will take several hours. Then the ion pumps are turned on to bring the pressure down to 10^{-8} Torr. After that, heating tapes are used to bake the system to about 160^{o} C to remove any moisture and other residual gas. Sometimes, aluminum foils are wrapped around the system to have higher baking temperature. However, care must be taken not to damage the component, especially the ion pump magnet, with which the baking temperature can not be higher than 250^{o} C. After these steps, usually the system pressure could be around low 10^{-9} Torr range. The whole procedure will take about two weeks for each procedure starting from the air pressure.

Chapter 3

Space-Charge Waves in Electron Beams Propagating Through a Resistive-Wall Channel

3.1 Motivation

Transport and acceleration of intense charged particle beams with high quality are important issues in advanced accelerator applications such as colliders for high-energy physics, induction linacs for heavy-ion inertial fusion, high intensity linacs and synchrotrons for spallation neutron sources, etc. Due to the requirements of ever increasing beam intensity in these applications, space-charge effects and collective behavior among charged beam particles play a crucial role in the beam dynamics, which may limit the maximum transportable beam current and deteriorate the beam quality. One such collective phenomenon is longitudinal space-charge waves generated by line-charge perturbations on beams, and longitudinal instabilities caused by the interaction between the space-charge waves and a dissipative environment, i.e. a resistive transport channel. For example, a heavy-ion fusion driver may consist of many induction modules. An induction accelerator for heavy ion fusion would have currents of heavy ions in the range between 20 to 30 KA and energy of 5 to 10 GeV. The average wall resistance of such an induction accelerator is about 100-300Ω/m. Longitudinal space-charge

waves can be generated on beams due to fluctuations in the bunch, mismatch between external focusing forces and space-charge forces, and other effects. Their propagation on beams and interaction with this kind of resistive environment leads to growth of slow space-charge waves due to the resistive-wall instability. The instability is caused because a perturbation in the beam current produces a corresponding perturbation in the return current, which flows through the wall. Ohm's law tells us that a current through a resistive wall requires an electric field. This electric field, on the other hand, may enhance the perturbation in the beam current and cause instability. The resistive-wall instability increases the longitudinal beam energy spread and may cause a dilution of the transverse emittance. The increase of the longitudinal beam energy spread and transverse emittance, in turn, makes it difficult to focus the beam into a short pulse and on a small spot. Therefore, the resistive-wall instability has become a concern for the success of this program.

The investigation of the longitudinal instability in charged particle beams has a long history. The early work on the instability was originated from the study of microwave tubes [8, 15]. Since 1980, the problem of the longitudinal instability has received new attention in connection with research on high-current accelerators for various applications. There has been some theoretical work in this area [1, 16, 17]. But there has been no experiment dedicated to this topic except in the EBTE group at the University of Maryland, under the direction of Prof. Reiser [18-22]. In the

applications of microwaves, the conventional approach is to use sinusoidal signals to generate space-charge waves. In the experiments conducted at the University of Maryland, localized waves are used as beam diagnostics. This has many advantages to the sinusoidal wave in diagnosing some beam parameters such as the wave propagation speed, the geometry factor g for the longitudinal space-charge field, the beam radius and so on. Also, this is the usual case for the instability in the induction linacs for heavy-ion fusion. Another feature of these experiments is that an electron beam, instead of a heavy-ion beam, is used. Because the electron has a much smaller mass than heavy ion, it is possible to observe the instability in a short facility (~ 1 m) with large resistivity.

In this chapter, a brief review of the linear theory of the resistive-wall instability is given first. Then the experimental results in both linear and non-linear regime are reported. In the linear regime, we can observe the results predicted by the theory. However, in the non-linear regime, some abnormal phenomena are observed.

3.2 Linear Theory on the Resistive-Wall Instability

3.2.1 Resistive-Wall Instability Theory Based on One-dimensional Model and Vlasov Equation.

The resistive-wall instability can be studied with different methods. One usual way is to use one-dimensional cold fluid equation to study the resistive-wall instability [23, 24]. Another way is to use one-dimensional Vlasov equation. This method can give more general results and also can be applied to the case of beam with energy spread or Landau-damping effect. Here, we will follow the second approach.

As been illustrated in Figure 3.1, suppose that a beam of momentum p is transported in a cylindrical pipe with wall impedance Z_w. Its one-dimensional distribution function has the form

$$f(z, p, t) = f_0(p) + f_1(z, p, t). \qquad (3.1)$$

Here, the subscript 0 represents the unperturbed quantity while the subscript 1 represents the perturbed term. In the linear theory, it is always assumed that the perturbation is small compared to the unperturbed term. The perturbed line charge and current are subject to the continuity condition

$$\frac{\partial \Lambda_1(z,t)}{\partial t} + \frac{\partial i_1(z,t)}{\partial z} = 0. \qquad (3.2)$$

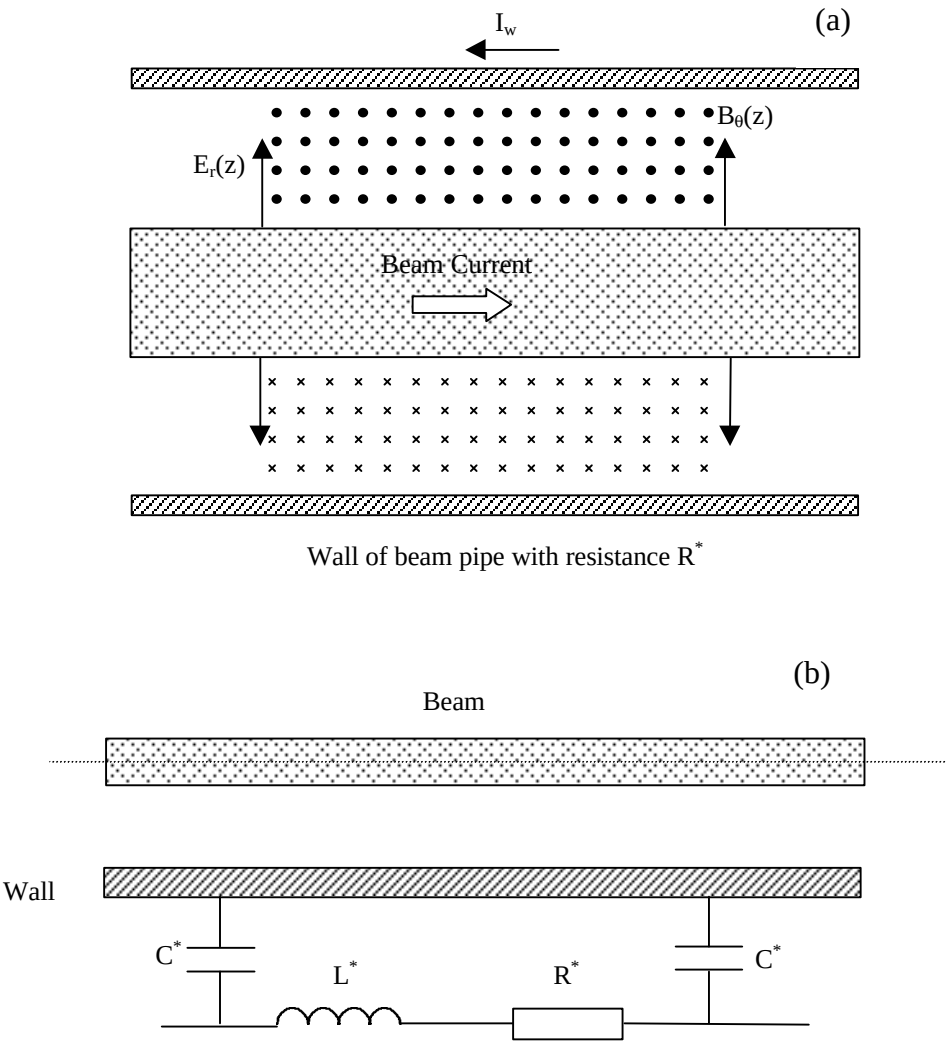

Figure 3. 1. (a) Particle beam inside a resistive-wall pipe. (b) Lossy transmission-line model for a resistive transport channel.

Here, $\Lambda_1(z,t)$ is the perturbed line charge density and $i_1(z,t)$ is the perturbed beam current. The second equation governing the perturbation is the linearized one-dimensional Vlasov equation

$$\left(\frac{\partial}{\partial t}+v\frac{\partial}{\partial z}+qE_0\frac{\partial}{\partial p}\right)f_1(z,p,t)=-qE_1(z,t)\frac{\partial f_0(p)}{\partial p}. \qquad (3.3)$$

In the equation, E_0 is the unperturbed electrical field which should be zero in the uniform beam, and E_1 is the electric field due to perturbation. It can be expressed by

$$E_1(z,t)=E_s(z,t)+E_w(z,t), \qquad (3.4)$$

where $E_s(z,t)$ is the axial electric filed due to non-uniform line charge density and beam current and $E_w(z,t)$ is the electrical field due to wall impedance. By long wavelength approximation, $E_s(z,t)$ is related to beam current and density by

$$E_s(z,t)=-\frac{g}{4pe_0}\left(\frac{\partial\Lambda_1(z,t)}{\partial z}+\frac{1}{c^2}\frac{\partial i_1(z,t)}{\partial t}\right), \qquad (3.5)$$

where g is the geometry factor and is given by $g=2\ln(b/a)$ with a and b being the beam radius and pipe radius respectively. c is the speed of light and ε_0 is the permittivity of vacuum. In the frequency domain, the $E_w(k,\omega)$ is related to the wall impedance per unit length by

$$E_w(k,w)=-Z_w^*(k,w)\Lambda_0\int vf_1(z,p,t)dp. \qquad (3.6)$$

Here, Z_ω^* is the wall impedance per unit length and v is the beam velocity.

If assume that the perturbation has the form of exp[i(ωt-kz)], and plug the above equations into (3.3), we can get the dispersion equation[21]

$$1 - iq\Lambda_0 \frac{w}{m}\left[Z_s^*(k,w) + Z_w^*(k,w)\right] \times \int \frac{f_0\{p\}}{g^3 (w - kv)^2} dp = 0 . \qquad (3.7)$$

Here, Z_s^* is defined as the space-charge wave impedance per unit length and can be expressed as

$$Z_s^*(k,w) = i\frac{g}{4p}\left(-\frac{ck^2}{w} + \frac{w}{c}\right)Z_0 , \qquad (3.8)$$

where c is the speed of light and Z_0 is the characteristic impedance of free space, equal to 377 Ω.

So far this dispersion equation is valid for different wall impedance within the framework of the theoretical model. In the following section, we will apply this equation to various situations.

3.2.2 Space-Charge Waves in a Monoenergetic Electron Beam With Conducting, Resistive and Complex Wall Impedance

First let us assume that the electron beam has no energy spread and the distribution function is expressed by

$$f_0(p) = d(p - p_0) . \qquad (3.9)$$

In this case, the dispersion equation is reduced to

$$-i\frac{mg^3}{wq\Lambda_0}(w-kv_0)^2 = Z_s^*(k,w)+Z_w^*(k,w)\,. \qquad (3.10)$$

Here, v_0 is the beam velocity. Using the model in Figure 3.1, the wall impedance can be written as

$$Z_w^* = R_w^* + iX_w^*\,. \qquad (3.11)$$

If we use the assumption that $w_0 \approx kv_0$, the space-charge impedance per unit length can also be approximated as [1]

$$Z_s^* = -iX_x^* = -i\frac{gw}{4pcb^2g^2}Z_0\,. \qquad (3.12)$$

Using Equations (3.11) and (3.12), we can solve Equation (3.10) and get the expressions for real and imaginary part of the wave number k as

$$k_r = k_0\left\{1\pm\left(\frac{pKb}{k_0Z_0}\right)^{1/2}\left[\sqrt{R_w^{*2}+\left(X_w^*-X_s^*\right)^2}-\left(X_w^*-X_s^*\right)\right]^{1/2}\right\} \qquad (3.13)$$

and

$$k_i = \mp k_0\left(\frac{pKb}{k_0Z_0}\right)^{1/2}\left[\sqrt{R_w^{*2}+\left(X_w^*-X_x^*\right)^2}-\left(X_w^*-X_s^*\right)\right]^{1/2}, \qquad (3.14)$$

where K is the generalized beam perveance and Z_0 is the impedance of free space. The real part k_r corresponds to the travelling wave part and the imaginary part k_i corresponds to the spatial growth part of the wave.

In the conductor wall case, both R_w^* and X_w^* are zero, then Equation (3.14) shows that k_i is equal to zero and k_r is reduced to

$$k_r = k_0\left(1 \pm \frac{c_s}{v_0}\right). \qquad (3.15)$$

Here c_s is the wave speed in the beam frame, defined as

$$c_s = \left(\frac{qg\Lambda_0}{4pe_0 g_0^5 m}\right)^{1/2}. \qquad (3.16)$$

The above equation tells us that when there is a perturbation in the electron beam with conducting wall, the perturbation will propagate inside the beam with wave velocity c_s. There are two waves, one is fast wave, which moves forward in the beam frame and another one is slow wave, which moves backward.

Let us take an example of parameters of the beam in our experiment to calculate c_s. For a beam with energy 3.5 keV, beam current 16 mA. The above equations give us beam velocity of 3.49×10^7 m/s and wave velocity c_s of 1.176×10^6 m/s. The ratio of the wave velocity to the beam velocity is 3.4%, which is consistent with our assumption.

If the beam pipe has pure uniform resistance, the wall impedance is expressed as

$$Z_w^* = R_w^*. \tag{3. 17}$$

Plug this equation into equations (3.13) and (3.14), we get

$$k_r = \frac{w}{v_0}\left\{1 \pm \left(\frac{pKb}{k_0 Z_0}\right)^{1/2}\left[\sqrt{R_w^{*2} + X_x^{*2}} + X_s^*\right]^{1/2}\right\}, \tag{3. 18}$$

and

$$k_i = \mp\frac{w}{v_0}\left(\frac{pKb}{k_0 Z_0}\right)^{1/2}\left[\sqrt{R_w^{*2} + X_x^{*2}} - X_s^*\right]^{1/2}. \tag{3. 19}$$

Here, k_0 is defined as ω/v_0 and K is the generalized beam perveance. If we assume that $R_w^* << X_s^*$, then the above equations can be reduced to

$$k_r = k_0\left(1 \pm \frac{c_s}{v_0}\right), \tag{3. 20}$$

and

$$k_i = \mp 2p\,\frac{R^*}{Z_0}\left(\frac{I}{I_0 gbg}\right)^{1/2}. \tag{3. 21}$$

In the equation, I_0 is the characteristic current of the electron beam, which is defined as $4pe_0 mc^3/q$. From this relationship, we find that fast waves and slow waves still propagate with the same speed as in the conducting wall case. However, the imaginary part of the wave vector is not zero in this case, which means that the wave will grow or decay spatially. In the resistive-wall instability, the fast wave

will decay and the slow wave will grow. Notice that in the regime defined by Eqs. (3.20), (3.21), the growth/decay rate in this condition, the growth rate of the wave is independent of the frequency. The growth/decay rate k_i depends on the resistance per unit length of the transport channel and the beam current and the beam energy through the factor $\beta\gamma$. Higher channel resistance and beam current lead to higher growth/decay rate, higher energy decreases the growth/decay rate.

To apply the above theory to a laboratory beam, let us take the example of a 3.5 keV electron beam with I=16 mA, R_w^*=10 kΩ, g≅2. From equation (3.21), we find k_i=0.33 1/m. The e-folding growth distance is around 3m. Figure 3.2 shows the growth/decay rate at different beam energy and beam current in a pure resistive channel.

If the space-charge impedance is not larger than the wall impedance, then we have to use equations (3.18~3.19) to calculate the growth rate. Because the space-charge impedance depends on the frequency, the growth rate in this case is also frequency dependant. Figure 3.3a shows the relative strength of the space-charge impedance and the wall impedance. At low frequency, the space-charge impedance is smaller than the wall impedance. However, it becomes larger than the wall impedance at the frequency above 150 Mhz. Figure 3.3b shows the frequency dependence of the growth rate. The growth rate increases with the frequency and approaches to the number indicated by equation (3.21), shown by a horizontal line.

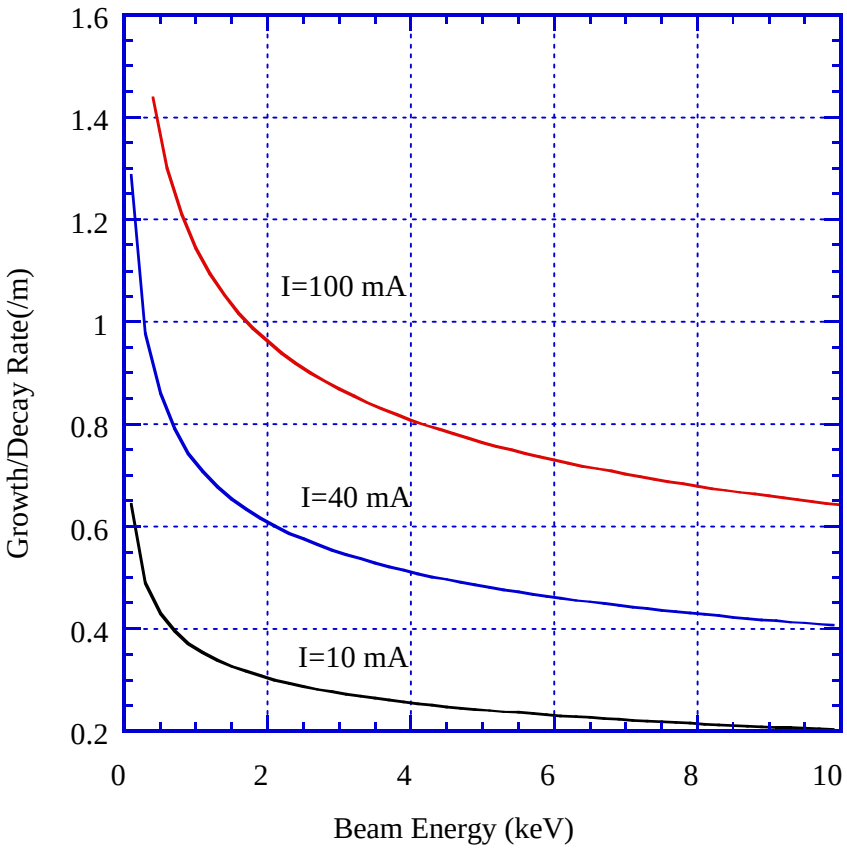

Figure 3. 2. Space-charge wave growth/decay rates at various beam energies and beam current for 10 kΩ resistive tube.

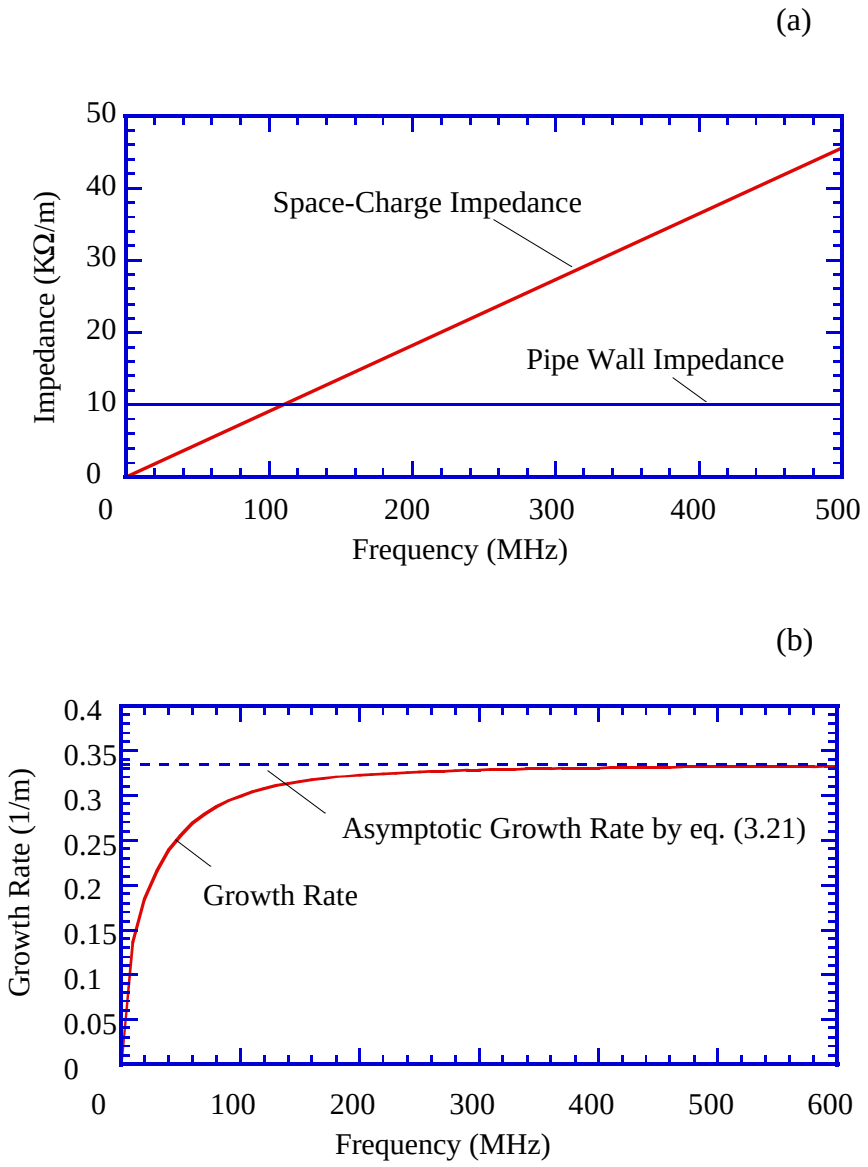

Figure 3. 3. (a) Relative strength of the space-charge impedance and resistive-wall impedance. (b) Frequency dependence of the growth rate of space-charge waves.

The general resistive wall impedance can be modeled using lossy transmission line as being illustrated in Figure 3.1b. The model includes a series inductor and resistor and a parallel capacitor designated by L^*, R^* and C^*. The impedance of this transmission line is

$$Z_w^*(k,w) = \frac{k^2\left(R^* + iwL^*\right)}{k^2 - w^2 L^* C^* + iwR^* C^*} = R_w^* + iX_w^*. \qquad (3.\ 22)$$

The real part and imaginary part of the impedance can be calculated as

$$R_w^* = \frac{R^*}{\left(1 - L^* C^* v_0^2\right)^2 + \left(R^* C^* v_0^2 / w\right)^2}, \qquad (3.\ 23)$$

and

$$X_w^* = \frac{wL^*\left(1 - L^* C^* v_0^2\right)^2 - R^{*2} C^* v_0^2 / w}{\left(1 - L^* C^* v_0^2\right)^2 + \left(R^* C^* v_0^2 / w\right)^2}, \qquad (3.\ 24)$$

respectively.

The capacitance and inductance parts have different effect on the growth rate. To study this effect, first study a case with $R^* \neq 0$, $C^* \neq 0$ and $L^* = 0$. In this case, the growth rate becomes

$$k_i = \frac{2pR^*}{Z_0}\left(\frac{I}{I_0 gbg}\right)^{1/2} \frac{1}{1 + \left(R^* C^* v_0^* / w\right)^2}\left(1 + \frac{R^*}{X_s^*}\frac{R^* C^* v_0^* / w}{1 + \left(R^* C^* v_0^* / w\right)^2}\right)^{-1/2}. \qquad (3.\ 25)$$

Compared to equation (3.21), we find that the growth rate is smaller due to the capacitance of the channel.

In another case, if we assume that $R^{*}\neq 0$, $C^{*}=0$ and $L^{*}\neq 0$, then the growth rate can be expressed as

$$k_i = \frac{2pR^{*}}{Z_0}\left(\frac{I}{I_0 gbg}\right)^{1/2}\left(1+\frac{wL^{*}}{2X_s^{*}}\right). \qquad (3.\ 26)$$

As expected, in this case, the inductance of the transport channel increases the growth rate.

3.2.3 Landau Damping

As mentioned before, Vlasov equation can also be used to the case of the beam with initial energy spread. The beam energy spread can decrease the growth rate or prevent the instability from developing. This effect is known as Landau Damping in the literature [1]. Landau damping has been studied extensively in the circular accelerators. Reference [21] has a complete theory on the linear machine with complex wall impedance. With appropriate distribution function and the dispersion equation, the theory can predict the boundary between the stability and instability. It shows that, due to the initial energy spread, the stable region can be created in the otherwise unstable region. Both Lorentz distribution and Gaussian distribution are used in the analysis.

3.3 Experimental Study of the Resistive-Wall Instability

3.3.1 Generation of Space Charge Waves

An experimental facility has been set up to study the resistive-wall instability of space-charge-dominated beam. The experiment setup is shown in Figure 2.1, and has been described in Chapter 2.

In the experiment, localized perturbation is used to study the interaction of electron beams with the beam pipe. The diagnostics with localized space-charge wave is relatively easy and intuitive. It is easier to identify the fast wave and slow wave and their propagation through the channel. To generate the space-charge waves, we modulated the cathode-grid pulse with a small bump as shown in Figure 3.4. The strength of the perturbation can be adjusted by using different lengths of cables as described in Chapter 2. Figure 3.5 shows the perturbations with different strength produced by different cables. For clarity, only the perturbation part is shown in the figure.

In the sinusoidal wave case, usually both fast and slow space-charge waves are generated when the electron beam is perturbed. However, for the localized wave, it is possible to generate only one fast wave or slow wave, or both [27]. When both waves are generated, fast wave will move forward and slow wave will move backward in the beam frame. If the transport channel is long enough and they

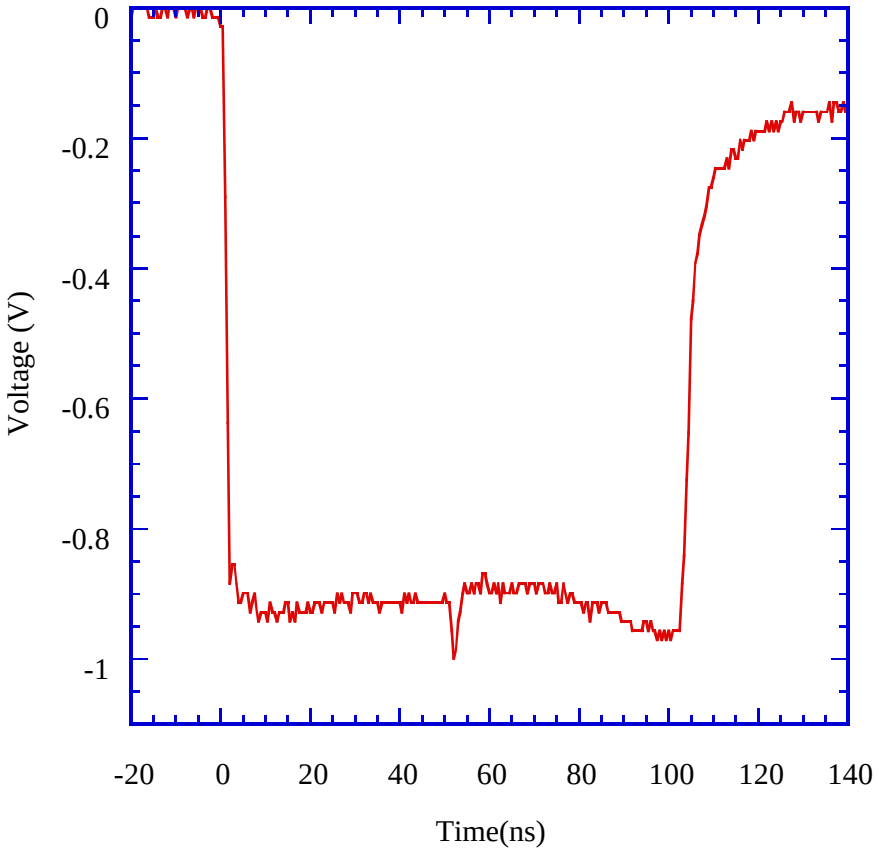

Figure 3. 4. Cathode-grid signal with a small localized perturbation in the middle.

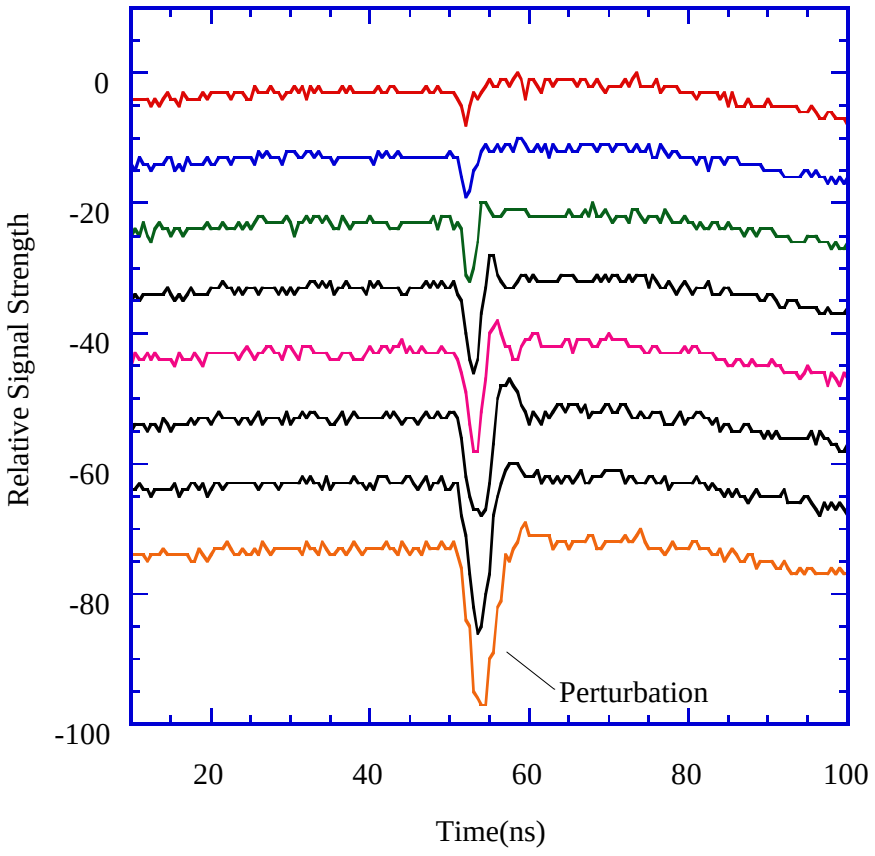

Figure 3. 5. Perturbations of different strengths at the grid-cathode signal.

reach the end, they will be reflected back [28]. In our experiment, in order to study the different behaviors of the waves, we try to avoid the mixture of both waves. Electron gun condition can be adjusted for the purpose of generating single fast or slow wave. The reason is as follows. The initial cathode-grid perturbation corresponds to a positive velocity perturbation on the beam particles, which, in turn, produces the initial density or current perturbation. The relative strength of the initial current, or density perturbation can be varied depending on the gun condition. For instance, an initial velocity perturbation will produce large current perturbation if the gun is operated in the temperature-limited regime; on the other hand, a relative small current perturbation will be produced by the same initial velocity perturbation if the gun is in the space-charge limited regime. The relative strength of velocity, current and density perturbation will determine whether a fast, slow or both waves are generated. If assume that the initial velocity perturbation is δ and the initial current perturbation is η, by the theory of reference [27], the larger is η/δ, the stronger is the fast wave. And in some ranges, one wave becomes dominant over another. If we want to generate a single fast wave, we operate the gun at relative higher energy and less space-charge-limited flow. On the other hand, to generate the slow wave, we have to reduce the beam energy and let the beam be more space-charge-limited flow.

In the experiment, we have to be able to test whether a fast or slow wave has been generated. Because the fast wave moves forward, and slow wave moves

backward, it is possible to determine it by timing the wave position. For example, for a 3.5 keV beam with beam current 16 mA, the beam velocity is 3.49×10^7 m/s and the wave velocity c_s is 1.176×10^6 m/s. After the beam is transported by one meter, the wave will propagate about 1 ns relative to the beam. This is noticeable from the wave signal and is used in the experiment to detect the slow or fast wave. However, because the beam expands due to space-charge force, sometimes it is difficult to determine the exact beam position. Hence, a second method is also used. According to the results from solving the fluid equation [27], two waves have opposite polarity for the current waveform. In our case, the fast wave has positive amplitude (current larger than the average beam current) and the slow wave has negative amplitude (current smaller than the average beam current). Figure 3.6 shows the typical waveform from the current monitor for both fast and slow waves. From the polarity of the current perturbation, we are able to tell whether a slow wave or fast wave has been generated.

3.3.2 Beam Matching into the Resistive-Wall Channel

As discussed in Chapter 2, the magnetic system consists of three matching lenses, one long solenoid and an extra short coil. The beam is uniformly focused in the long solenoid; the beam envelope can be adjusted by changing the focusing strength. The magnetic field of the long solenoids can be varied from 40 G to 80 G for good matching. The focusing strength of three matching lenses can be

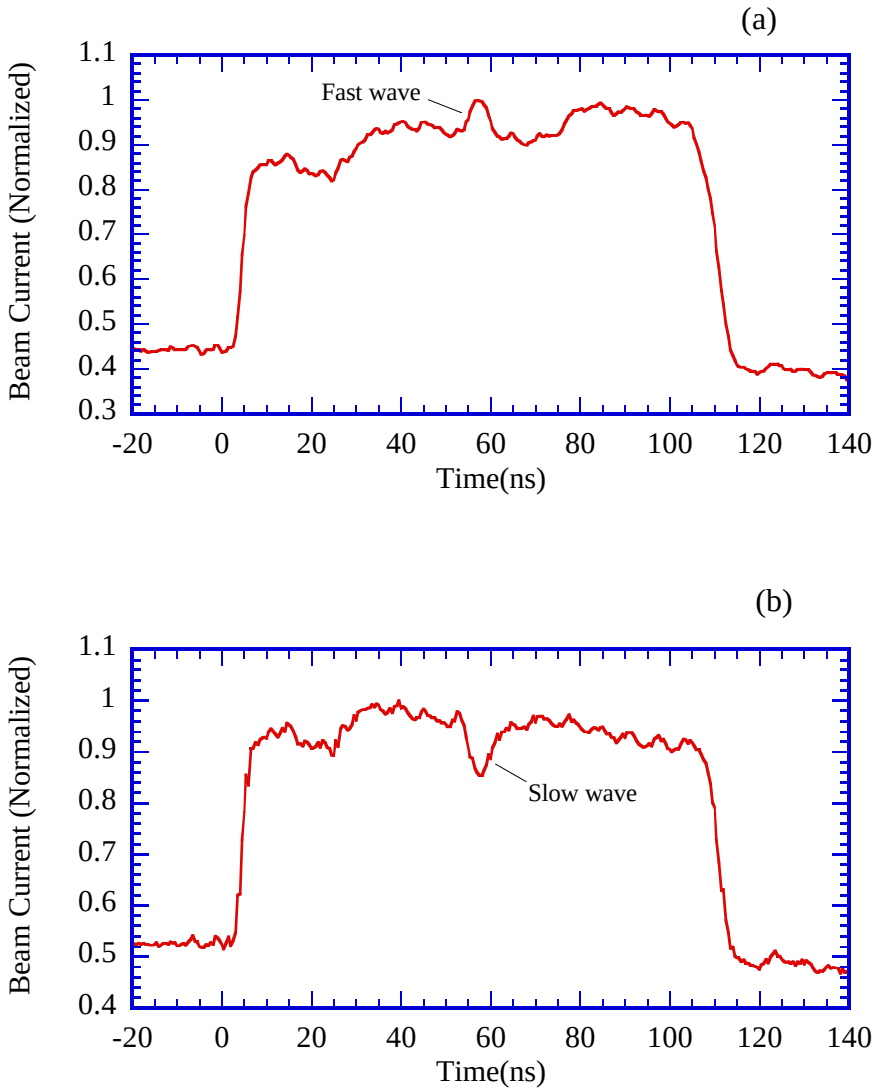

Figure 3. 6. (a) Fast wave signal has larger current than the main beam. (b) Slow wave signal has smaller current than the main beam.

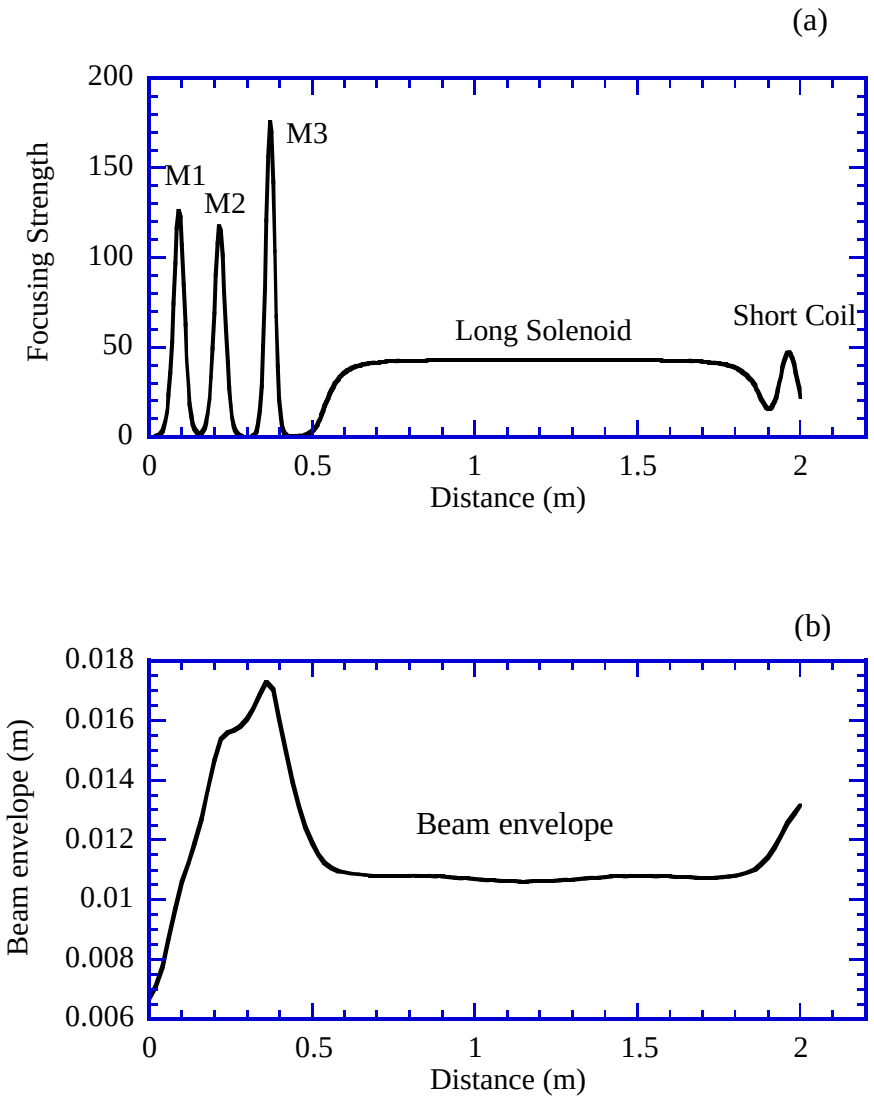

Figure 3. 7. Example of matching the beam into long solenoid.

(a) Focusing strength vs. distance from the electron gun. (b) Beam envelope vs. distance.

adjusted accordingly for the beam to be matched into the long solenoid. The peak magnetic fields of three matching lenses range from 40 G to 100 G respectively.

A K-V envelope equation has been solved to give us an idea how the beam is matched into the system. Figure 3.7 is one example of the matching case. Figure 3.7a gives the focusing strength of the magnetic lens. The driving currents for three matching lens are 2.24, 2.16 and 2.25 A respectively. The long solenoid current is 3 A and the short coil current is 4 A. Figure 3.7b gives the beam envelope vs. distance from the electron gun. A 2.5 keV and 40 mA beam is used in the simulation. In the graph, the beam is matched into the long solenoid with little ripple. The simulation results provide the guidelines for the experiment.

3.3.3 Experiments of Space-Charge Waves in the Linear Regime

After a space-charge wave has been generated and injected into the resistive wall. The space-charge wave will interact with the resistive wall and will either grow or decay. In our experiment, we study the growth or decay rate of the energy width of space-charge wave. The energy width of space-charge waves are measured and compared at both ends of the resistive-wall channel. This is done as follows: by increasing the retarding voltage in the energy analyzers, the beams and space-charge waves can be gradually suppressed in the analyzer output. First, the main beam is suppressed at retarding voltage corresponding to the beam energy. Then, we increase the voltage further till the wave signal is also suppressed. The

difference of the two voltages gives the energy width of the space-charge wave, which is the most interesting parameter in the experiment.

Measurements with two energy analyzers for a fast wave have been performed for a beam of energy 3.595 keV and current 19.8 mA. A typical measurement with the first energy analyzers is shown in Figure 3.8. The location of the first energy analyzer is at the entrance of the resistive-wall channel. The beam is suppressed at a retarding high voltage of 3.595 kV. The remaining signal on the top trace is a fast wave in which particles have a higher energy than the average beam energy. When the retarding high voltage further increases, the space-charge-wave signal decreases and eventually disappears. Figure 3.9 gives the energy profile of the space-charge wave. This results in an energy width of 21 eV for the fast wave. The same measurement is also done at the second energy analyzer, which is located at the exit of the resistive-wall channel. Figure 3.10 shows the space-charge wave at different retarding voltages; and Figure 3.11 shows the energy profile of the wave. Both figures give the energy width of the fast wave at the second energy analyzer of 13 eV. The experiment shows that the energy width of fast space-charge wave decreases in the resistive environment. The energy width decreases from 21 eV to 13 eV, giving a spatial decay rate of –0.48/m.

The measurements are also done at different beam energy and beam current. Table 3.1 shows the results from beam energy 2.5 keV, 3.5 keV and 4 keV. The error bar for each measurement is also shown in the table. The experimental

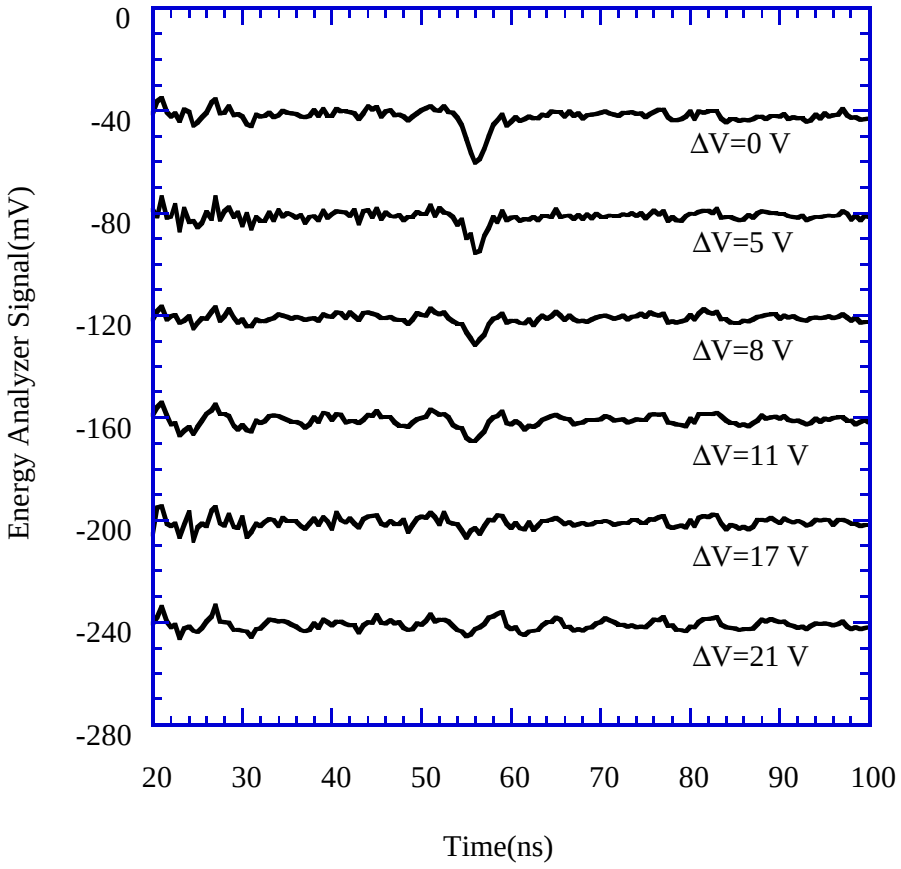

Figure 3. 8. Energy width of a fast space-charge wave at the first energy analyzer. Energy width ΔE_1=21 eV.

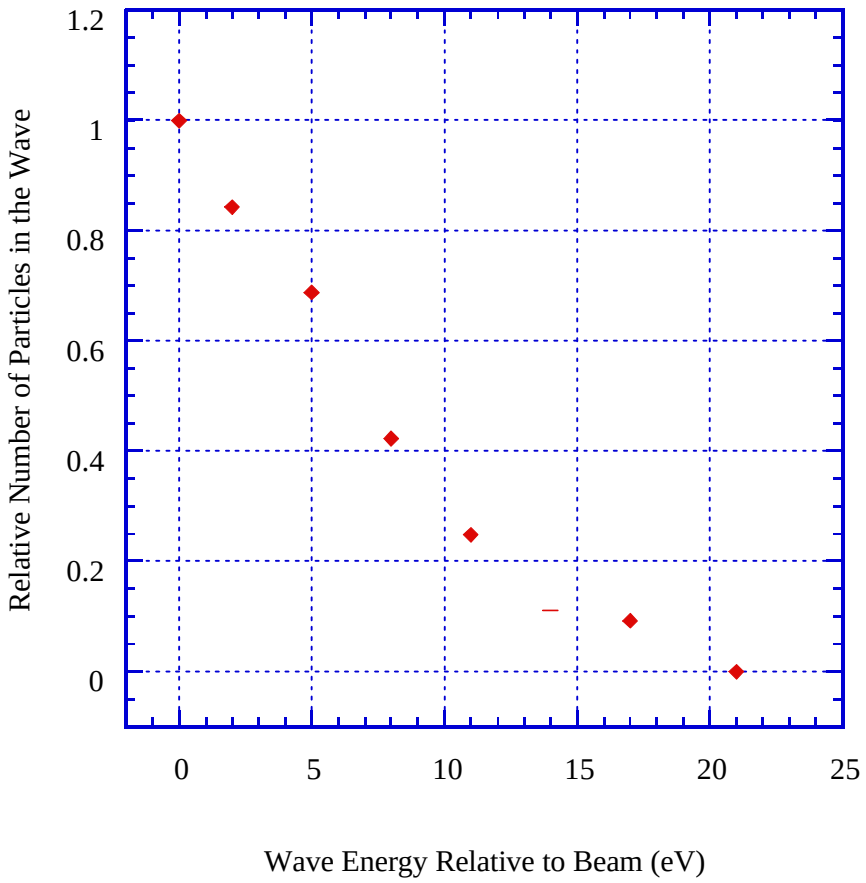

Figure 3. 9. Energy profile for a fast wave at the first energy analyzer.

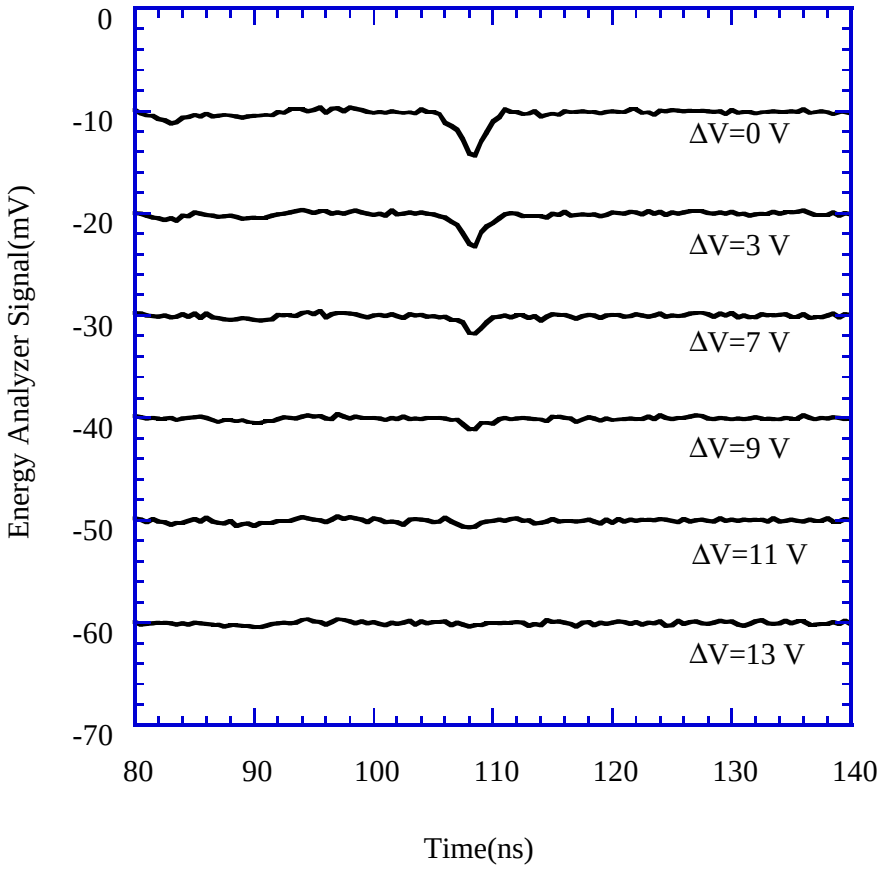

Figure 3. 10. Energy width of a fast space-charge wave at the second energy analyzer. Energy width ΔE_2=13eV.

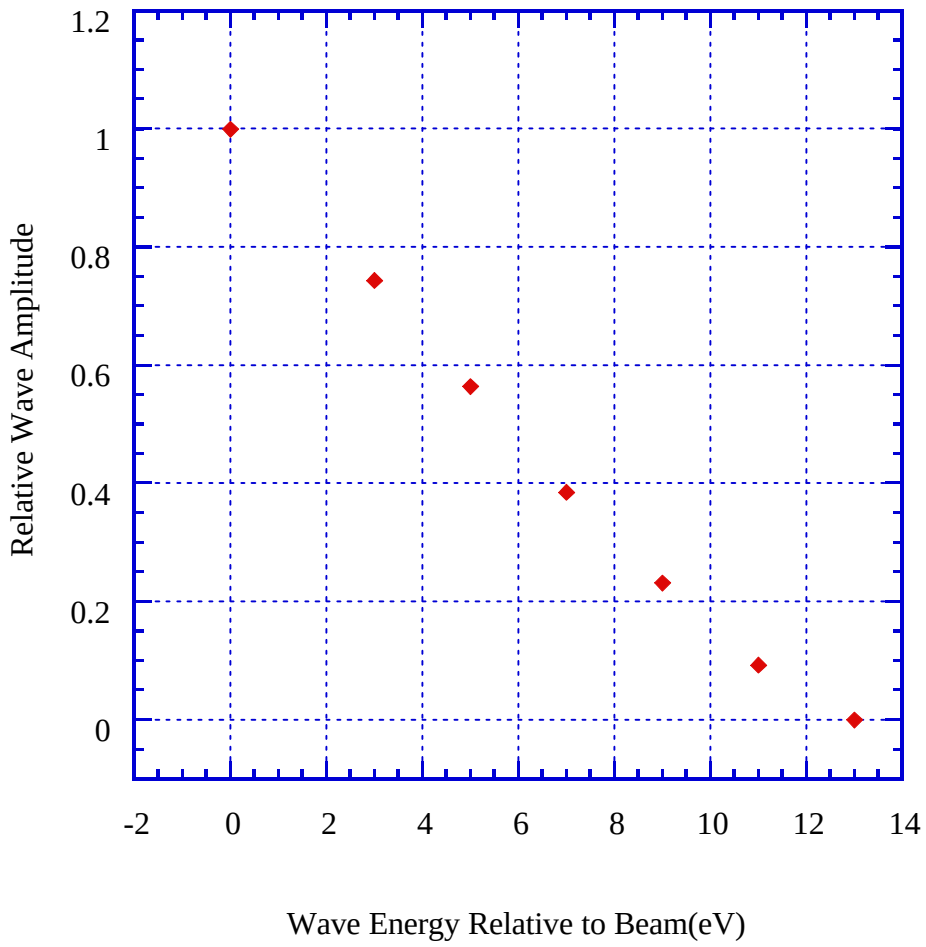

Figure 3. 11. Energy profile for a fast wave at the second energy analyzer.

results are compared with the calculated numbers from Equation (3.21). The comparison shows that they agree with each other reasonably well.

Table 3. 1. Fast space-charge wave decay rate at different beam parameters

Beam Energy (keV)	2.5	3.5	4
Beam Current (mA)	15.6	19.8	23.2
ΔE_1 (eV)	12 ± 1	21 ± 1	18 ± 1
ΔE_2 (eV)	7 ± 1	13 ± 1	16 ± 1
Experimental k_i (1/m)	-0.54 ± 0.2	-0.48 ± 0.12	-0.12 ± 0.12
Calculated k_i from Eq.(3.21) (1/m)	-0.41	-0.4	-0.39

Experiments are also performed to study the growth rate of slow space-charge wave in the resistive-wall pipe. In the experiment, the beam energy is 2.5 keV and the beam current is 30 mA. Figure 3.12(a) is for the measurement at the first energy analyzer while Figure 3.12(b) is for the measurement at the second energy analyzer. This figure indicates that energy width of slow wave in the resistive-wall channel increases from 27 eV to 37 eV, giving a growth rate of 0.32 1/m.

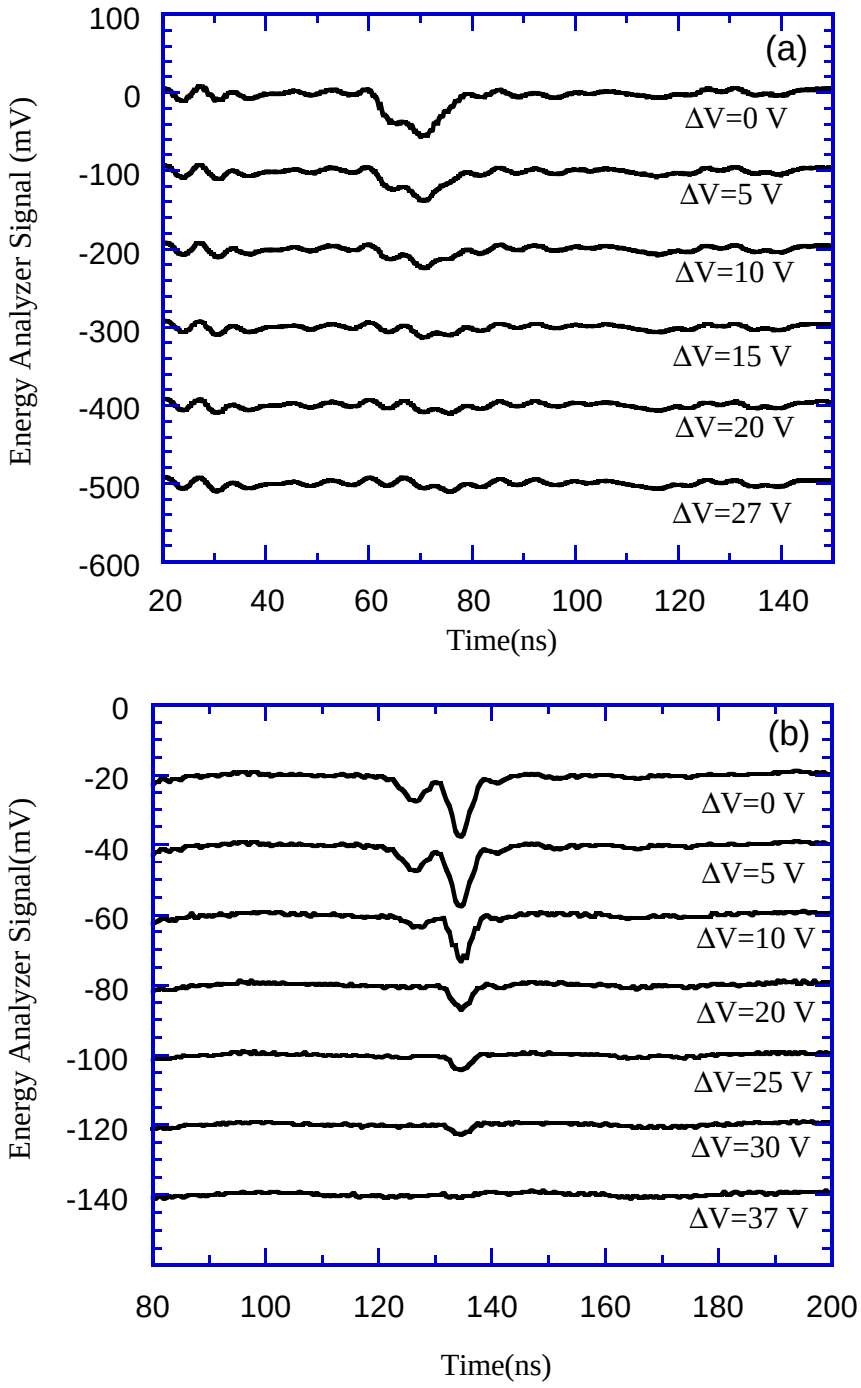

Figure 3. 12 (a) Energy width of slow wave at the first energy analyzer. (b) Energy width of slow wave at the second energy analyzer.

3.3.4 Experiments with Fast Waves in the Nonlinear Regime [43]

Measurements with the energy analyzers are also performed in the nonlinear regime where a rather large current perturbation is introduced on the beam. This is done by applying a strong voltage perturbation on the grid-cathode pulse of the electron gun, which results in large line-charge density and current perturbation on the beam. Figure 3.13 shows such a case, where the beam current signal is modulated with a large localized space-charge wave, measured before the resistive wall. The ratio of the wave amplitude over the average beam current is nearly 35%, a highly nonlinear case. In this experiment, we measure the evolution of the energy width of the nonlinear fast wave against this initial perturbation strength defined as the ratio I_p/I_b, where I_p and I_b are indicated in Fig. 3.13.

Measurements with two energy analyzers for the nonlinear fast waves have been performed for a beam of energy 2.5 keV and current 16 mA. The result of the measurement with the first energy analyzer is shown in Figs 3.14 and 3.15. As in the linear regime experiment, the location of the first energy analyzer (EA1) is near the entrance of the resistive-wall channel. The five curves in Fig. 3.14 show that the wave perturbation signal disappears at $\Delta V = 20$ V, where ΔV refers to the retarding voltage above the energy-equivalent beam voltage. From this result, we infer an energy width of 20 eV for the fast wave near the entrance of the resistive-wall channel. The same measurement is also done at the second energy analyzer, which

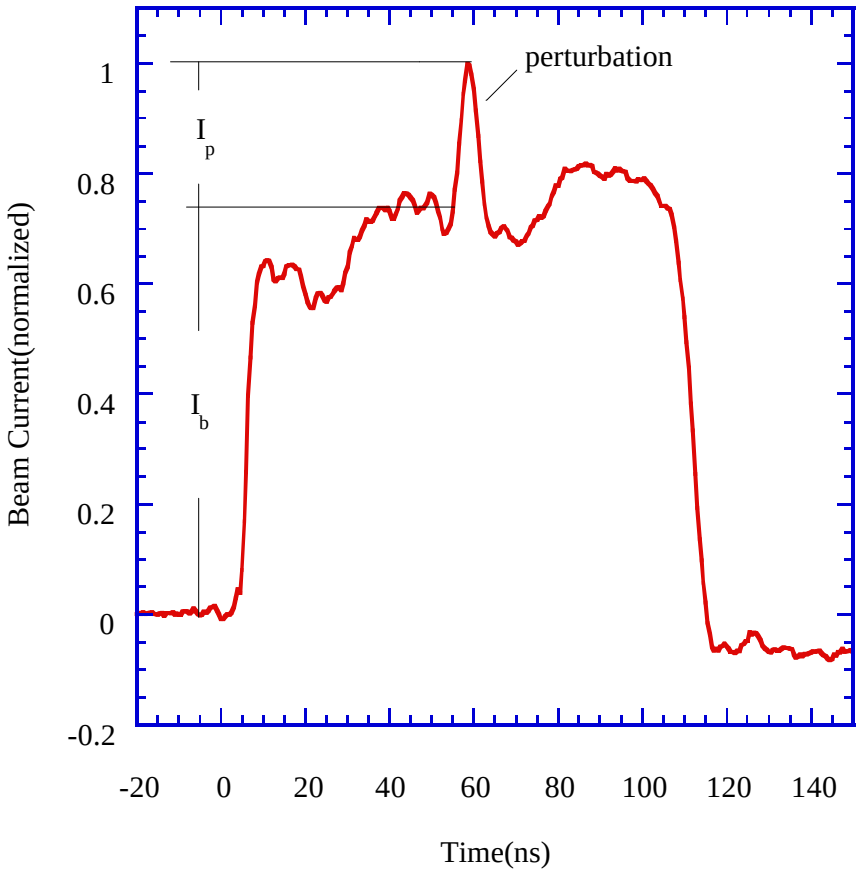

Figure 3. 13. Beam current signal with a highly nonlinear space-charge wave. Perturbation strength=I_p/I_b.

is located near the exit of the resistive-wall channel. In Fig. 3.15, we show the signal profiles of the fast wave measured at the second energy analyzer (EA2), which indicates that the energy width of the fast wave is equal to 25 eV. This result shows that, for the nonlinear initial perturbation generated on the beam pulse, the energy width of the fast space-charge wave increases when the beam propagates through the resistive wall. In this particular case, the energy width of the fast wave increases from 20 eV to 25 eV, yielding an exponential growth rate of $k_i = [\ln(\Delta V_2/\Delta V_1)]/\Delta z = 0.23/\text{m}$, where Δz is the length of the resistive channel.

The experimental results with the nonlinear fast waves are unexpected and to the best of our knowledge, no theory exists that can explain them. To study the dependence of the decay/growth rate of the fast waves on the initial perturbation strength, systematic measurements were performed for a 2.5 keV beam with 16 mA beam current. The waves are generated in the beam with different initial perturbation strengths. The results are shown in Fig. 3.16, where the growth/decay rates of the fast wave are plotted against the initial perturbation strength. In the linear regime, the fast wave decays, as expected. When the perturbation is strong enough, a transition from decay to growth takes place. The growth rate eventually levels off for the strongest perturbations in the experiments.

In order to eliminate possible errors in the diagnostics, we performed the same experiment in a conducting-wall tube, which replaced the resistive-wall tube while all the other conditions remain the same. In this case, essentially no growth

or decay was observed for the fast wave within the experimental error bars, as expected. The magnitude of the errors depends mainly on the resolution of the energy-width measurements. The results are plotted in Fig. 3.17.

We are so far not able to interpret this unexpected phenomenon. As mentioned earlier, no nonlinear model could be found, which would apply to our experiment. Furthermore, to our knowledge, at the present time, no particle-in-cell code exists that could be used to simulate our experiments. The closest simulation studies were done with a suitably modified WARP code by D. A. Callahan et al, for the linear case with an idealized geometry [26]. The extension of this code to the nonlinear regime in the same ideal geometry would require substantial code modifications and benchmarking, which would be very time-consuming and could not be done in the very near future. The simulation of our actual experiment will also require major code developments, which must include the launching of the perturbations from the gridded cathode and the transition from the conducting to the resistive-wall environment, an effort that will take several years. We plan to pursue such work in the future.

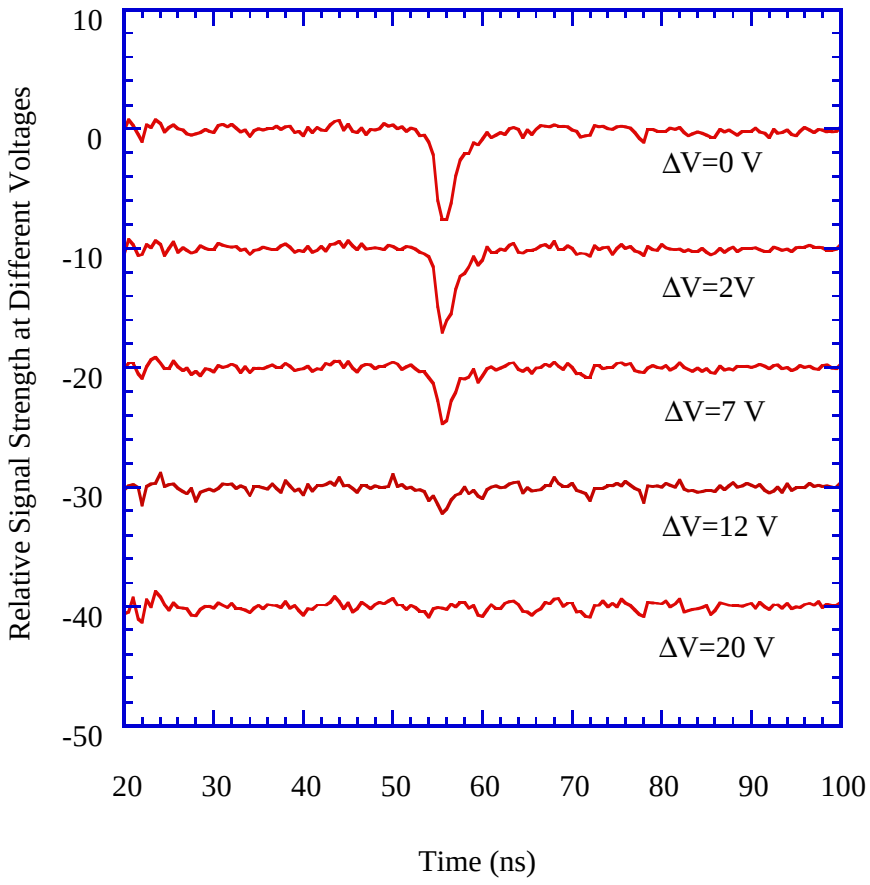

Figure 3. 14. Energy width of a fast wave at the first energy analyzer. Energy width ΔE_1=20 eV.

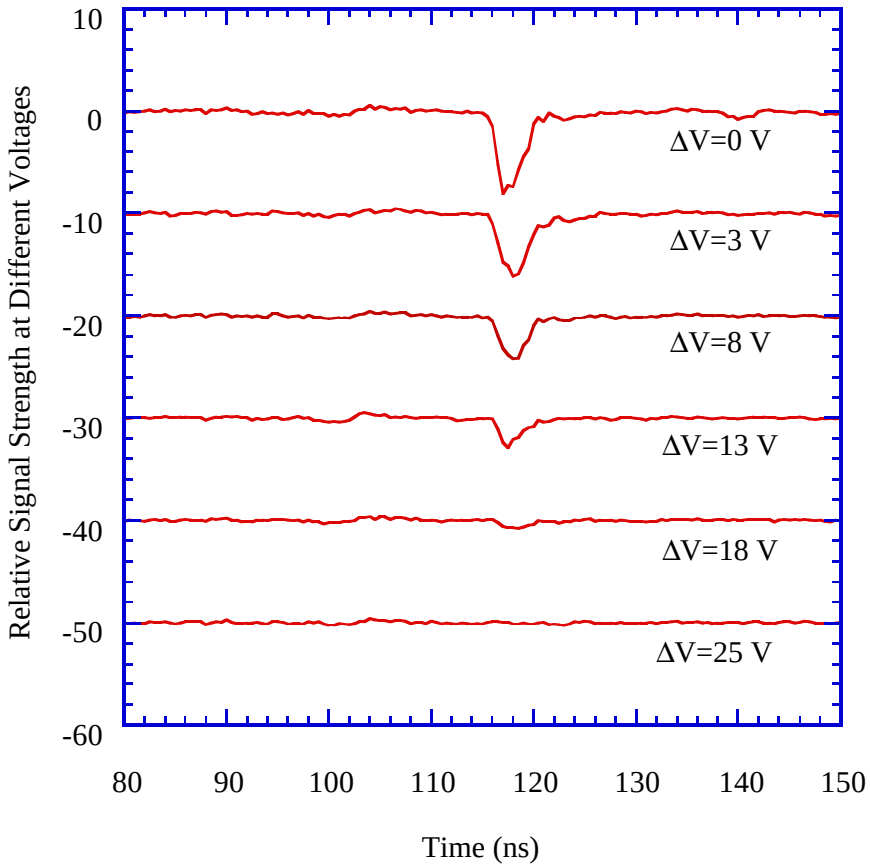

Figure 3. 15. Energy width of a fast wave at the second energy analyzer. Energy width ΔE_2=25 eV.

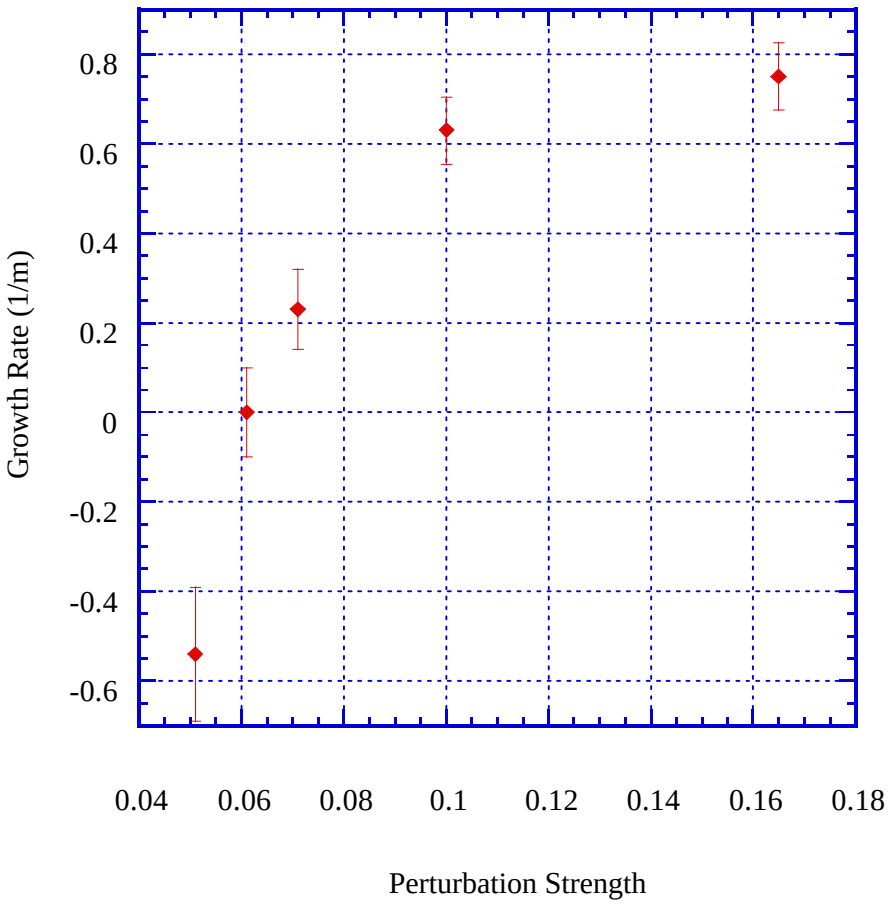

Figure 3. 16. Growth rate vs. perturbation strength for fast waves.

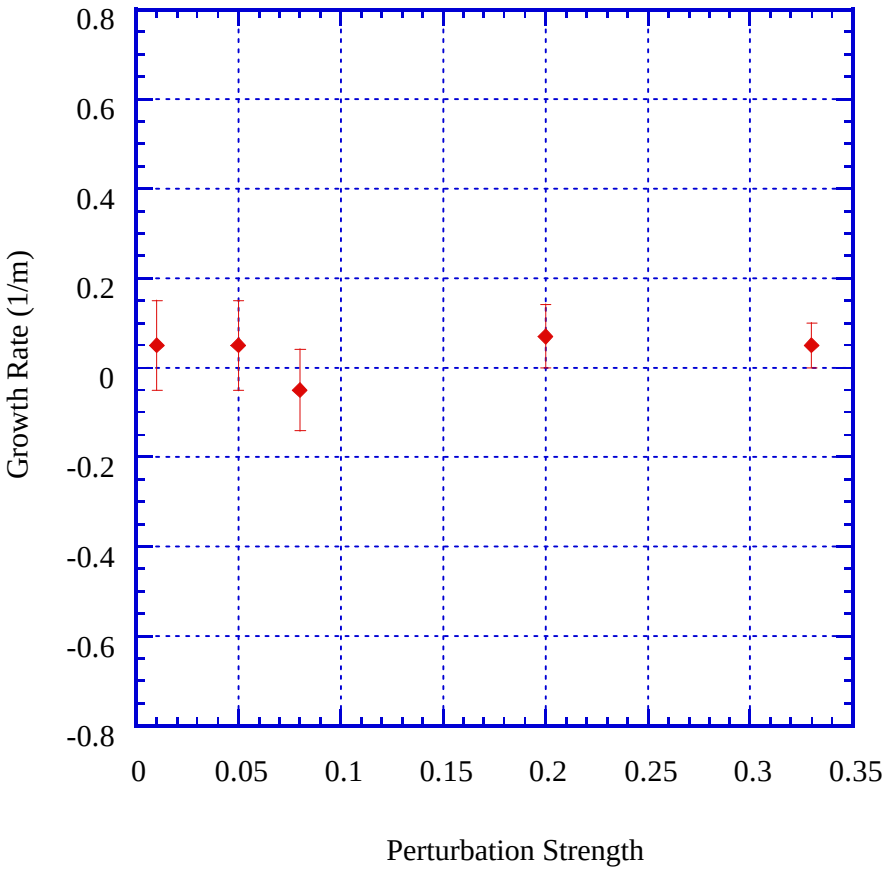

Figure 3. 17. Growth rate vs. perturbation strength for fast wave in a conducting pipe.

3.4 Summary

Experiments have been performed to study the resistive-wall instability in a space-charge-dominated beam. High-perveance electron beams with localized perturbations were launched from a gridded electron gun and transported through a short resistive-wall channel consisting of a resistive-film coated glass tube inside a long solenoid providing uniform focusing. The energy width of the space-charge waves developed from the perturbations was measured at both ends of the channel. The experiments have shown that, for the small initial perturbation the energy width of fast waves decreases, while the energy width of the slow waves increases. However, in the nonlinear regime (large initial perturbation), we found the energy width of fast space-charge wave grows. This apparently nonlinear effect was unexpected, and, to the best of our knowledge, no theory exists that would predict this phenomenon.

Chapter 4

Development of a High-Performance Retarding Field Energy Analyzer

4.1 Introduction

As was discussed in the introduction, in the advanced particle accelerators for many applications, the accelerated beams must have very low emittance and energy spread. While there have been many experimental and theoretical investigations of emittance growth, very little work exists on the sources and evolution of energy spread in such beams. At the University of Maryland, various experiments are being carried out to study space-charge-dominated electron beams. Some of these experiments, such as the resistive-wall instability experiment and the University of Maryland Electron Ring (UMER) [30] currently being constructed require detailed knowledge of the beam's energy spread. The initial energy spread of the beams from the thermionic gun and the growth of this energy spread in the beam transport line must be measured with good accuracy. For these applications, a high-resolution energy analyzer is a necessary. Due to its simplicity and high signal-to-noise ratio output, the retarding field energy analyzer becomes a natural choice for the low energy electron beam. However, in this kind of device, such as a parallel plate structure, space-charge forces, beam trajectories, mechanical

misalignment, beam mismatching, etc, often lead to poor resolution of the energy measurement. In this dissertation, we report on the design and test results of a cylindrical retarding field energy analyzer which greatly improved the resolution compared to a parallel-plate energy analyzer used previously in our experiments [7, 31].

4.2 Theory of Retarding Field Energy Analyzer

To characterize the energy spread of a low energy beam, two kinds of energy analyzer are usually used. They are dispersion type and retarding field type. Due to its simplicity and high transmission rate, retarding field energy analyzer has been widely used. A typical application that uses a retarding field energy analyzer is ion microfabrication, where low energy, low current and high intensity ion is used. In the accelerator area, however, the retarding field energy analyzer is seldom used because the beam energy is usually much higher (from MeV to GeV). In UMER, we want to study the space-charge effect of intense beam and intentionally use a low energy beam (10 keV). Hence retarding field energy analyzer becomes a natural choice to characterize such kind of beam.

The simplest retarding field energy analyzer is the parallel plate energy analyzer. Figure 4.1a shows the most primitive form of the parallel plate energy analyzer. First, let us assume that the beam is ideal, that is, all the particle

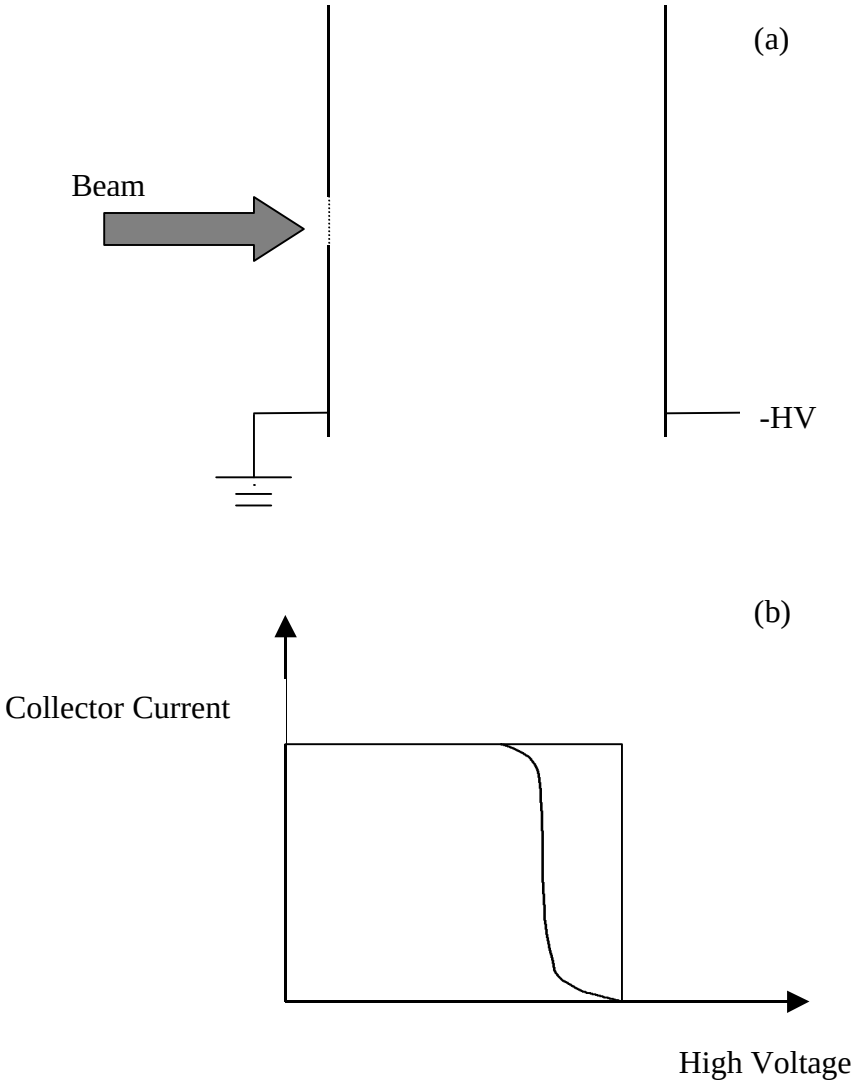

Figure 4. 1. (a) Primitive Parallel Plate Retarding Field Energy analyzer. (b) Responses of ideal and real energy analyzers to a monoenergetic beam.

trajectories are parallel to the beam axis. After the beam enters into the energy analyzer, the kinetic energy is converted into potential energy. Only those particles that have higher energy than the retarding voltage can reach the collector plate and appear as a current. Hence, if the beam is monoenergetic, the ideal response of the energy analyzer should have a sharp cut-off at the beam energy, as shown in the Figure 4.1(b).

In reality, the beam is never perfect. The real beam size is not infinitesimal small, nor has it zero divergence angle. In the case of parallel plate energy analyzer, the finite beam size is not a problem, but the finite divergence angle will cause problem. Suppose the beam divergence angle is θ, then the axial energy is related to the total beam energy by

$$E_{\parallel} = E_t (\cos q)^2 . \qquad (4.\ 1)$$

Because only the axial part of the kinetic energy is useful to overcome the retarding potential, the starting cut off voltage would be below the beam energy by

$$\Delta E = E_t - E_{\parallel} = E \sin^2 q \qquad (4.\ 2)$$

This formula shows that the parallel plate retarding field energy analyzer has a fundamental resolution due to the divergence angle of the beam. Of course this resolution depends on the quality of the beam, the smaller divergence angle of the beam, the better resolution the energy analyzer has.

Besides the limitation due to the beam trajectories, the energy analyzer also suffers from other limitations of the resolution. If we look at the structure of Figure 4.1(a), there is an aperture on the first plate for the beam to go through. This forms an aperture lens [1], which will cause defocusing effect to the beam.

As shown in Figure 4.2, a common aperture lens has two electrical field ranges separated by three electrodes. The center electrode is set at voltage V, the first one is V_1, and the third one is set at V_2. The central plate has an aperture of radius a, through which electrons can pass. The electrical fields at two sides of the central plates are E_1 and E_2 respectively which, in general, are different. Using classical electron optics theory, it can be proved that this aperture, along with the different electrical field on the two sides of it, has a focal strength of [1]

$$\frac{1}{f} = \frac{E_2 - E_1}{4V}. \qquad (4.\ 3)$$

Here, V is the central plate voltage and f is the focal length of the aperture lens. Applying this formula to the case of the parallel plate energy analyzer, the formula for the focal strength is reduced to

$$\frac{1}{f} = -\frac{1}{4d}. \qquad (4.\ 4)$$

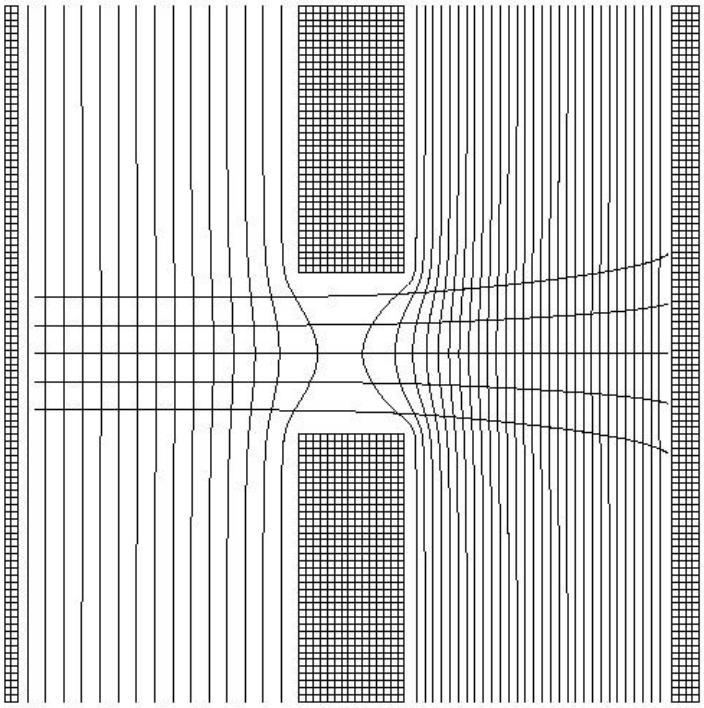

Figure 4. 2. Lens effect of an aperture in the plate. In this case, the lens is defocusing.

Here, d is the distance between two electrodes in Figure 4.1(a). The negative sign shows that the aperture has defocusing effect on the beam. After a parallel beam comes through the aperture, the beam has a divergence angle of

$$q = arctg(a / f) = arctg(a / 4d), \qquad (4.5)$$

where a is the aperture radius. This divergence angle is proportional to the aperture radius and inversely proportional to the distance between two plates of the energy analyzer.

To see the effect of this aperture lens, let us plug in some numerical numbers. For a typical energy analyzer built in our lab [7], a is equal to 2.4 mm, and d is 4.9 mm. It turns out the divergence angle is about 26^{o}, which will cause very poor energy resolution.

One way to overcome this problem is to use wire mesh covering on the aperture. From Equation (4.4), the mesh will not change the focal length of the aperture. The function of mesh is to subdivide the beam into many beamlets, each of which passes through much smaller apertures formed by the wire. Because the aperture is much smaller, even the focal length is still the same, the beam divergence angle can be reduced as predicted by Equation (4.5). By using mesh, we have an energy analyzer with much better resolution. The side effect of the mesh is that it is difficult to clean it, and might be harmful to the ultra high vacuum system. However, in some cases, it is necessary to use the mesh to reduce the aperture effect of the hole.

From the previous analysis, if we want to measure the beam energy spread, a parallel plate analyzer will give apparently larger energy spread due to particle trajectories. However, this type of energy analyzer can still measure the highest beam energy accurately, because there are always some particles moving along the axis. In reality, as we will see later, the real parallel plate energy analyzer is little bit different from the primitive one. The main difference is that the real one has separate high voltage plate and collector. There is an extra collector behind the high voltage plate to avoid the high voltage difficulty of the electronics.

Besides the parallel plate energy analyzer, there are also other variations of the retarding voltage energy analyzer. One is spherical type energy analyzer, called spherical-condenser analyzer [32]. If the beam has infinitesimal size and finite divergence angle, like the beam emitted from a point source, the spherical energy analyzer will have very good results. This kind of analyzer has found application in the areas like photoelectric and field emission, where the sources are close to spherically symmetric.

Reference [32] presents a systematic analysis of the performance of this kind of analyzer. Here, I only summarize some of the results. The usual geometry takes the forms of two concentric semi-spheres, as being illustrated in Figure 4.3. The radius of two spheres are a and b respectively. The beam trajectories are much more complicated than those in the parallel plate analyzer. However, due to its symmetric geometry, the analytical solution is still solvable. The typical trajectory

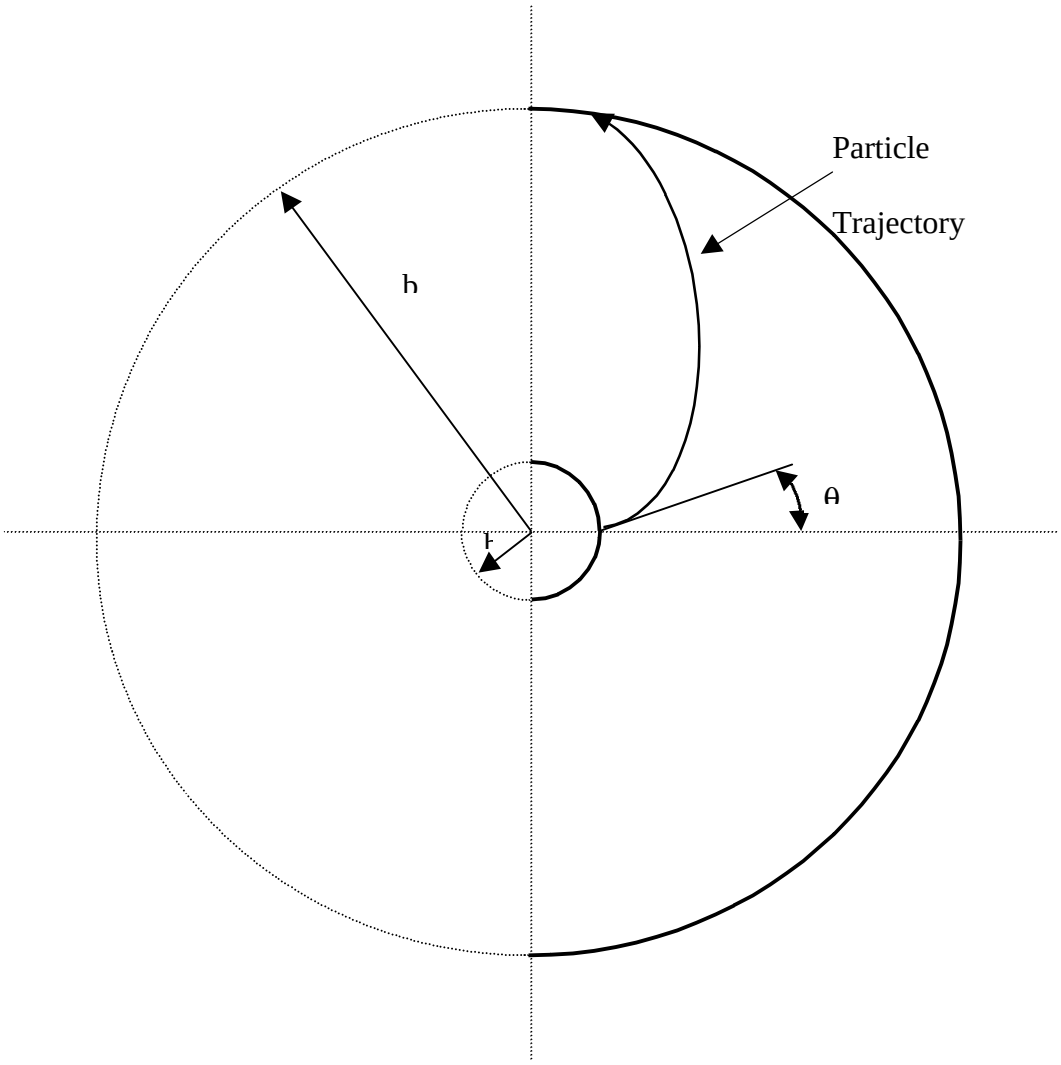

Figure 4. 3. Spherical energy analyzer

path is an ellipse. If the particle incident angle is too large, the particle can not be collected by the outside sphere. The largest angle that the particle could have is determined by the following equation

$$\sin^2 q_m = e/(2h). \qquad (4.6)$$

Here $h = (b-a)/b$ and $e = eV/(\frac{1}{2}mv_0^2)$. This results the resolution of the energy analyzer as

$$\Delta E/E = 2ab^{-1}\sin^2 q_m. \qquad (4.7)$$

Unlike a parallel plate energy analyzer, even for the parallel beam of radius $r_{0,}$ the energy analyzer has a finite resolution

$$\Delta E/E = \frac{2r_0^2}{ab}. \qquad (4.8)$$

From Equations (4.2) and (4.8), we found that the parallel-plate energy analyzer has better resolution for parallel beam while the spherical type has better performance for point source beam.

The cylindrical energy analyzer is a compromise between the parallel plate energy analyzer and spherical energy analyzer. As illustrated in Figure 4.4, the second electrode of the cylindrical energy analyzer is a cylinder. This is a special case of a normal bipotential lens and can focus the beams strongly according to the analysis in reference [1]. The cylindrical energy analyzer has relatively

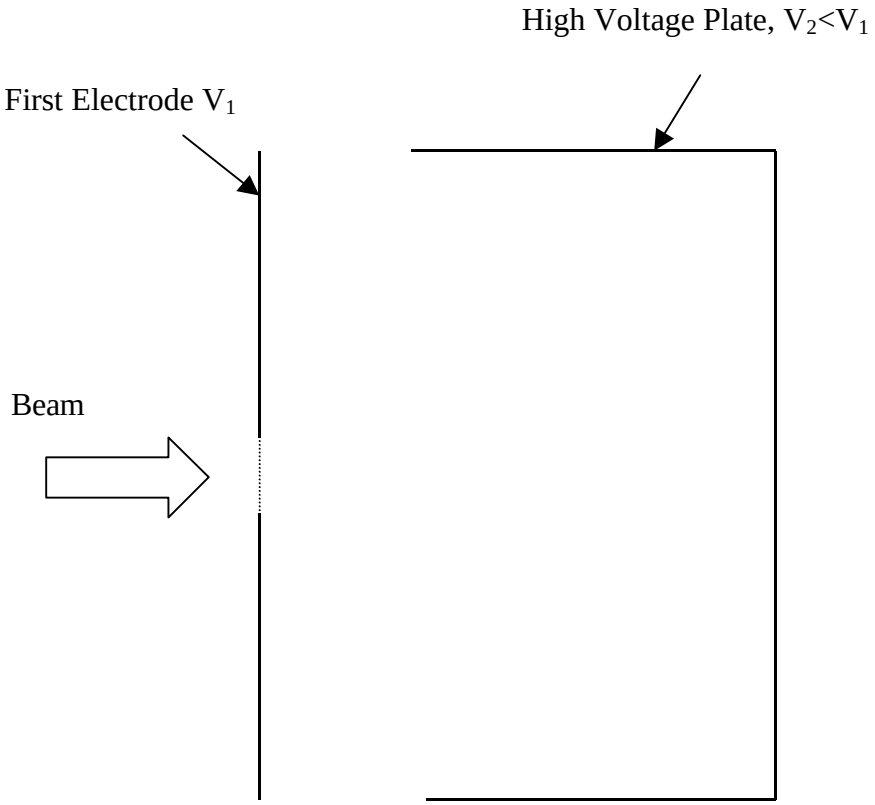

Figure 4. 4. Cylindrical retarding voltage energy analyzer

good performance for a beam with large size and finite divergence. The analytical solution for the resolution of the cylindrical analyzer is not quite tractable. So we must rely on the computer simulation, which will be described in the next section. Table 4.1 summarizes the performances of three types of energy analyzer.

Table 4. 1. Comparison of the performances of different energy analyzers

Type of Energy Analyzer	Large Beam Size	Large Beam Divergence Angle
Parallel plate energy analyzer	Good	Poor
Spherical energy analyzer	Poor	Good
Cylindrical energy analyzer	Good	Good

It is worth noting that, besides these three types of energy analyzer mentioned above, there are also other types of retarding field energy analyzer. One example is the einzel lens energy analyzer, which is more complicated and more flexible for different applications.

4.3 Design of a Compact, High-Performance Energy Analyzer

The accurate measurement of energy spread of the electron beam is difficult. In our group, several people have tried to measure the energy spread of the beam. But they were puzzled to find that the measured energy spread from the electron beam is much larger than predicted by theory, ranging from 20 eV to around 50 eV

[7, 31]. These measurements raise the question: what is the real energy spread of the beam from an electron gun?

Careful study of their experiments found that all of them used parallel plate energy analyzer. As was discussed in the previous section, the parallel plate is only good for a parallel beam. In our case, when electrons are emitted from the electron gun, the beam has a finite divergence angle. If we use the parallel plate energy analyzer to measure the energy spread, the resolution will be poor. The real beam energy spread will be masked by the apparently large energy spread due to the coherent transverse beam motion.

To study the performance of the energy analyzer, a computer code called SIMION is used. The SIMION is a single particle code, widely used in the semiconductor industry. Finite element method is used to solve the field equations. User can define any shape of the electrode and the voltage associated with the electrode. The voltage on each electrode is adjustable even after the field calculation is done. Wire mesh can also be simulated in the program.

A parallel plate energy analyzer developed by H. Suk was simulated. The actual dimensions were taken from his dissertation [7]. Figure 4.5(a) shows the structure of the energy analyzer and the beam trajectories. This energy analyzer consists of two electrically isolated parallel plates and a Faraday cup. Both plates have a hole with diameter of 4.8 mm and the distance between two plates is 4.9 mm. The holes are covered with wire mesh to produce a uniform electric field.

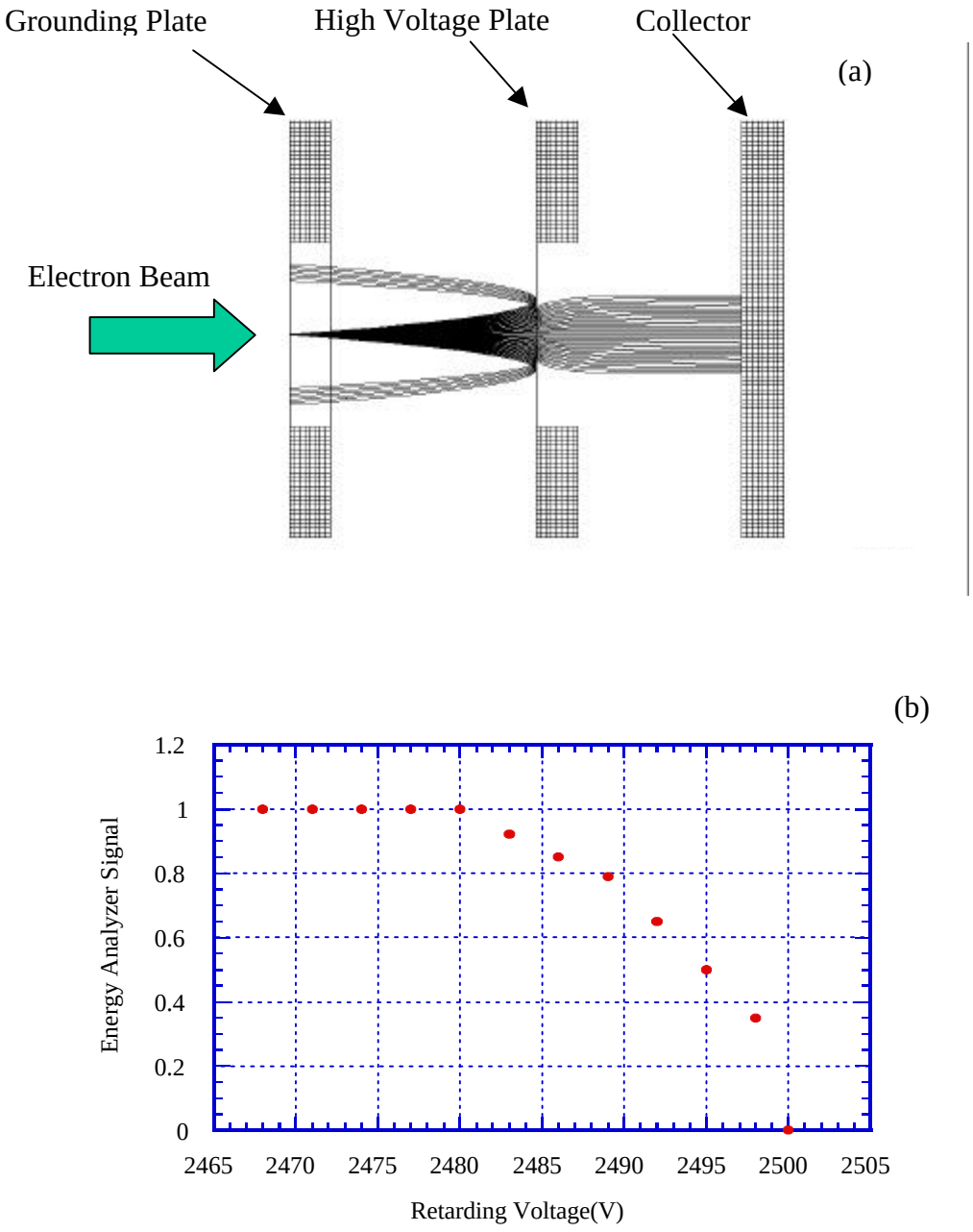

Figure 4. 5.(a) Geometry of the old energy analyzer and particle trajectory. Retarding voltage is –2.490 kV. Beam energy is 2.5 keV. (b) Simulated performance of energy analyzer for a 2.5 keV beam.

In the figure, the beam is mono-energetic with beam energy of 2.5 keV and divergence angle of -5^o to 5^o. Only those particles which have axial kinetic energy larger than the retarding potential can pass the retarding plate and form a current at the collector. If we change the high voltage on the second plate, the collector current will change. From this collector current vs high voltage curve, the beam energy profile could be constructed. Figure 4.5(b) shows the simulated performance of this energy analyzer. Even for a monoenergetic beam, this energy analyzer has a resolution of 20 eV, which gives $\Delta E/E_0$=0.8%. This is the same order as the energy spread measured by the previous experiments.

Based on above analysis, a new energy analyzer is designed with much better resolution. The ideal is to use curved equipotential lines to give transverse focusing to the beam. Cylindrical geometry is chosen because of the following reasons. First, the spherical energy analyzer is not appropriate for the large beam size. Reducing the hole diameter of the first plate will help, but it will reduce the signal to noise ratio. Second, cylindrical geometry is much easier for mechanical machining and mesh installment.

Figure 4.6 shows the schematic of this energy analyzer. The equipotential lines and typical beam trajectories are also shown in the figure. The whole energy analyzer is enclosed in a metal shell for signal shielding. The first grounding plate

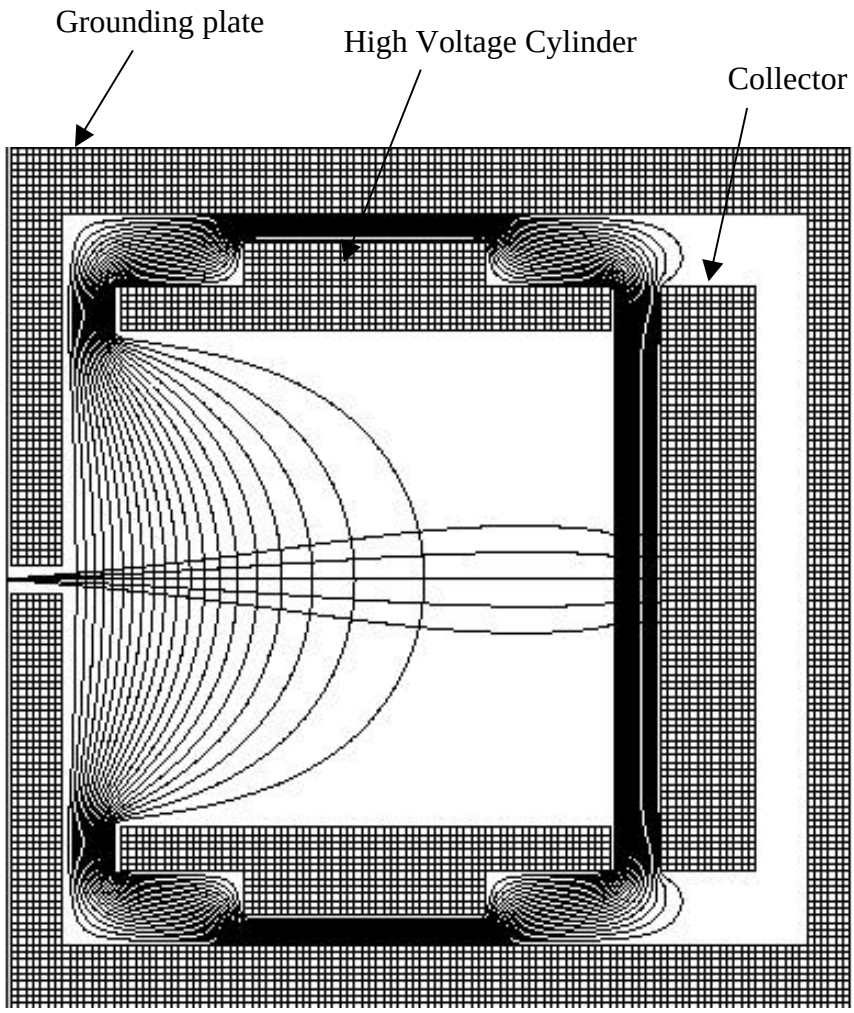

Figure 4. 6. Schematics of cylindrical energy analyzer with equi-potential lines and typical particle trajectories.

has a hole of diameter 1mm. Second electrode is a cylinder covered with wire mesh at the rear end. The third one is a collector. From the figure, we can see that, due to the curved equipotential lines, particles can be focused in the energy analyzer. Nearly all beam kinetic energy can be used to overcome the retarding potential. When the retarding voltage is low, all particles can pass through. With higher retarding voltage, more and more particles are reflected. Figure 4.7 shows this picture at different retarding voltages. All the particles are reflected at the beam energy. The simulated performance of this energy analyzer is shown in Figure 4.8. The beam is the same as in previous simulation. Results from both energy analyzers are shown in the figure. We can see that the new one has a very sharp cut off, which gives resolution of 0.6 eV, instead of 20eV in the old one. It is interesting to note that at different beam energies, the energy analyzer resolutions are different. The higher is the beam energy, the poor resolution the energy analyzer has. Figure 4.9 gives the energy analyzer resolution at 2.5 keV, 5.5 keV and 10 keV.

Figure 4.10 shows the design of this energy analyzer. The high voltage cylinder is supported by two macor rings, which is a very good insulator material. For the electron, there is a reverse electrical field on the collector to suppress the second emission. So we just use a single plate, instead of a Faraday Cup, as the collector. The collector is made of copper and others are made of stainless steel. Some holes are deliberately made for better vacuum pumping.

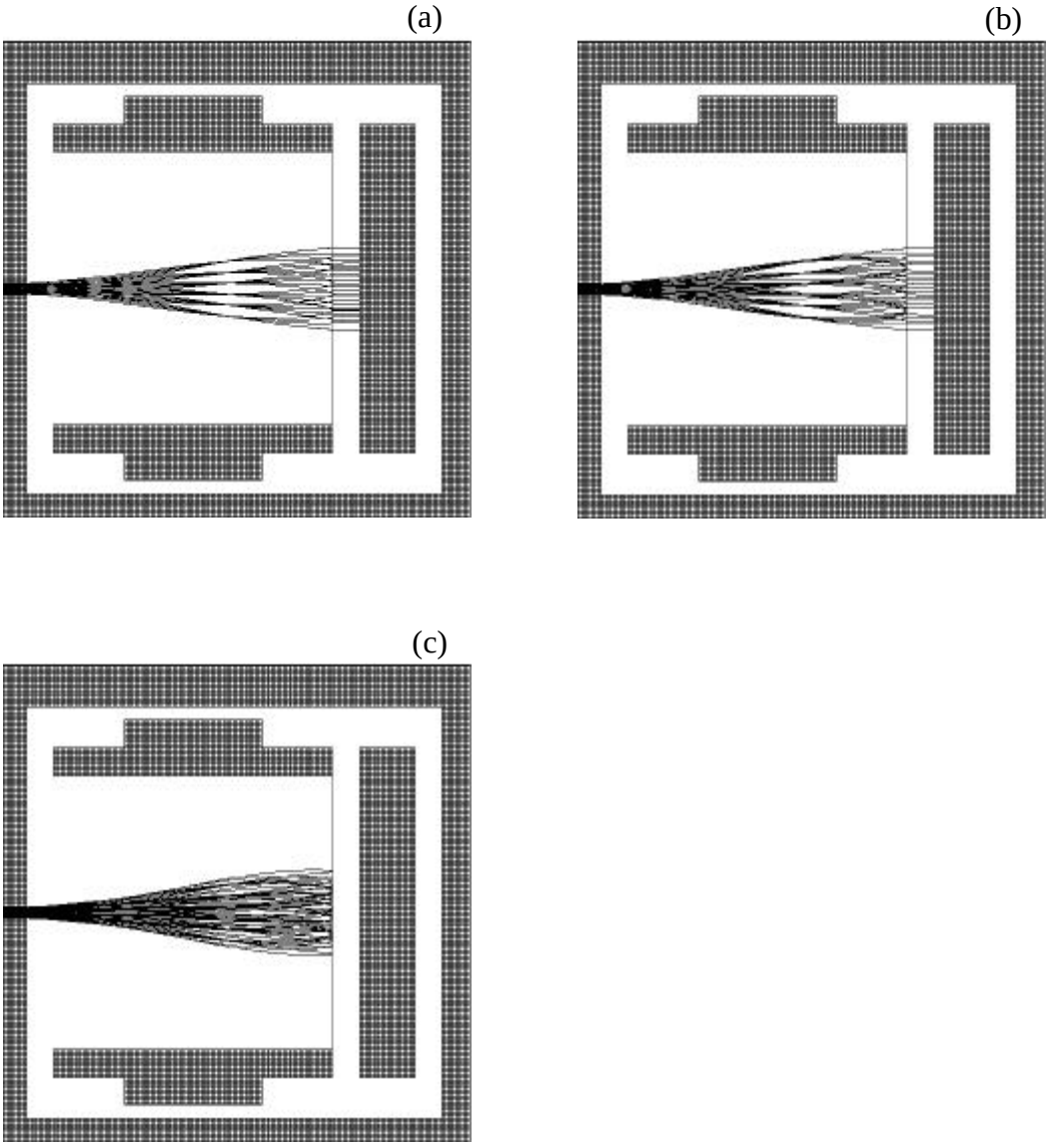

Figure 4. 7. Beam trajectories at different retarding voltages. Beam energy is 2.500 keV. (a). Retarding voltage is 2.4994 keV. (b) Retarding voltage is 2.4997 keV. (c). Retarding voltage is 2.500 keV.

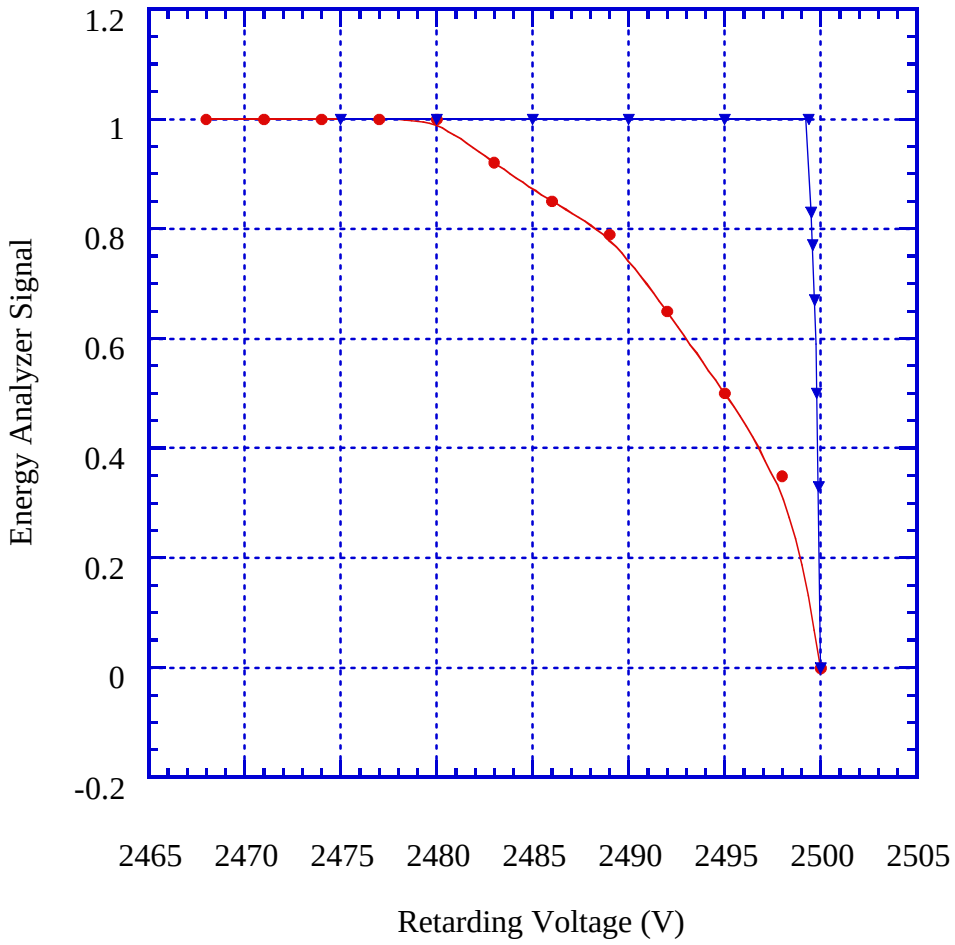

Figure 4. 8. Simulation shows that, for the beam with divergence angle of 5^{o}, the old one has resolution of 20eV, while the new one has resolution of 0.6eV.

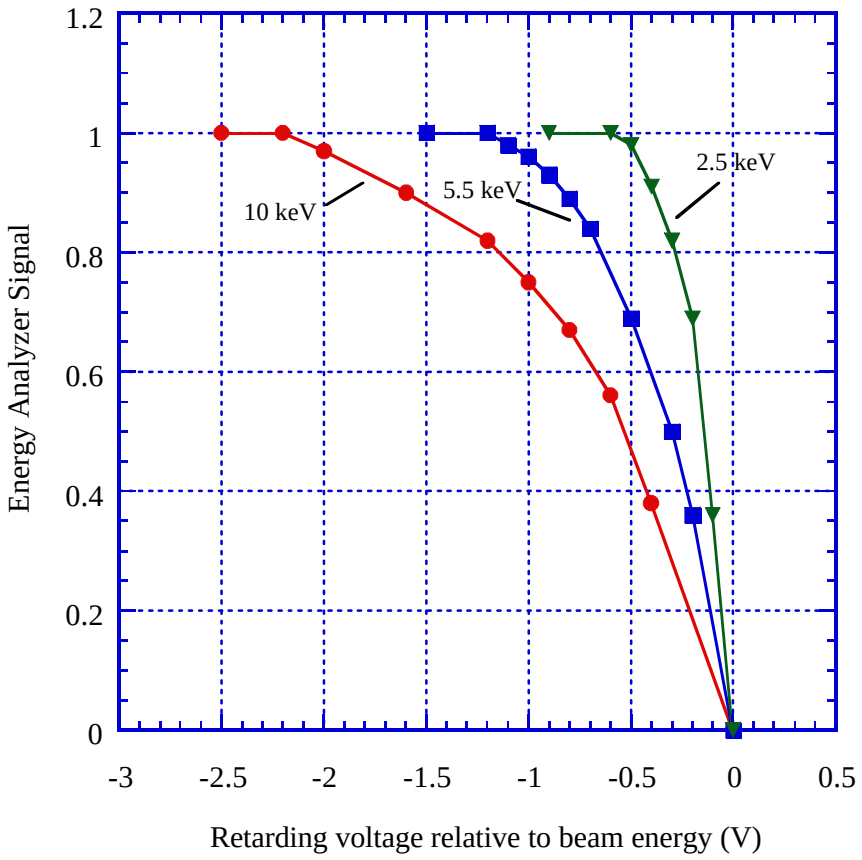

Figure 4. 9. Energy analyzer responses to a monogenetic beam at different beam energy of 2.5 keV, 5.5 keV and 10 keV.

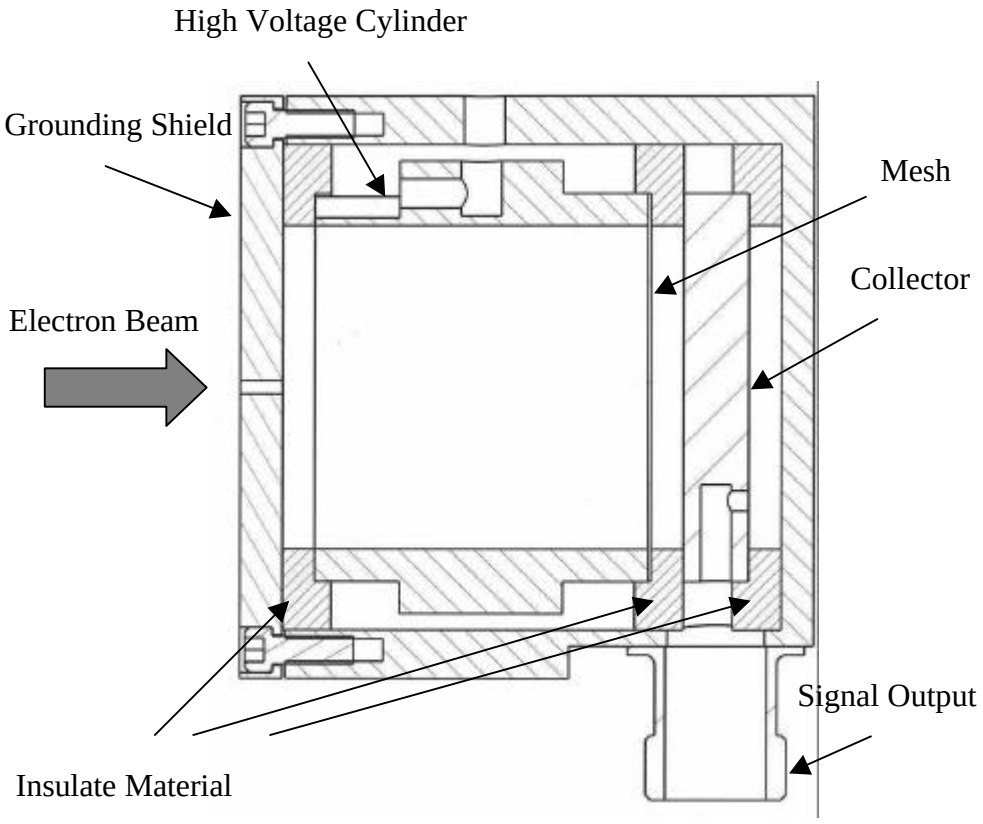

Figure 4. 10. Cross Section of new energy analyzer with cylindrical high voltage electrode.

4.4 Beam Test of the New Energy Analyzer

4.4.1 Electron Gun Commissioning

In this experiment, the electron gun is the same as in the resistive–wall experiment; but a new cathode is used. After commissioning, two experiments are carried out to characterize the electron gun. The first experiment is to measure the electron gun emission vs. filament heating power curve. This will help us to find the optimized heating power for the cathode. If the heating temperature is too low, the cathode is not uniformed heated and has poor emission. If the heating temperature is too high, the emission will level off and the life-time of the cathode will be much shortened. Because it takes long time for the cathode to reach the thermal equilibrium, every time when we set different heating voltage, we have to wait half an hour or longer for thermal equilibrium. Figure 4.11 shows the results of the experiment. In the figure, the horizontal axis is the heating power and the vertical axis is the electron gun current. The emission increases rapidly between 3.5 and 4 W of the heating power. After that point, the curve levels off. The cross indicates the normal operating temperature, which corresponds to the heating voltage of 6.6V. It is worth noting that the gun emission also depends on the vacuum. Higher vacuum can result in better gun emission and longer cathode life-time. In this experiment, the vacuum is kept at high 10^{-9} Torr.

The second experiment to characterize the electron gun is to study the gun emission current vs beam energy at fixed A-K distance, 19 mm in the experiment.

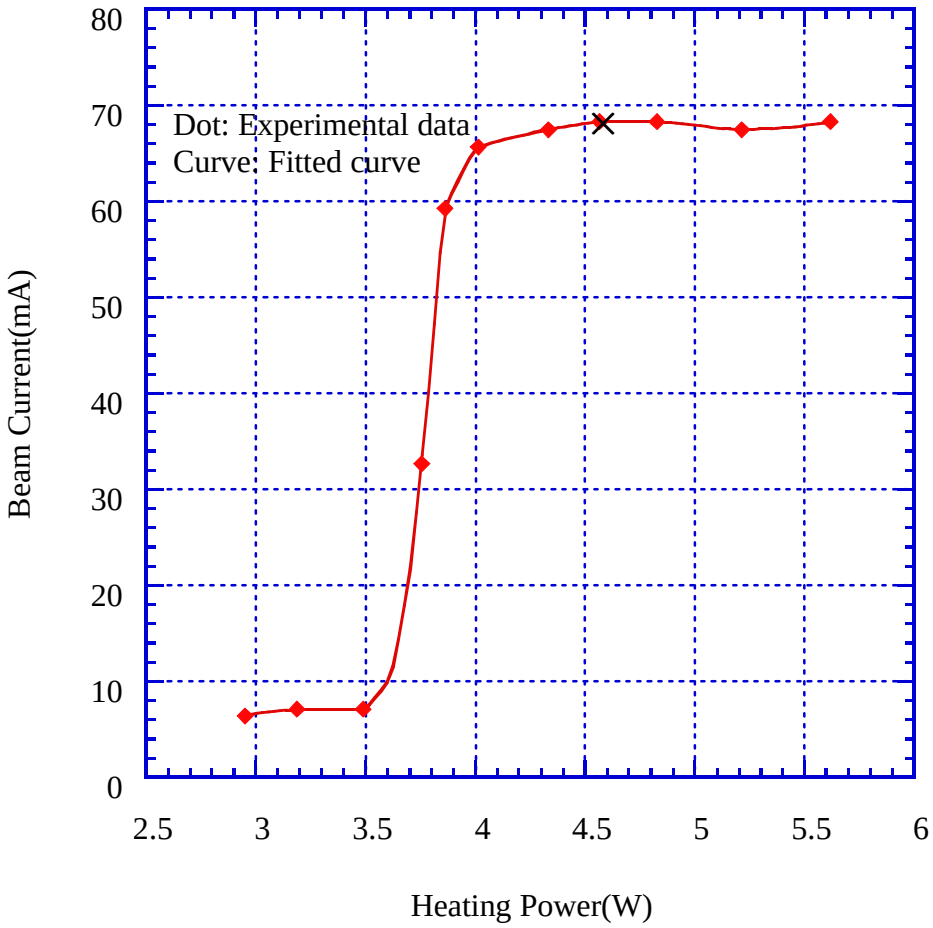

Figure 4. 11. Cathode emission vs heating power. Electron gun anode voltage 3 kV, the A-K distance is 19mm. Normal operating point corresponds to the heating voltage of 6.6V.

In this case, the heating voltage is set at 6.6 V, which is the normal operating voltage determined previously. Figure 4.12 shows the results. In the figure, the horizontal axis is the beam energy and the vertical one is the beam current. This curve fitting shows that the beam current increases with the energy by power of 1.2. Ideally, this curve should follow Child-Langmuir law [44, 45], that is, the current increases with the beam energy by the power of 1.5. This is based on the one-dimensional model and planar-diode geometry. In this gun, due to this different geometry, the emission is lower than this Child's law limit.

The third test is to measure the beam current change vs the A-K distance. The beam energy is fixed at 4.5 kV. Figure 4.13 shows the results. In the figure, the current changes with the A-K distance by inverse power of 1.6. Again, this is lower than the ideal case of inversely squared curve.

4.4.2 Experimental Apparatus

The experimental set up is shown in the Figure 4.14. Beam is emitted from the electron gun and is focused by two solenoids down stream. The energy analyzer is inside the first diagnostic chamber. A linear and rotation motion is used to adjust the position of the energy analyzer accurately. Two solenoids are the same as in the resistive-wall experiment. The distance of two solenoids and energy analyzer from the electron gun is 9.1cm, 21.6 cm and 33.2 cm respectively. Figure 4.15 is one example of the beam envelope in the transport line. Currents for the first and

second solenoids are 3.6 A and 4.7 A respectively. We can see that the energy analyzer is sitting at the waist of the beam.

4.4.3 Test Results

Figure 4.16 is a typical signal output from the energy analyzer. In the figure, the beam energy is 5 keV and the beam pulse length is 100 ns. From the signal, we can see that this energy analyzer has pretty fast rise time (~2 ns) and can reproduce the beam waveform faithfully.

The way to measure the energy spread of beam is to adjust the retarding voltage and, by constructing the change of the beam current with the retarding voltage, we can get the beam energy profile information. Figure 4.17 shows such a case. In the figure, different traces corresponding to different retarding voltage are plotted together. The traces of larger index number correspond to higher retarding voltage. From this figure, the beam energy spread can be reconstructed, as shown in figure 4.18. In this figure, the vertical axis is the beam current at the center of the pulse and the horizontal axis is the retarding voltage. By taking the difference of the data, the beam energy profile can be plotted, which is shown in figure 4.19. In this example, the beam energy and current is 2.5 keV and 60 mA respectively. The measured beam rms energy spread is 1.8 eV.

Tests are also performed at different beam energies. Figure 4.20 shows the beam energy spread change with the beam energy. Notice, in this case, the beam

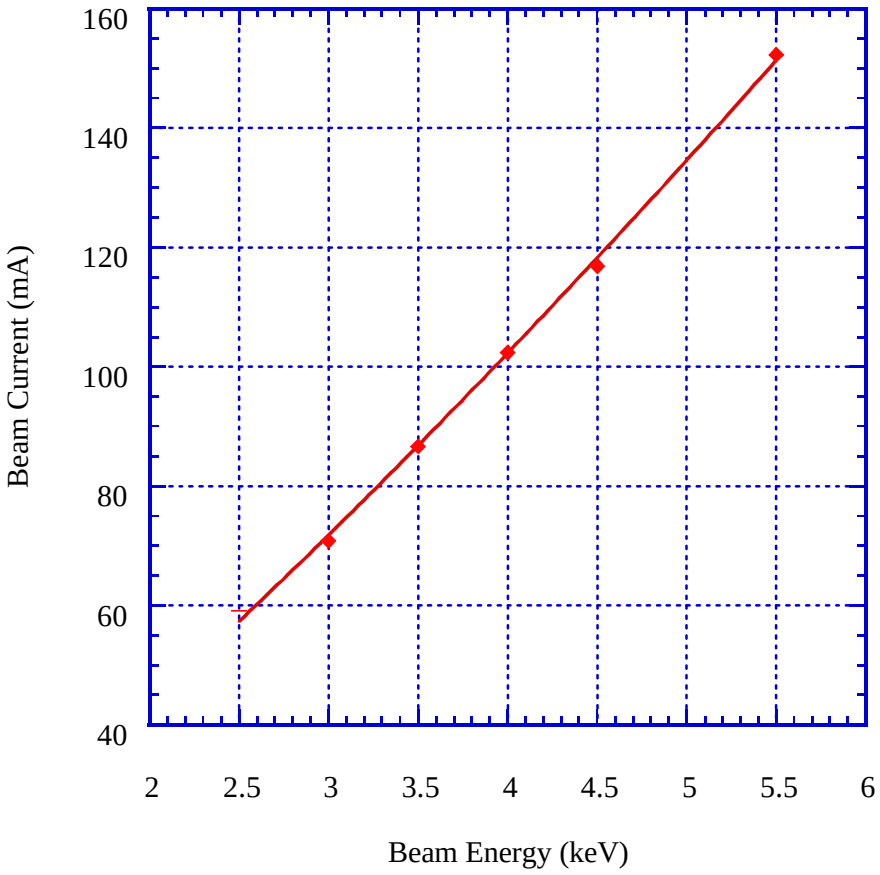

Figure 4. 12. Beam current vs beam energy. The curve shows that the beam current changes with beam energy by power of 1.2.

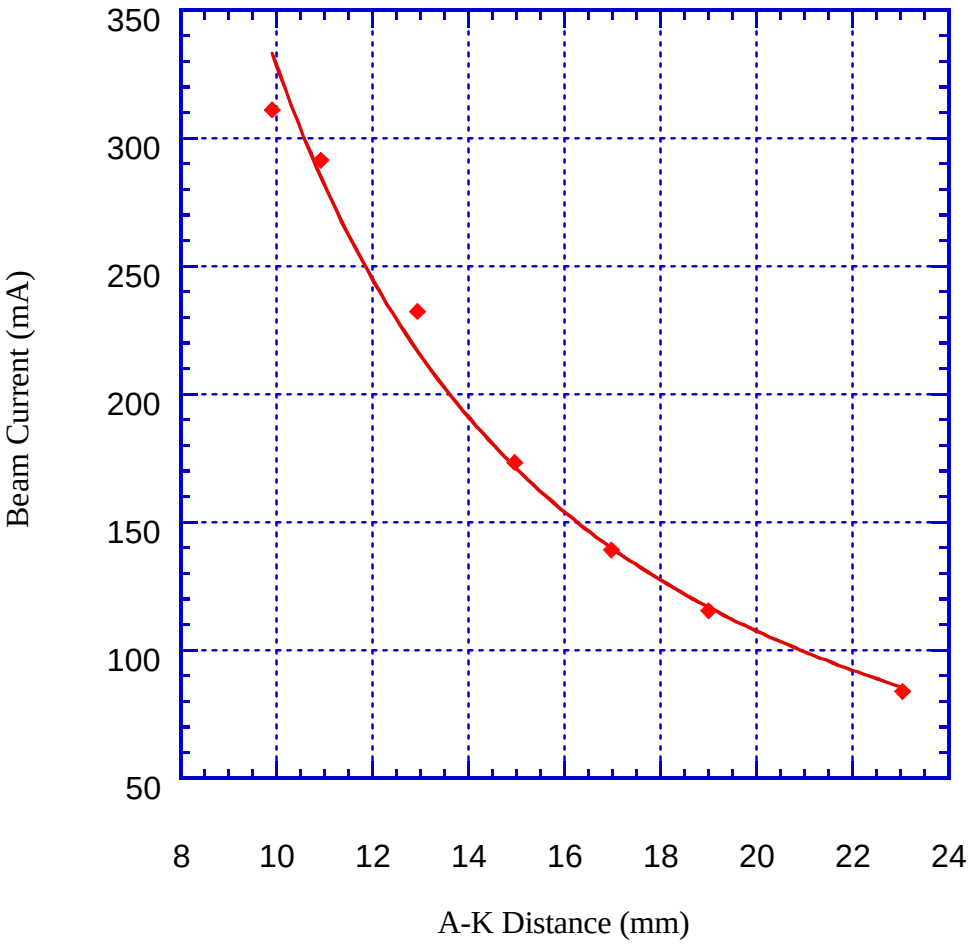

Figure 4. 13. Electron gun emission current vs A-K distance. The curve fitting gives that the current changes with the distance by inverse power of 1.6.

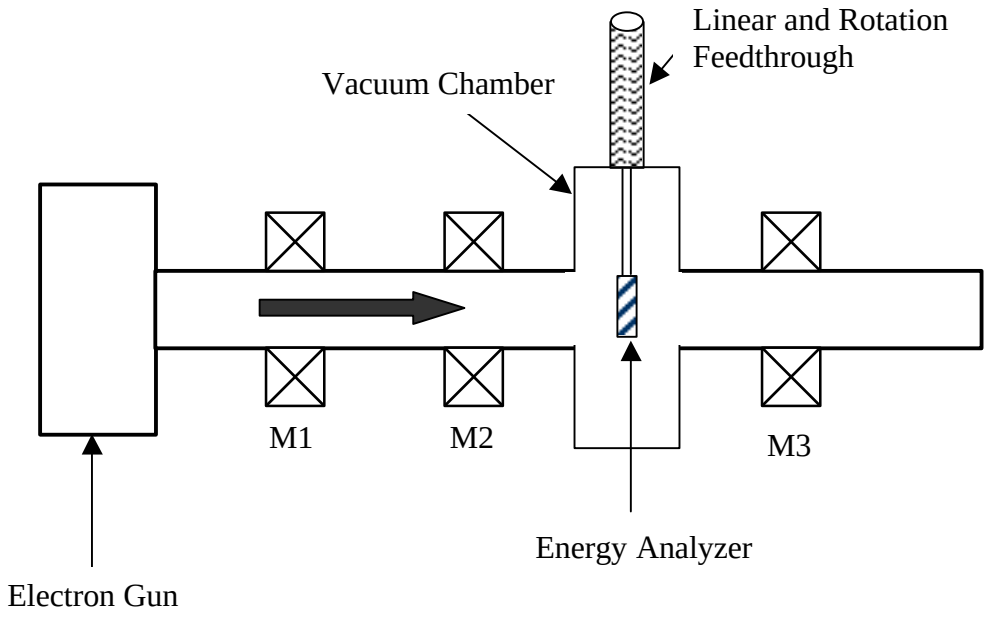

Figure 4. 14. Experimental setup for the energy analyzer test. M1, M2 and M3 are the three solenoids.

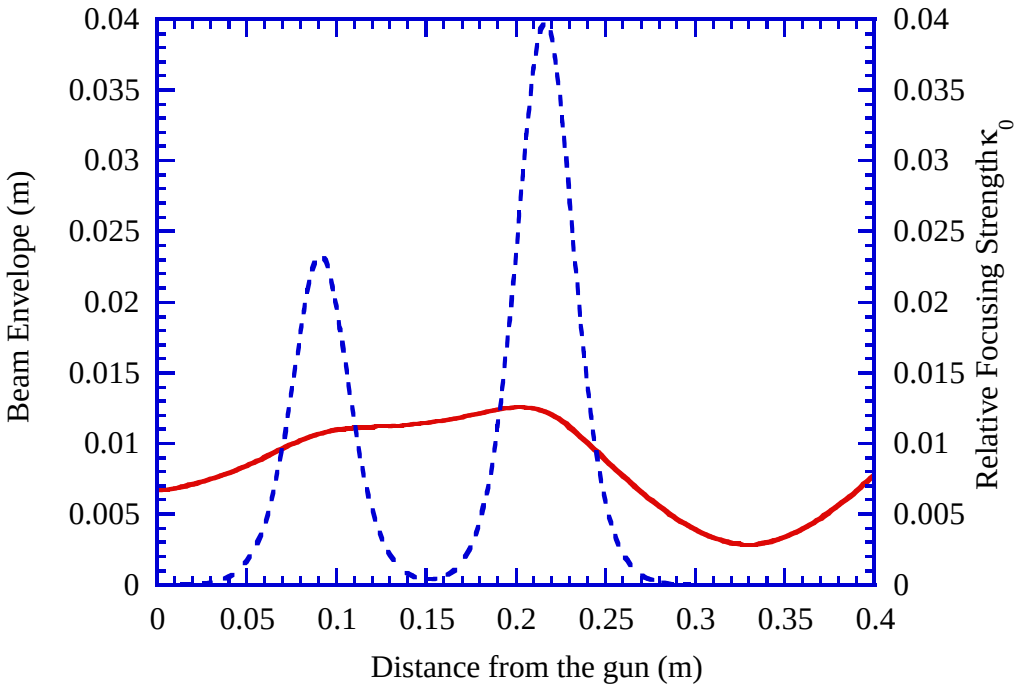

Figure 4. 15. Beam envelope in the transport channel. The relative focusing strength of the solenoids are also shown. Beam energy is 3.5 keV. Beam current is 87.9 mA. The energy analyzer is at the waist of the beam.

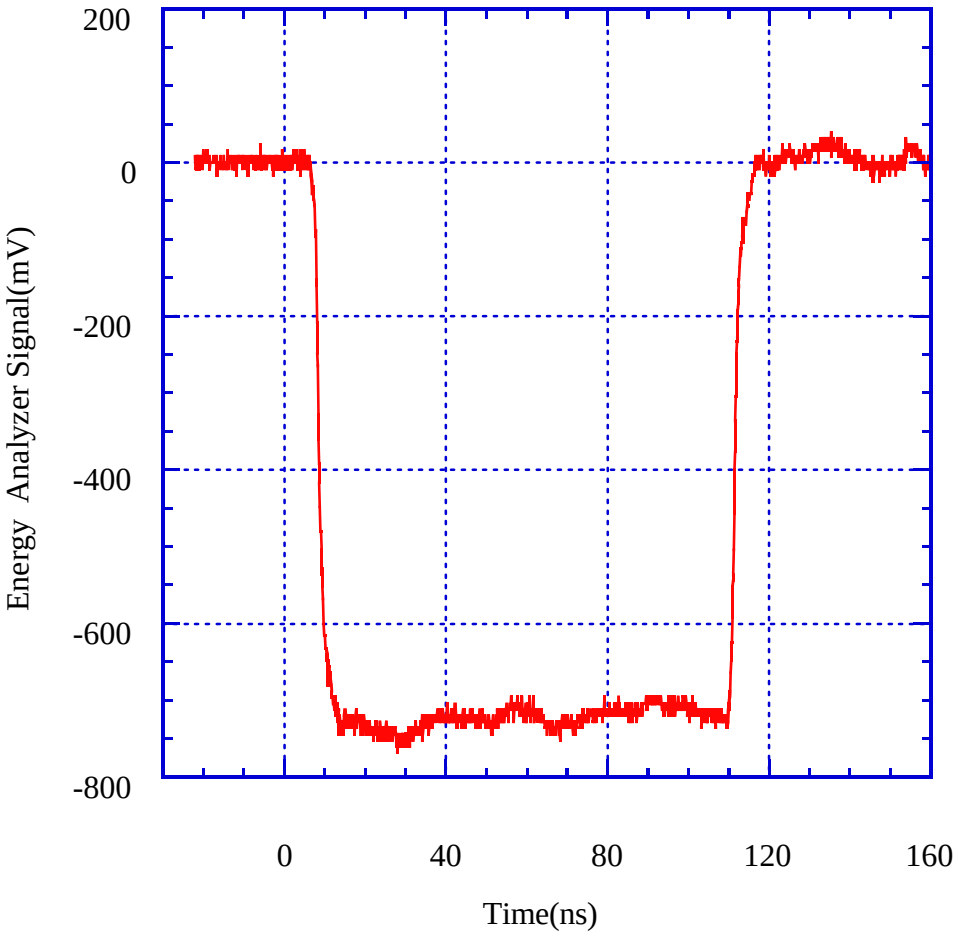

Figure 4. 16. Typical energy analyzer signal. The beam current pulse length is around 100ns. The rise time of the energy analyzer signal is 2ns.

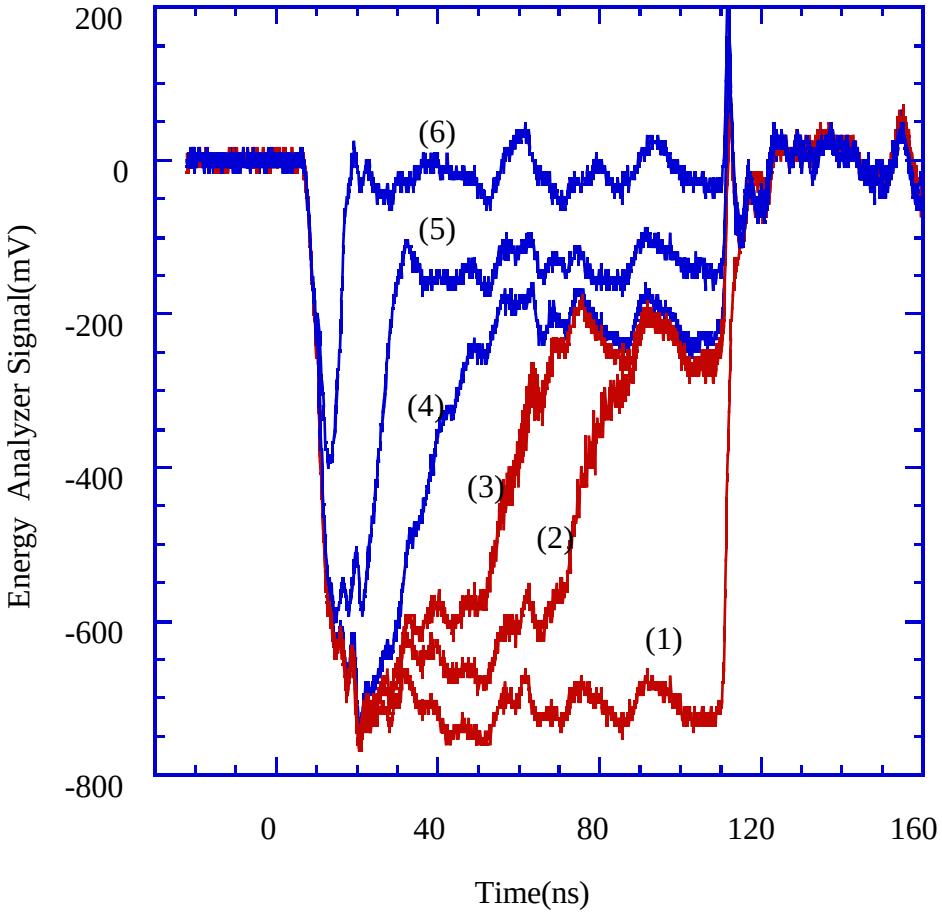

Figure 4. 17. Different beam current waveforms at different retarding voltages. Six waveforms are shown in the figure.

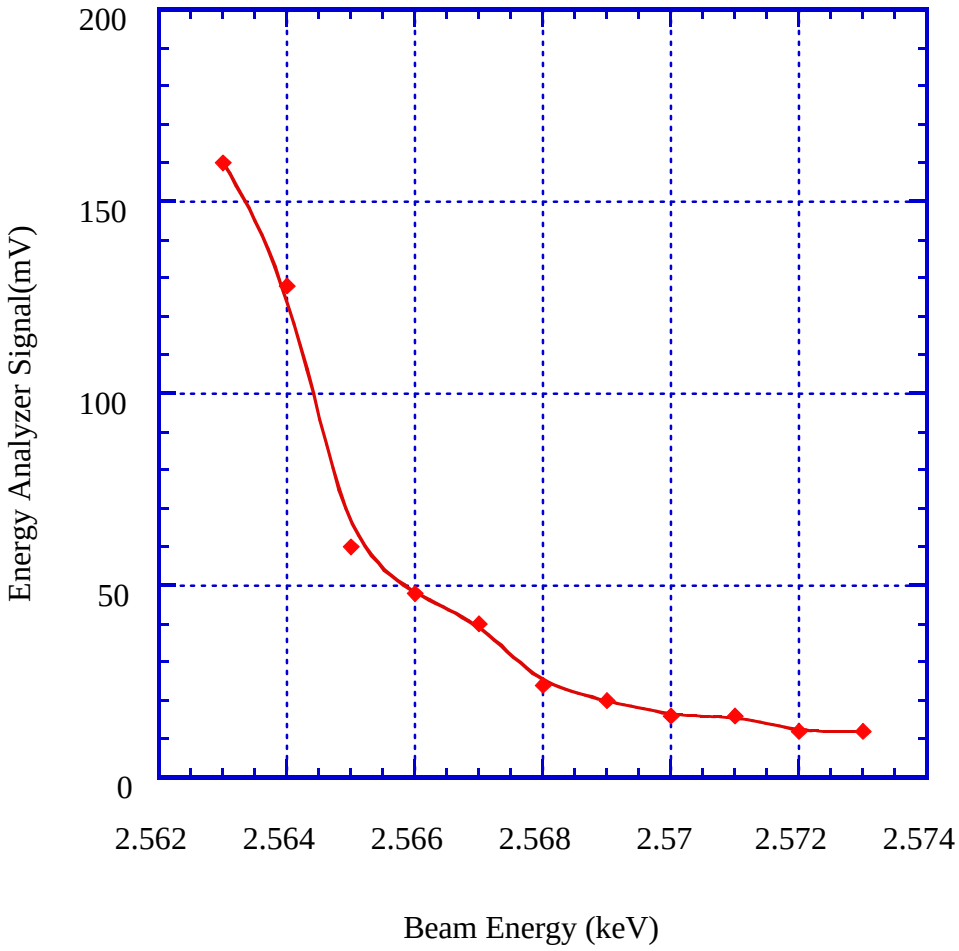

Figure 4. 18. The energy analyzer signal vs beam energy.

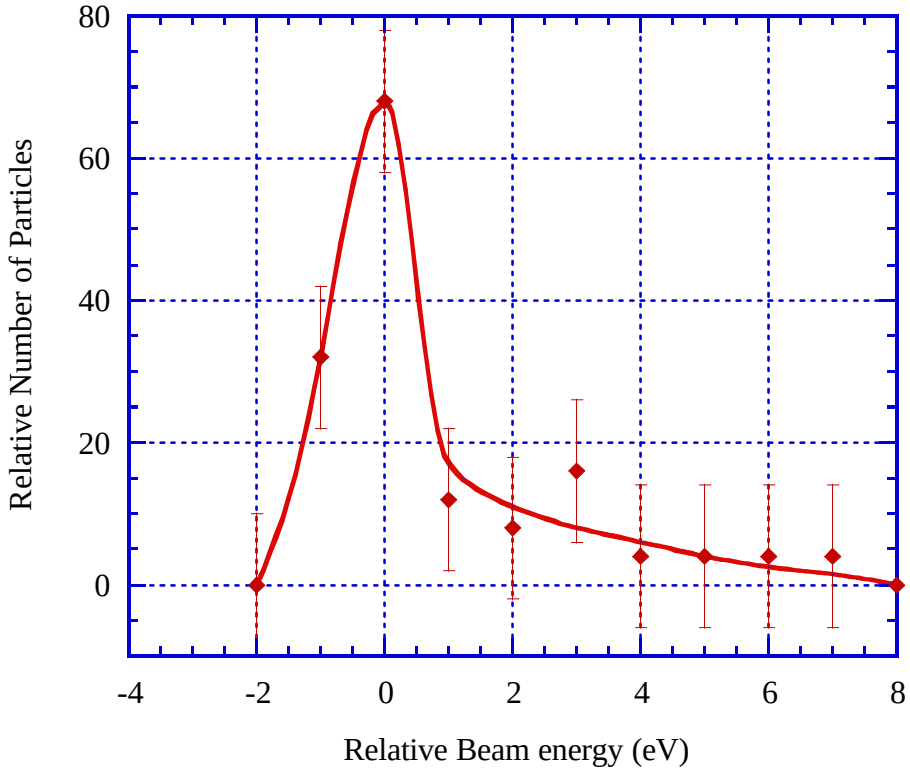

Figure 4. 19. Beam energy distribution for a beam with energy 2.5 keV. The rms energy width is 1.8 eV.

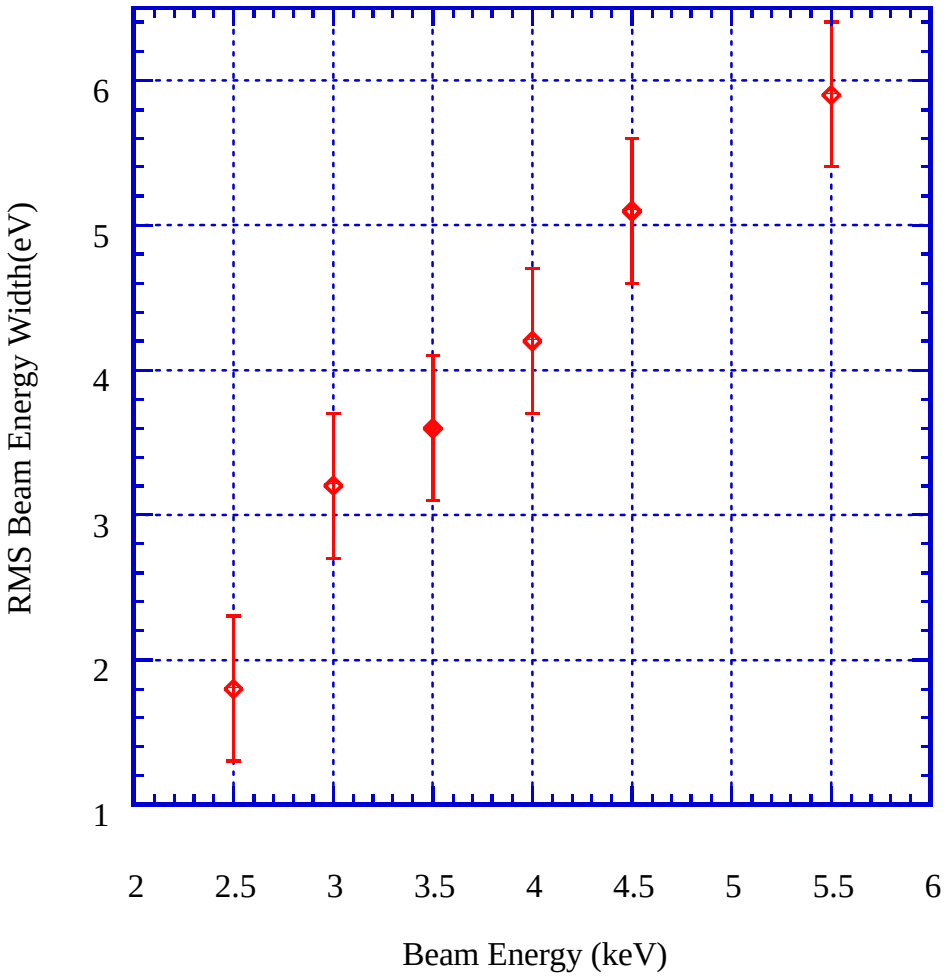

Figure 4. 20. Beam energy width dependence on the beam energy.

current is not fixed. By Child's law, the beam current increases with the beam energy as shown in Figure 4.12.

4.5 Theoretical Considerations of the Sources of Beam Energy Spread

The theoretical understanding of the evolution of energy spread in a beam is very complicated and not complete. There are different papers and books describing the energy broadening in a charged-particle beam [1, 31, 33-35]. Here I give a brief review of two dominant sources of the energy spread and compare them to the measurements in our experiment.

4.5.1 The Boersch Effect

When the beam is emitted from the cathode, it has energy spread due to the cathode temperature. The rms beam energy spread is related to the temperature by

$$\Delta E_{rms} = \Delta\tilde{E} = m v_{rms}^2 = k_B T . \qquad (4.9)$$

Here, v_{rms} is the rms thermal velociy, k_B is the Boltzmann's constant and T is the beam temperature.

When the beam is accelerated by an electric field, every particle will gain longitudinal kinetic energy. Suppose two particles having an energy difference ΔE in the beginning. They will still have the same amount of energy difference ΔE

after acceleration. However, their velocity difference will change. To see the difference between the velocity spread and energy spread, consider two non-relativistic particles, one with initial velocity v_{1i}, and the other one with initial velocity $v_{2i}=v_{1i}+\Delta v_i$. When they are accelerated through an acceleration gap of voltage V_0, the two particles will have final kinetic energy of

$$\frac{1}{2}mv_{1f}^2 = \frac{1}{2}mv_{1i}^2 + qV_0 \qquad (4.\ 10a)$$

and

$$\frac{1}{2}mv_{2f}^2 = \frac{1}{2}mv_{2i}^2 + qV_0 = \frac{1}{2}m(v_{1i} + \Delta v_i)^2 + qV_0 . \qquad (4.10b)$$

The difference of the velocity after the acceleration, Δv_f, is defined as

$$\Delta v_f = \sqrt{(v_{1i} + \Delta v_i)^2 + 2qV_0 / m} - \sqrt{v_{1i}^2 + 2qV_0 / m} \qquad (4.\ 11)$$

By expanding both equations and assuming Δv is much smaller than the mean velocity, we find that

$$\Delta v_f = \Delta v_i \frac{v_{1i}}{v_{1f}} . \qquad (4.\ 12)$$

From this relation, we find that the velocity difference between the particles is smaller after the acceleration. Because the random velocity distribution is related to the temperature, this effect is called the longitudinal cooling of the beam due to acceleration [1].

This can also be viewed from the relation between the energy spread and the temperature. Initially, the beam energy spread is given by Equation (4.9). After acceleration, the beam thermal energy spread is [1]

$$\Delta\tilde{E}_f = \sqrt{2qV_0 k_B T_{\|f}} \ . \qquad (4.13)$$

Here, V_0 is the accelerating voltage, $T_{\|f}$ is the longitudinal temperature after acceleration. Because the energy spread in the lab system is the same before and after the acceleration, equating Eqs.(4.13) and (4.9), we find that

$$k_B T_{\|f} = \frac{(k_B T_{\|i})^2}{2qV_0} \ . \qquad (4.14)$$

Here, $T_{\|i}$ is the initial beam temperature, which is isotropic (i.e. $T_{\|i}=T_{\perp i}=T$) before the acceleration. This longitudinal cooling effect is very significant. For example, if initially the beam has a cathode temperature of 1100^{o} C, corresponding to a thermal energy of 0.1eV. After the electron beam has been accelerated to 5 keV, the longitudinal temperature is decreased to 1×10^{-6}eV, a reduction of temperature by a factor of 10^5!

Note that the transverse temperature is the same as the initial temperature since the acceleration acts only in the longitudinal direction. The longitudinal temperature becomes negligible compared to the transverse temperature. The beam is now in an extremely anisotropic state ($T_{\|i}<<T_{\perp i}$). Coulomb collisions and other processes will try to redistribute the beam velocity distribution into thermal

equilibrium. The transverse temperature is decreased while the longitudinal temperature is increased. The resulting beam longitudinal energy spread will increase. This thermal relaxation procedure is referred to as the Boersch Effect because Boersch was the first researcher to observe this effect [See Ref [1], Chapter 6].

The transverse-longitudinal temperature relaxation effect is very complicated in a real beam. For a simple case in which the beam propagates through a smooth focusing channel and has a constant radius, the temperature relaxation can be described by the following equations [1]

$$\frac{dT_{\perp}}{dt} = -\frac{1}{2}\frac{dT_{\parallel}}{dt} = -\frac{T_{\perp} - T_{\parallel}}{t} \quad . \tag{4. 15a}$$

$$\frac{2}{3}T_{\perp} + \frac{1}{3}T_{\parallel} = T_{eq} = const \tag{4.15 b}$$

Here, $T_{\parallel}$ and $T_{\perp}$ are longitudinal and transverse temperature respectively. T_{eq} is the final equilibrium temperature. τ is the relaxation time. With the initial conditions $T_{\parallel 0}=0$ and $T_{\perp 0}=3/2\ T_{eq,}$ we can solve these two equations and the solutions are

$$T_{\perp} = \frac{2}{3}T_{\perp 0}(1 + \frac{1}{2}e^{-3t/t_{eff}}), \tag{4. 16a}$$

and

$$T_{\parallel} = \frac{2}{3}T_{\perp 0}(1 - e^{-3t/t_{eff}}), \tag{4.16b}$$

where τ_{eff} is the effective temperature relaxation time and is given by

$$t_{eff} = 4.44\times10^{20}\frac{(k_B T_{eff}/mc^2)^{3/2}}{n\ln\Lambda}. \qquad (4.17)$$

Here, T_{eff} is related to $T_{\perp 0}$ by

$$k_B T_{eff} = 0.373 k_B T_{\perp 0}. \qquad (4.18)$$

$\ln\Lambda$ is the Coulomb logarithm and it is obtained from

$$\ln\Lambda = \ln\left[5.66\times10^{21}\frac{(k_B T/mc^2)^{3/2}}{n^{1/2}}\right]. \qquad (4.19)$$

In the formula, n is the particle density and is given by

$$n = \frac{I}{ea^2 pv}, \qquad (4.20)$$

where I is the beam current, a is the beam radius and v is the beam velocity.

From Equation (4.16), we find that the final longitudinal and transverse temperature will reach the equilibrium of two thirds of the initial transverse temperature. The time it takes to reach equilibrium is about τ_{eff}. Figure 4.21 shows how they reach equilibrium with time. In the figure, longitudinal and transverse temperatures are normalized to the final temperature and the time is normalized to the effective relaxation time.

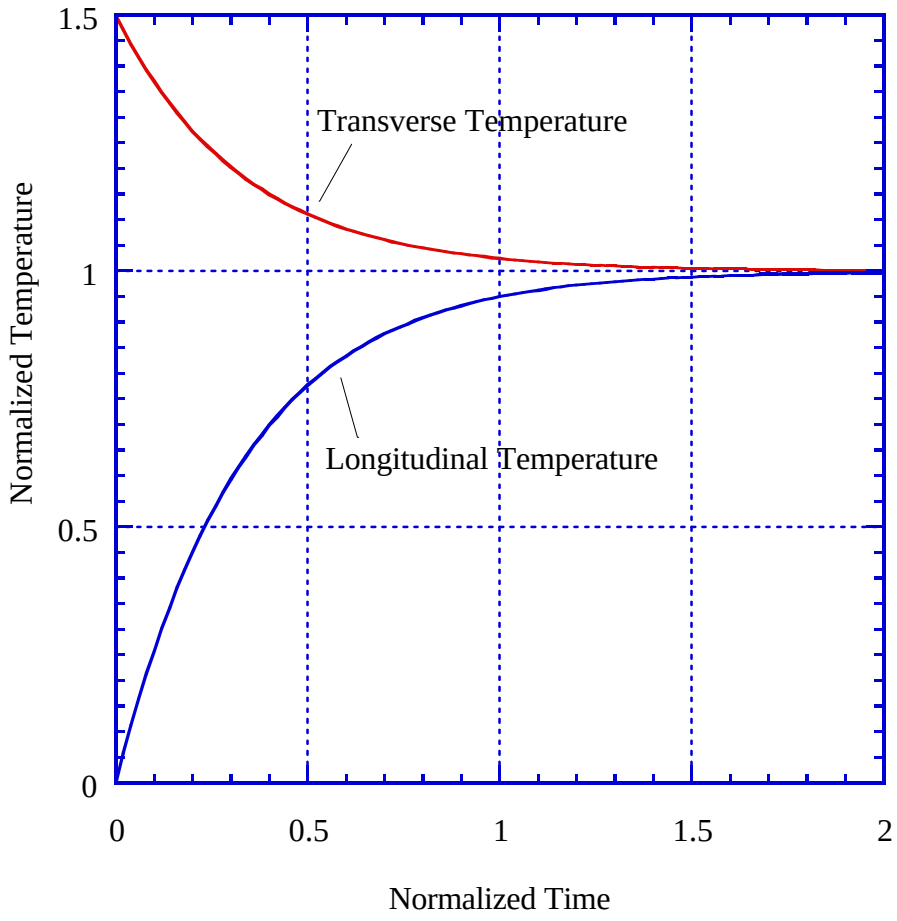

Figure 4. 21. Relaxation of the transverse and longitudinal temperature due to Boersch effect. The time is normalized to t_{eff} and the temperature is normalized to $\frac{2}{3}T_{\perp}$.

4.5.2 The Longitudinal-Longitudinal Relaxation Effect

The energy transfer from transverse direction to longitudinal direction due to the Boersch effect can be suppressed by applying a strong magnetic field. However, even if this energy transfer is suppressed, the final beam energy spread is found to be still larger than what is predicted by transverse-longitudinal cooling effect. The reason is that the coulomb collisions in addition to the Boersch effect, cause another temperature relaxation called longitudinal-longitudinal relaxation. If the acceleration is fast (non-adiabatic) compared to the period of the electron beam plasma oscillation period, the initial state of relative high density and slow motion of electrons relative to each other is preserved during the acceleration process. Coulomb collisions relax this non-equilibrium state into a more homogenous state and result in energy spread increase. Taking into account this longitudinal-longitudinal effect, the final beam energy spread is [1, 10]

$$\Delta\tilde{E}_{\parallel f} = \left[\frac{C}{pe_0} qn^{1/3} qV_0 + 2qV_0 k_B T_{\parallel}\right]^{1/2}, \qquad (4.\ 21)$$

Here $\Delta\tilde{E}_{\parallel f}$ is the rms energy spread after acceleration and beam propagation; qV_0 is the beam energy and $T_{\parallel}$ is an increasing function of time or distance of beam propagation, which can be calculated from Equation (4.16) (Boersch Effect). All the beam energies are in units of eV; n is the beam density, q is the electron charge and C is a constant of the order of unity. The first term in the bracket corresponds to the longitudinal-longitudinal effect during acceleration, and the second term is

the transverse-longitudinal (Boersch) effect. The second term takes much longer time than the first term until equilibrium between longitudinal temperature $T_{\parallel}$ and transverse temperature $T_{\perp}$ is reached. The Boersch effect (second term in Eq. (4.21)) quickly dominates over the longitudinal-longitudinal relaxation effect.

To look at the time scale of the longitudinal-longitudinal effect, we first have to calculate the plasma frequency of the beam. In the electron beam, the plasma frequency can be expressed as

$$w_p = \sqrt{\frac{q^2 n}{e_0 m}} . \qquad (4.22)$$

Here n is the particle density, m is the electron mass, q is the electron charge and ε_0 is the dielectric constant. In our experiment, ω_p is typically about 7.8×10^8 s^{-1} and one plasma period is

$$t = 2p / w_p , \qquad (4.23)$$

which is around 8 ns, a very short time. While for a similar beam, the effective relaxation time constant of the Boersch effect is in the range of microseconds.

As was pointed out before, the longitudinal-longitudinal effect occurs when the beam acceleration is fast (non-adiabatic) and it can be reduced by adiabatic acceleration. The criteria for the adiabaticity condition is determined by a non-

dimensional parameter λ, which compares the cooling time $\left(-\frac{1}{T_{\|}}\frac{dT_{\|}}{dt}\right)^{-1}$ with the plasma period ω_p^{-1}:

$$l = -\frac{1}{w_p T_{\|}}\frac{dT_{\|}}{dt}. \qquad (4.24)$$

If λ<1, then the acceleration is adiabatic. λ depends on the acceleration structure. It is interesting to note that a thermal electron gun with Pierce geometry has l equal to $2^{3/2}$ [10], a nonadiabatic case, which applies to our experiment.

4.5.3 Comparison of the Experimental Results with the Energy Spread Predicted by the above two Sources.

We can use the above theory to estimate the energy spread due to the Boersch effect and the longitudinal-longitudinal effect. In our example, the beam energy ranges from 2.5 keV to 5.5 keV. The beam is emitted from a cathode with radius of 5 mm. In the transport system, the average beam radius is around 9 mm. By applying Equations (4.16)~(4.17) to a 2.5 keV beam with beam current of 60 mA, we calculate that the rms energy spread due to the Boersch effect is ~1.0 eV. The first term of Equation (4.21) gives the energy spread due to the longitudinal-longitudinal effect, which is 0.9 eV in this case. The final energy spread resulting from both effects as given by Equation (4.21), is ~1.3 eV. The experimental measurement of the energy spread for this 2.5 keV beam is 1.8 eV, relatively close

to, but larger than, the theoretical prediction. The measurements are also performed at different beam energies. Table 4.2 shows the comparison of the results from these two effects and the results from experiments. The table shows that at this distance, the energy spreads due to the two sources are comparable. From the comparison, we find that the experimental results are always larger than the theoretical predictions, and the discrepancy increases with beam energy. The discrepancy becomes larger at higher beam energy. There are several possible reasons for this discrepancy. First, as we explained earlier, the resolution of the energy analyzer decreases almost linearly with increasing energy. Secondly, besides these two dominant energy spread sources, there are other sources which may cause an increase of the beam energy spread. For example, some simulations show that a beam with a two-temperature anisotropy ($T_{\|i} << T_{\perp i}$) will develop an instability which will increase the longitudinal energy spread and even significantly deteriorate the beam quality [41,42].

Table 4. 2. Comparison of the rms energy spread from sources of Boersch effect, longitudinal-longitudinal effect and experiment at different beam energies.

Beam Energy (keV)	Boersch Effect (eV)	L-L Effect (eV)	Combination of Both Effects (eV)	Experimental Results (eV)
2.5	1.0	0.9	1.3	1.8
3	1.1	1.0	1.5	3.2
3.5	1.2	1.1	1.6	3.6
4	1.3	1.2	1.8	4.2
4.5	1.4	1.3	1.9	5.1
5.5	1.6	1.4	2.1	5.9

4.6 A Computer-Controlled System for Energy Spread Measurements

Measuring beam energy spread is very tedious and time consuming because it needs a lot data taking and processing. In the previous experiment, we could not afford taking a lot data points because, to save the cathode lifetime, we can only keep the beam running for a short time. After we are familiar with running experiment, it becomes natural and necessary to run the experiment automatically. A computer-controlled system is designed for this purpose. The system diagram is shown in Figure 4.22. The software platform is LabVIEW^{TM} 5.0. A high voltage is supplied by an analog high-voltage power supply; the analog power supply can be controlled by a computer through Bertan 205B GPIB interface. Bertan 205B takes the GPIB command from the computer and converts it into analogue signal to control the high voltage power supply. The analog signal is 0~10 V for the full range control.

The Tektronix 602A Digital Signal Analyzer (DSA) takes the data from the energy analyzer and saves the data to disk for later processing. The DSA has a GPIB interface so it is easy to communicate with the computer. In the experiment, the user set high voltage scanning range and the DSA channel number on the software front panel. The data file name and whether or not you want to save the data can also be set in the beginning. User also has to set the time window for which she wants to measure the energy profile. After clicking RUN button, the

program will start to set the high voltage, take the energy analyzer data and set new high voltage and take data again. The process keeps going until full high voltage range has been scanned. After the data are taken, the software will plot out the energy profile and its differentiation for the beam energy distribution. Figure 4.23 shows the front panel of the demo program.

The automated system works much faster than doing it manually. The measurement speed of this system is mainly limited by saving signal trace to the disk. So user has an option to choose fast mode or slow mode. In the fast mode, the data is only taken in the memory, but not saved to the disk. In the slow mode, all the traces are stored in the disk. Approximately 50 data points can be taken in four minutes when the system runs in the fast mode, while 20 data points can be taken in four minutes in the slow mode.

The system still needs improvement. In the experiment, we found that the real high voltage output is always a couple of volts off from the setting value. We guess this is due to the analog control of the high voltage power supply. Because in the analog control, we use 0~10 V control signal to control 0~10 kV high voltage. If there is any voltage drop due to the connection resistance, the output voltage will be smaller than the setting voltage. One way to correct this problem is to make good contact of each connector. However, this has limited effect. A better solution is to use a digital interface directly in the high voltage power supply and use TTL signal to control the power supply.

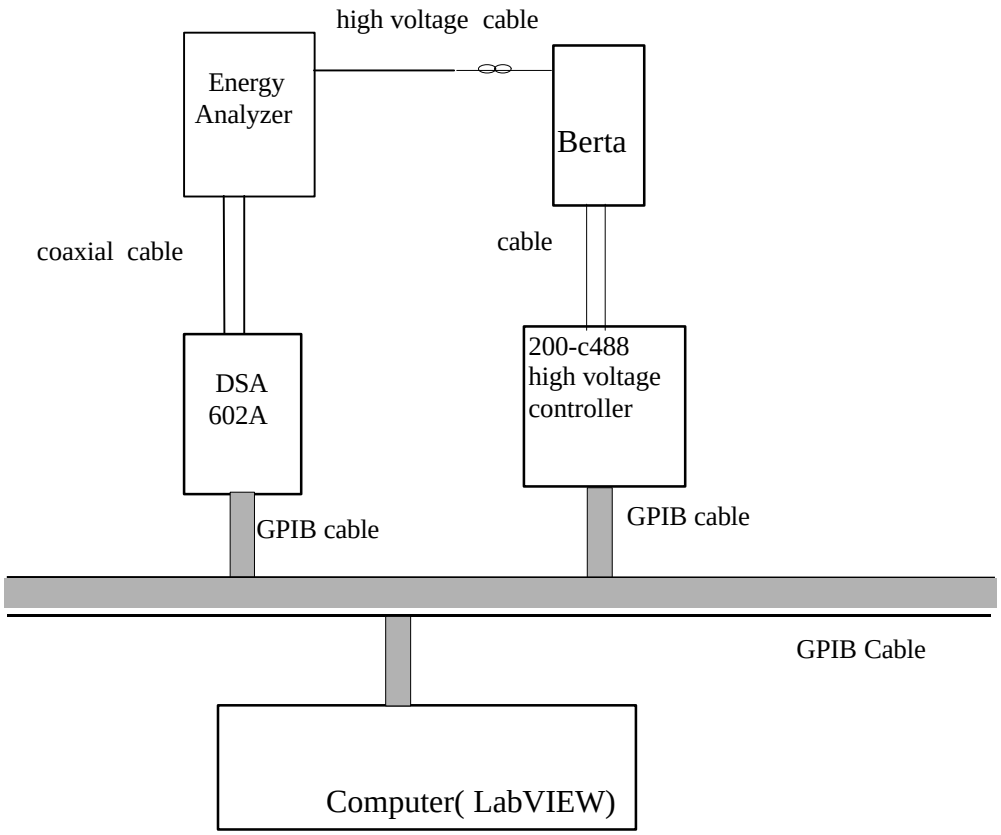

Figure 4. 22. Computer-controlled system for retarding voltage energy analyzer.

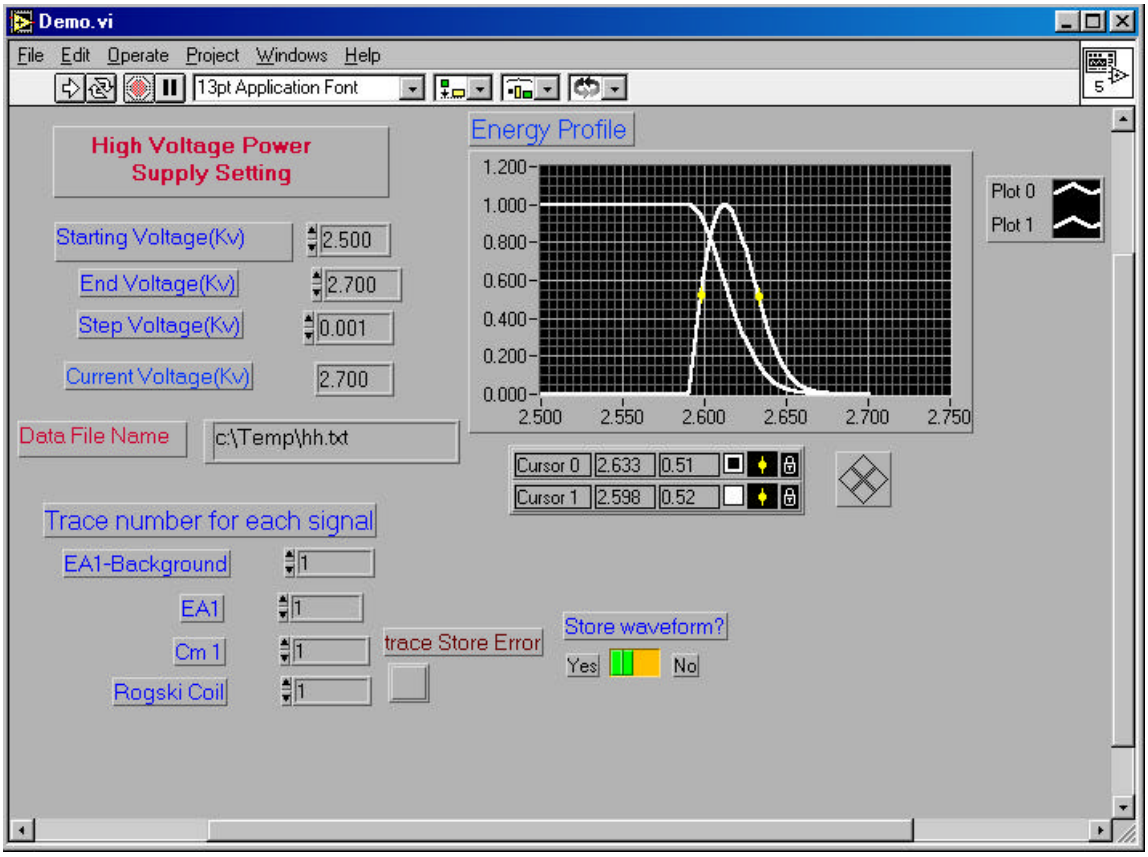

Figure 4. 23. The program front panel for the computer-controlled energy spread measurement system. The curve in the panel is a demonstration, not from the real experiment.

4.7 Conclusion and Future Work

Work has been performed to study the principle of retarding voltage energy analyzer. It was found that due to the imperfection of the energy analyzer, the response of the energy analyzer is not always the same as in the ideal case. The objective of designing an energy analyzer is to get as close as possible the ideal response to a real beam.

Performances of different retarding voltage energy analyzer were studied and compared. Study showed that the parallel energy analyzer developed previously is only good for measuring the highest energy of the beam but not good enough to measure the beam energy spread. The transverse beam trajectories will affect the energy analyzer results and result in apparently larger energy spread. A new energy analyzer with cylindrical structure was designed to improve the resolution of energy spread measurement. Computer simulation showed that it has much better resolution than the parallel energy analyzer.

Beam test was performed on the cylindrical energy analyzer. The new experiment has achieved much smaller energy spread than the previous experiments, showing that the results are much closer to the real beam energy spread. Measurements were also performed at different beam energy to study the energy width dependence on the beam energy.

Simples models were applied to estimate the energy spread in the electron beam due to the Boersch effect and longitudinal-longitudinal effect. The experimental results and the theory estimation agreed reasonably well.

The computer simulation and beam test showed that this energy analyzer is good enough to be used for UMER and future study of the energy spread in the space-charge-dominated beam. This includes the electron gun characterization, resistive-wall instability in UMER and more systematic measurement of the beam energy spread at different distance from the electron gun and with different beam parameters etc. In the experiment, we also found that the new energy analyzer is very reliable and very robust with respect to the mechanical misalignment.

A computer-controlled system is being built to run experiment more efficiently.

Chapter 5

Development of a Capacitive Beam Position Monitor (BPM) and a Fast Rise-Time Dipole for the University of Maryland Electron Ring (UMER)

5.1 The University of Maryland Electron Ring (UMER)

To study the physics of space-charge dominated beams, a small electron ring has been designed and being built at the University of Maryland [5, 30, 36]. It is directly motivated by the research in the heavy ion inertial fusion (HIF), which requires extremely high-density and short-pulse beam. As a cost-saving alternative, beam physics of the intense heavy ion beam could be studied on a low-energy electron ring. Compared to the linear accelerator, the electron ring can be small enough to fit into a regular laboratory while still can provide much longer beam path to study the dynamics of space-charge dominated beam.

The schematic of the UMER is shown in Figure 5.1. A 10 keV, 100mA, 70-100 ns electron beam with a normalized effective emittance of 10 mm-mrad from an electron gun is injected into the ring with the aid of a pulsed, Panofsky-type

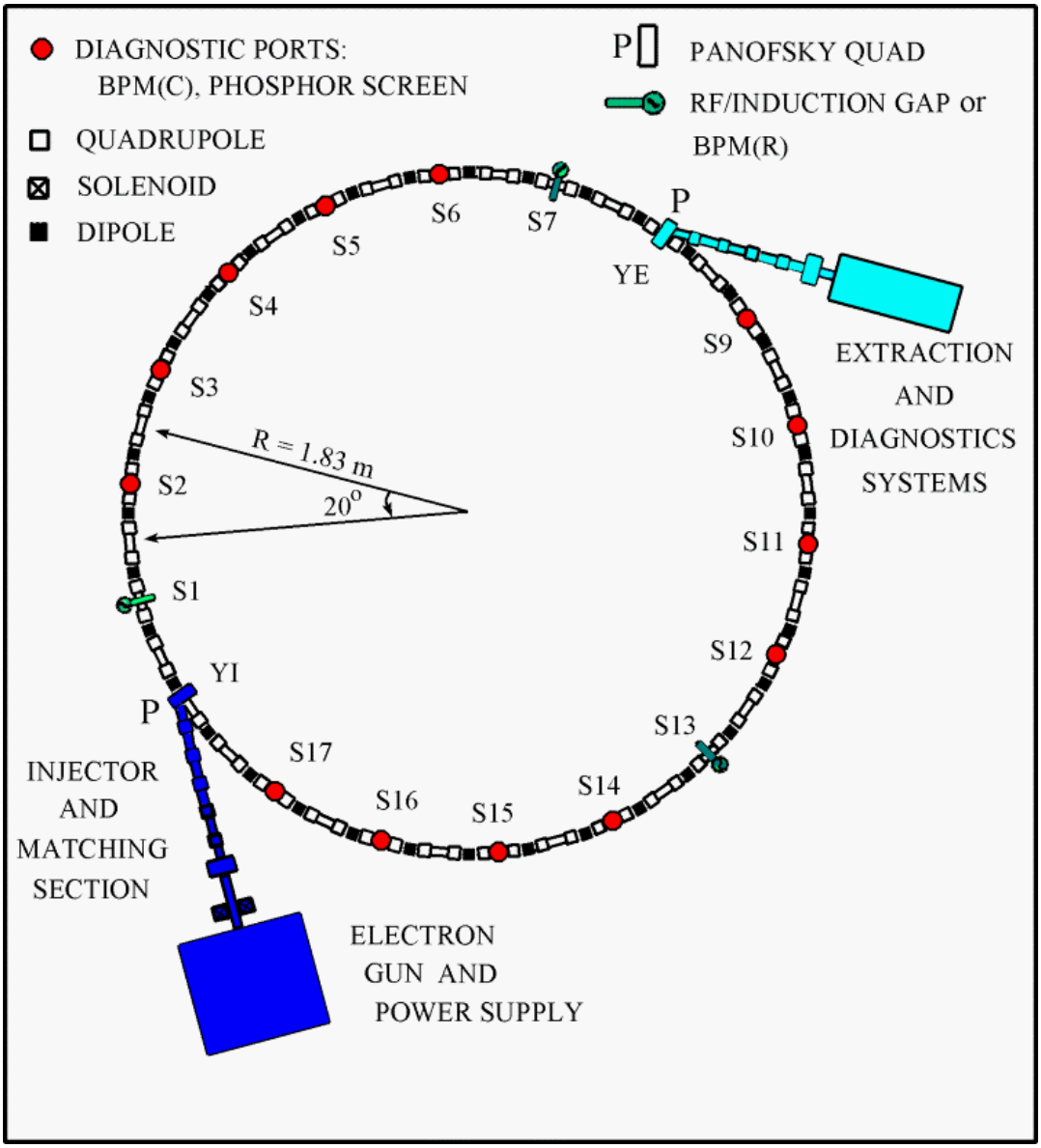

Figure 5. 1. UMER layout.

quadrupole, and a fast deflecting dipole. Transverse focusing is provided by 72 printed-circuit (PC) quadrupoles while steering is provided by 36 PC dipoles. Three induction gaps are employed for longitudinal focusing of both parabolic and rectangular bunches. The diagnostics on the ring include 13 capacitive BPMs, 3

Table 5. 1 Main design parameters of UMER.

Injection energy	10 keV
Injection current	100 mA
Generalized perveance	0.0015
Initial emittance (normalized)	10 mm-mrad
Mean beam radius	1.04 cm
Vacuum Tube bore diameter	4.90 cm
Lap time	197 ns
Lattice periods	36
Half-lattice length	16 cm
Quadrupole effective length	3.86 cm
Quadrupole diameter	5.3 cm
Gradient	7.7 G/cm
Tune (zero current)	7.6
Phase advance w/o space charge	76^{o}
Phase advance w/ space charge	9^{o}- 25^{o}

resistive-wall current monitors and 13 phosphor screens. A pulsed extraction system similar to the injector is included for beam analysis. The extraction chamber houses an emittance meter, an energy analyzer and a phosphor screen viewer. The ring's main parameters are summarized in Table 5.1.

5.2 Development of a Capacitive Beam Position Monitor (BPM)

5.2.1 Motivation

BPMs, including capacitive BPMs and resistive BPMs, are widely used in charged particle accelerators and beam lines [37-39]. In the UMER, because the beam has relatively low energy (10 keV), it is almost impossible to have the beam perfectly centered in the pipe. Every imperfection, like stray magnetic fields (the earth's field and other stray fields due to the presence of metal) and misalignments of the quadupoles and dipoles, will let the beam go off-centered. To guarantee the success of the UMER, beam centroid motion has to be measured very accurately and the information from the BPMs must be provided to a beam steering system to steer the beam back. Both resistive wall BPMs and capacitive BPMs will be used in the UMER. The detailed theory and design of a capacitive BPM are discussed below.

5.2.2 Basic Principle

The common method of monitoring the position of a charged-particle beam is to couple the electromagnetic field of the beam. When an electron beam travels inside a beam pipe, there are electromagnetic fields accompanying it. For a highly relativistic beam, the fields are pure transverse electric and magnetic fields. In our case, the beam energy is 10 keV and it is non-relativistic. However, the beam is so long that the fields accompanying the beam body are still transverse fields, which means that one-dimensional model is still a good approximation for this problem.

There are two types of most commonly used, non-interceptive BPMs in the accelerator field. One is called resistive-wall BPM, which is a gap in the beam pipe with a ceramic sealing to maintain vacuum. A bunch of uniformly distributed resistors are connected across the gap to carry the wall currents. The azimuthal distribution of wall currents, determined by the voltage across different resistors, can be used to measure the beam position. Another way to detect the electromagnetic field of a beam is to put a pair of electrodes inside the beam pipe. When the beam passes an electrode, signals are induced on it. Based on the different signals from two opposite electrodes, we are able to determine the beam position. Because this is a capacitive pick up, it is referred as capacitive BPM in the linterature. In this section, we will focus on the design of a capacitive BPM.

There are various kinds of electrodes for capacitive BPM. Button electrode, which is short and the capacitance is very small, is suitable for detecting very weak

beam current. On the other hand, capacitive electrode, which is relatively long and has larger capacitance, can reproduce the beam pulse waveform faithfully. We use the second structure because it is very important for us to see the beam profile while measuring the beam position. This becomes essential when we study the propagation of space charge waves in the beam.

Figure 5.2(a) is a sketch of the cross section of a capacitive BPM. There are four pickup electrodes uniformly located inside the beam pipe. If the beam is centered, the induced voltage on each electrode are the same. First, let us study the response of an arbitrary electrode to a centered beam.

Assume the beam current is $I_b(t)$, and the electrode is short enough that the current inside can be treated as independent of the z position, the induced charge on one of the electrode can be written as

$$Q(t) = \frac{a}{2p}\int_0^L I_b(t,z)dz/v_0 \cong \frac{aL}{2pv_0} I_b(t). \qquad (5.1)$$

Here, L is the electrode length, α is the angle of the electrode, $I_b(t)$ is the beam current and v_0 is the beam velocity. If the capacitance between the electrode and beam pipe is C, then the voltage on the electrode due to the induced charge is given by

$$V = \frac{Q}{C} = \frac{aL}{2pv_0 C} I_b, \qquad (5.2)$$

where C is given by

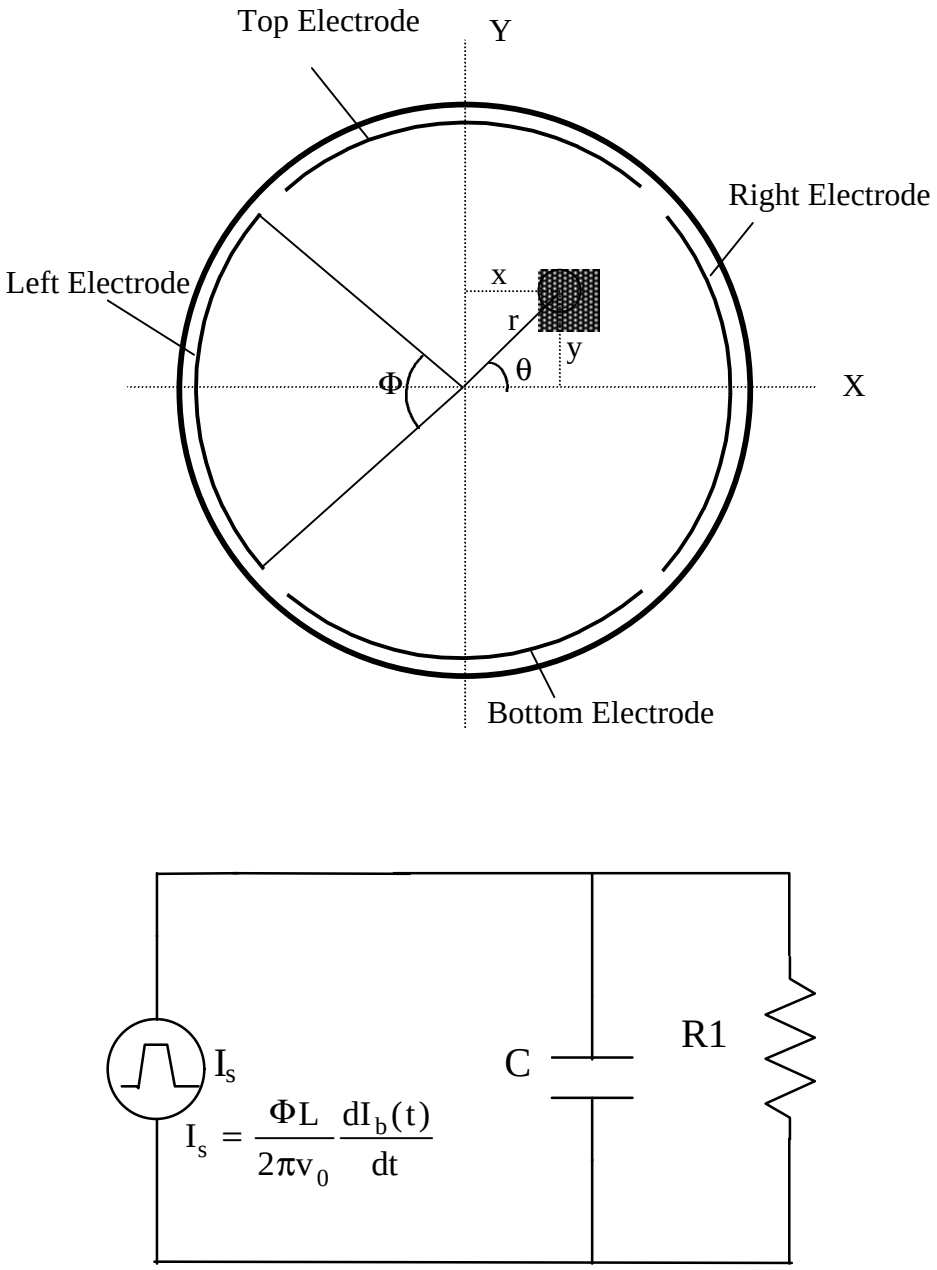

Figure 5. 2. (a) BPM pick up electrodes. (b) BPM equivalent circuit.

$$C = \frac{\alpha \varepsilon L}{\ln(\frac{b}{a})}. \qquad (5.3)$$

Here a is the radius of the electrode, b is the radius of the beam pipe and ε is the dielectric constant of the insulating material between the electrode and beam pipe.

The above derivation is based on the assumption that the induced charge can be kept on the electrode and they are not discharged. In a real BPM, to avoid excess charge accumulation on the electrodes, there is a bleeder resistor between the electrode and the beam pipe. So the charge on the electrode is always discharged through the bleeder resister. The effects of this process on the signal output depend on the RC time constant and beam bunch length. If the RC time constant is much larger than the beam bunch length, the above derivation is still a good approximation. On the other hand, if the RC time constant is smaller than the beam bunch, the voltage on the electrode will have a droop. For the extreme case, i.e., the RC time constant is much smaller than the beam bunch length, the signal output is the derivative of the beam signal.

The equivalent circuit shown in Figure 5.2 (b) can explain this effect. In the figure, C is the capacitance between the electrode and beam pipe, R_1 is the bleeder resistor between the electrode and the pipe and I_s is a frequency dependent current source. From Equation (5.1), the formula to calculate I_s is

$$I_s = \frac{dQ}{dt} = \frac{aL}{2pv_0}\frac{dI_b(t)}{dt}. \qquad (5.3a)$$

The output signal is picked up from a resistor, which is in parallel with the capacitor. If the impedance of the resistor is much larger than the impedance of the capacitor, the circuit is an integrator. The integration of $I_s(t)$ is $I_b(t)$, the beam current itself. This is the large R_1C constant case. On the other hand, if the impedance of the resistor is much smaller than that of the capacitor the output is approximately I_sR_1. In this case, the output is the derivative of the beam signal.

We used PSPICE to simulate the performance of this circuit. In the simulation, we assume that the beam bunch profile is a rectangular bunch. To avoid any singularity we intentionally let the rectangular bunch have a rise time of several nanoseconds. Figure 5.3 is the case of $R_1C=10T_0$, with T_0 being the beam bunch length. The BPM can reproduce the beam signal pretty well. Notice that even in this case, the response has a small droop. Also notice that, at the end of the signal, there is undershoot. Theoretically, the area of undershoot should be equal to the difference between the areas of the beam current and BPM response. Figure 5.4 depicts a case for $R_1C<<T_0$ where the BPM output is close to the derivative of the beam signal. In the design, we try to avoid this case by applying large enough RC time constant.

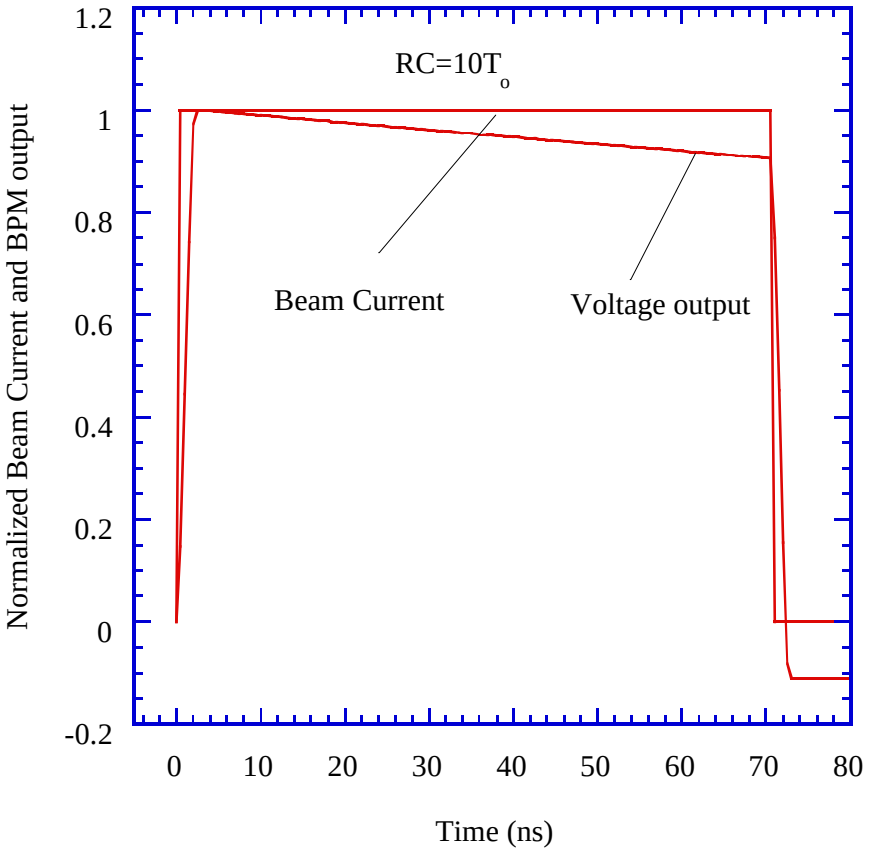

Figure 5. 3. BPM response to a current pulse with RC=10 T_0.

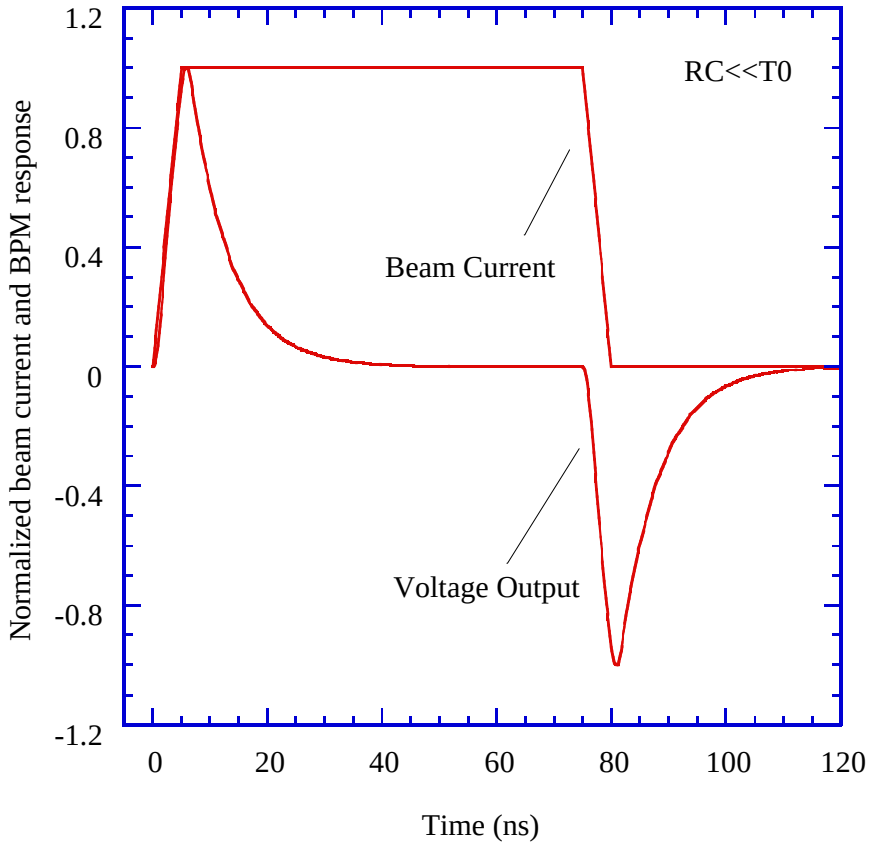

Figure 5. 4. BPM response to a beam current with $RC<<T_0$.

If the beam is displaced from the axis, the voltages from four electrodes will be different. Assuming a pencil beam at position r and θ inside a circular pipe, as shown in Figure 5.2(a), the wall current density at b, Φ_w is given by

$$i_w(b, \Phi_w, t) = \frac{-I_b(t)}{2\pi b}[1 + 2\sum_{n=1}^{\infty}(r/b)^n \mathrm{Cos}[n(\Phi_w - \theta)]] \ . \quad (5.4)$$

Because of this asymmetric wall current distribution, the voltages on the two opposite electrodes are different. Integrating the wall current density over the electrode, we can find the total charge and, therefore, the voltages on two opposite electrodes. Equations (5.5) and (5.6) give the voltage on two opposite electrodes respectively. They are

$$V_R(t) = \frac{I_b(t)\ln(b/a)}{2pev}[1 + \frac{4}{\Phi}\sum_{n=1}^{\infty}\frac{1}{n}(r/b)^n Cos(nq)Sin(\frac{n\Phi}{2})] \quad (5.5)$$

and

$$V_L(t) = \frac{I_b(t)\ln(b/a)}{2pev}[1 + \frac{4}{\Phi}\sum_{n=1}^{\infty}\frac{1}{n}(r/b)^n Cos(nq)Sin[n(p + \frac{\Phi}{2})]]. \quad (5.6)$$

The ratio of two voltages in decibels determines the beam position. The ratio of V_R over V_L is (in decibels) [Appendix I]

$$20\log(V_R / V_L) = \frac{160}{\ln 10}\frac{\mathrm{Sin}(\Phi/2)}{\Phi}\frac{x}{b} + \frac{20}{\ln 10}[\frac{8}{3}\frac{\mathrm{Sin}(\frac{3\Phi}{2})}{\Phi} - 16\frac{\mathrm{Sin}(\Phi)\mathrm{Sin}(\Phi/2)}{\Phi^2}$$
$$+ \frac{128}{3}\frac{\mathrm{Sin}^3(\Phi/2)}{\Phi^3}]\frac{x^3}{b^3} + [-8\frac{\mathrm{Sin}(\frac{3\Phi}{2})}{\Phi} + 16\frac{\mathrm{Sin}(\Phi)\mathrm{Sin}(\Phi/2)}{\Phi^2}]\frac{xy^2}{b^3} + \ldots \quad (5.7)$$

If x/b is small enough, we can take the linear term. It is

$$20\log(V_R / V_L) = \frac{160}{\ln 10}\frac{\mathrm{Sin}(\Phi/2)}{\Phi}\frac{x}{b}. \quad (5.8)$$

The above formula shows that the logarithmic ratio of two voltages is proportional to the beam position. The coefficient of the linear term is called the sensitivity of the BPM, the parameter that we are most interested in. The coefficient of the second term in Equation (5.7) is the nonlinearity of the BPM. We can compensate this term by calibrating the BPM on the x or y axis. The third term, which depends on both x and y displacements, is the coupling term between x and y direction.

It is interesting to note that the coefficient of each term only depends on the electrode angular width Φ. Figure 5.5 gives the plots of these terms with respect to the angle Φ. From this figure we find that the sensitivity and the nonlinear term decrease with Φ, but both of them are greater than zero if Φ is between zero and

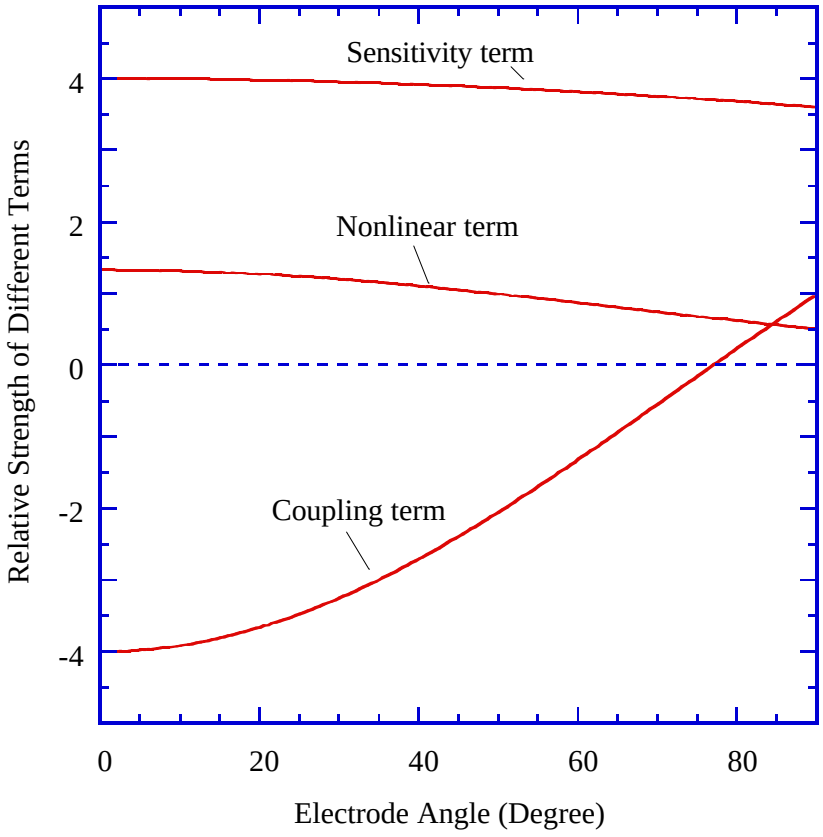

Figure 5. 5. The dependence of different terms on the electrode angle width.

90^o. The coupling term, however, could be positive or negative, depending on Φ. So it is possible to let the coupling term be zero by using an appropriate electrode width Φ. From Equation (5.7), let the third term be zero, i.e.

$$-8\frac{\mathrm{Sin}(\frac{3\Phi}{2})}{\Phi}+16\frac{\mathrm{Sin}(\Phi)\mathrm{Sin}(\Phi/2)}{\Phi^2}=0. \qquad (5.9)$$

By solving this equation, we get Φ=76.99^o. If we set the electrode width to be 76.99^o, we are able to decouple the signals from X and Y electrodes.

5.2.3 Design and Bench Test of a Prototype BPM

A prototype capacitive BPM has been designed and built to test our theory. The geometry is the same as in Figure 5.2(a). There are four electrodes inside the pipe, which are insulated from the grounded pipe by mylar, a material with dielectric constant of $2.9\varepsilon_0$. Each electrode is connected to a bleeder resistor R. For the bench test, a conducting cylindrical bar was built to simulate the beam. The bar and pipe form a co-axial structure with 50 Ω impedance. The bar can move freely inside the pipe. A pulser provides a 100 mA current pulse on the bar. The pulse is terminated by a 50 Ω load, as shown in Figure 5.6.

The signal is picked up from the bleeder resistor, which has a resistance of 3 kΩ. Because this resistor is very large, we have to use 1-MΩ impedance channel in the oscilloscope in order to avoid any interference with the source. The problem

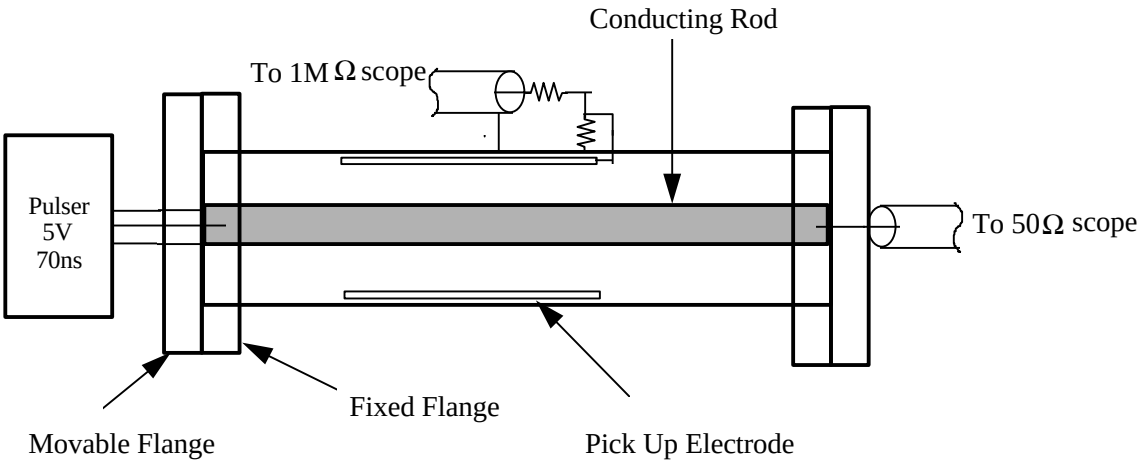

Figure 5. 6. Capacitive BPM bench test setup.

with high impedance input is that it is very easy to have oscillations. One way to solve this problem is to connect a 80-Ω resistor in series with the cable. It turns out that this resistor can suppress the signal ringing effectively. The parameters of this prototype BPM are shown in Table 5.2.

Table 5. 2. Parameters of the Prototype BPM

Pipe inner radius	23.6 mm
electrode radius	23.5 mm
electrode angle width	$\Phi=83^{o}$
Beam current	100 mA
Pulse length	70 ns
Capacitance C	0.55 nF
Bleeder resistance R	3 kΩ
RC constant	23 T_0

Figures 5.7 -5.9 are signal outputs to three different beam current signals. Figures 5.7 and 5.8 are BPM responses to a rectangular beam pulse with very fast rise time (~ 2 ns). The only difference is that one has a small perturbation while the other one does not. The ability to resolve the small perturbation is very useful to study the beam instability in the UMER. Figure 5.9 gives the BPM response to a

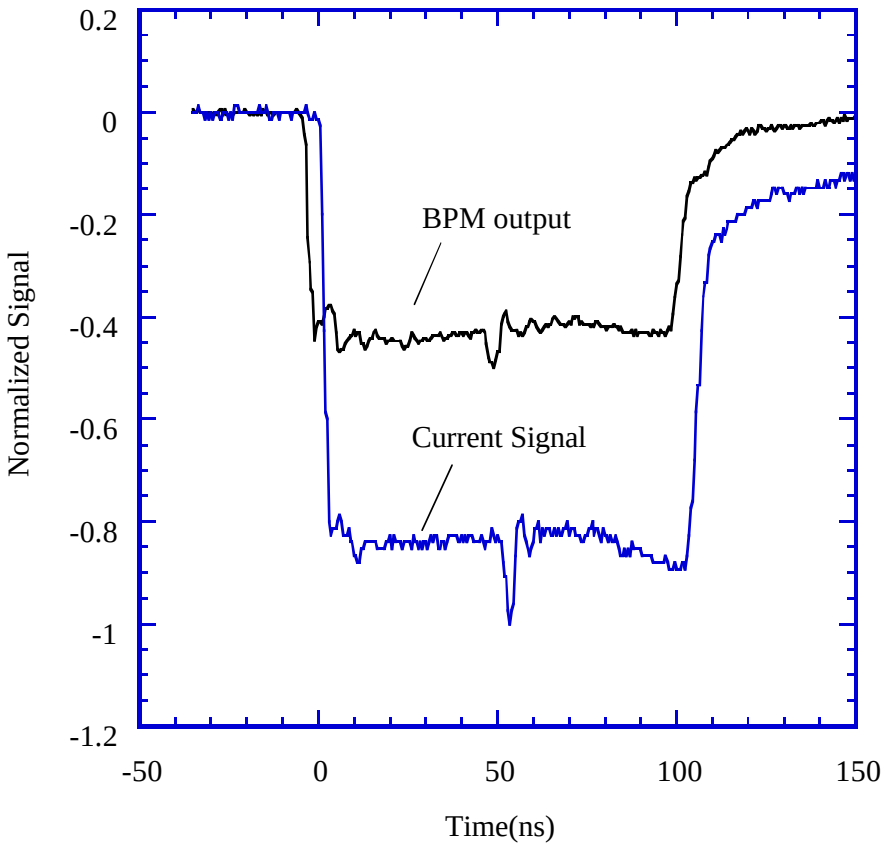

Figure 5. 7. BPM response to a rectangular pulse with a perturbation in the middle.

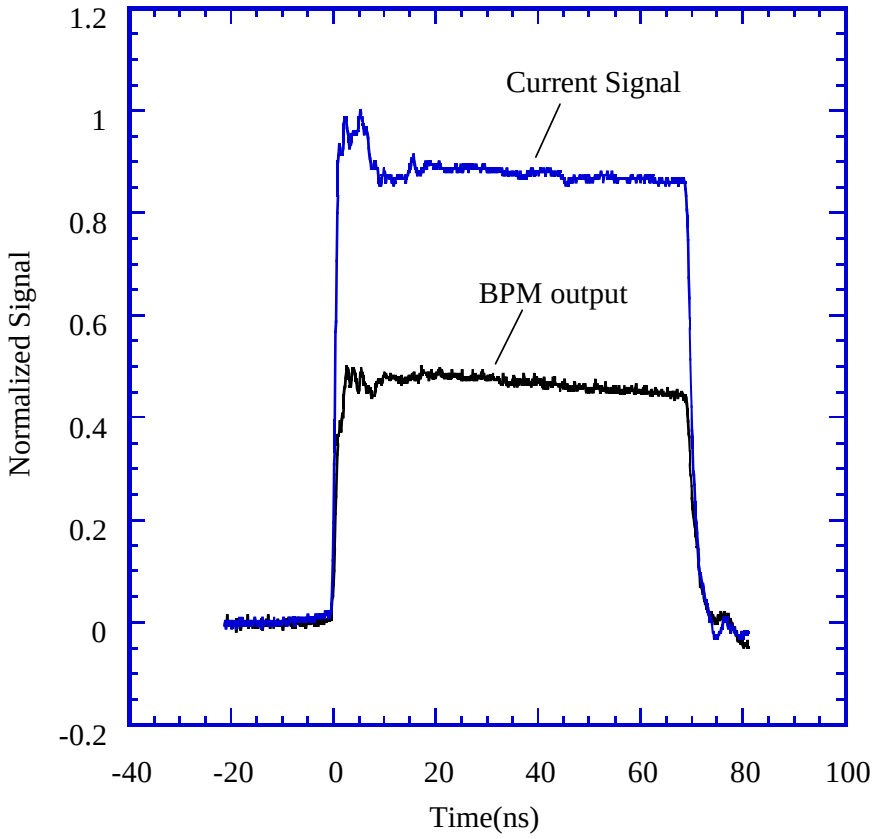

Figure 5. 8. BPM response to a rectangular pulse with fast rise-time.

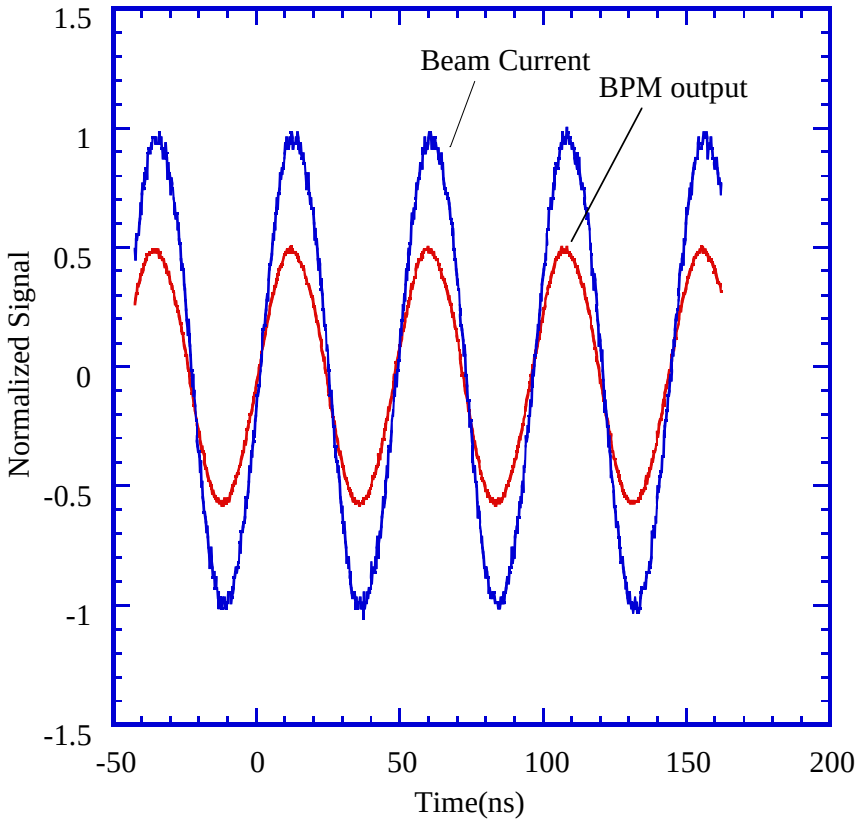

Figure 5. 9. BPM response to a sinusoidal beam signal.

sinusoidal beam current. From these experimental results, we find that the capacitive BPM has adequate signal output for a certain beam current and it is fast enough to reproduce the beam signal faithfully.

As the beam moves off-centered, the voltages from the four electrodes are different. By calculating the voltage ratio from two opposite electrodes we can find the displacement in the X and Y directions using Equation (5.8). However, in practice, four channels of the BPM are not always identical. In order to measure beam position accurately, we have to calibrate the BPM response to the beam displacement. Figures 5.10(a) and (b) are two calibration curves on both X and Y axes. By using two calibration curves, we are assuming that the voltages from the X and Y direction are not coupled. Otherwise we have to calibrate the BPM on the whole X-Y plane, which is very tedious.

To test the performance of the BPM, we have done a bench test. We set the conducting rod at different locations and measure its position mechanically. We also measure the rod positions using BPM and compare the results with the mechanical measurements. Figure 5.11 shows the comparison. We find that, within 3 mm displacement, two measurements agree with each other very well (difference smaller than 0.2mm). However, at 6mm, there is relative large difference between them (about 0.8mm). By the design parameter of the UMER, the beam displacement is with a couple of millimeters and the required accuracy from BPM is within 0.2 mm. So this accuracy has already met the requirement of the design.

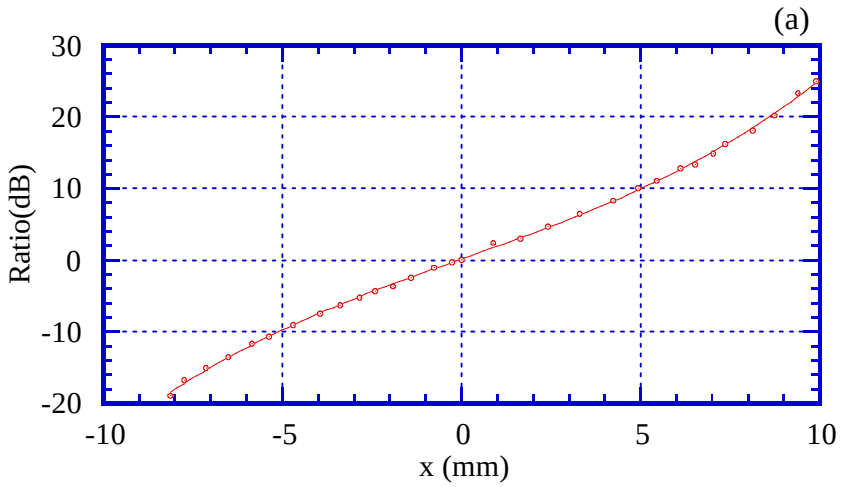

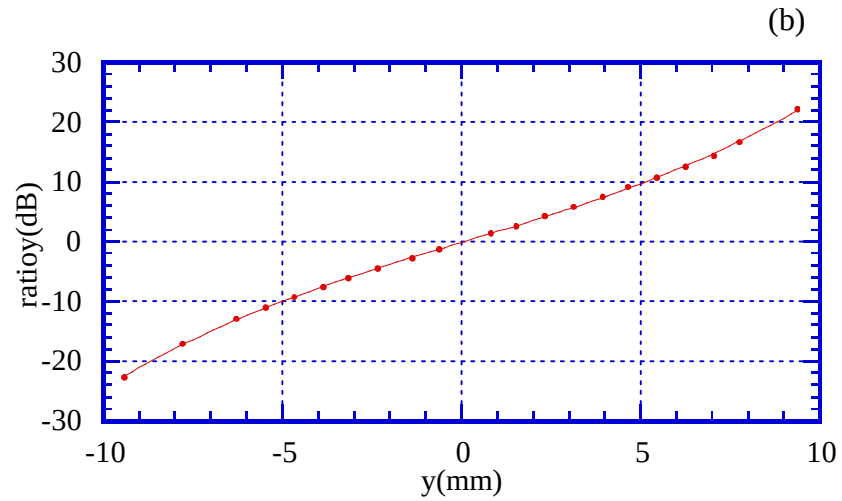

Figure 5. 10. (a) Calibration curve of BPM on X-axis (b) Calibration curve on Y-axis.

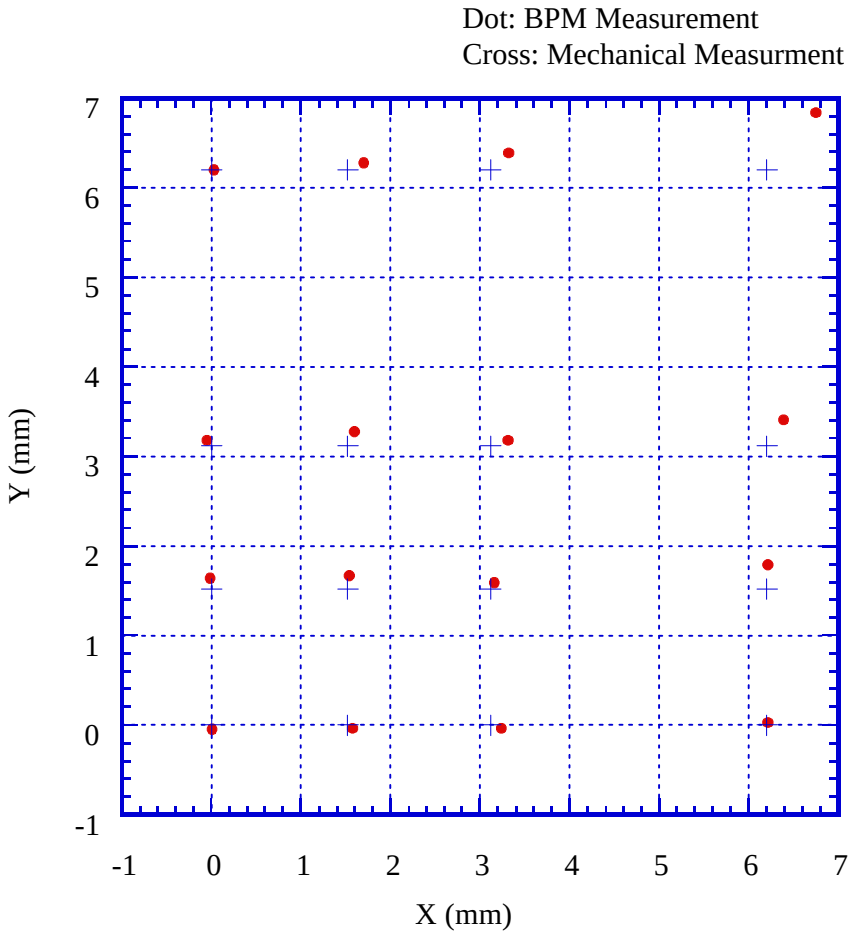

Figure 5. 11. Comparison of BPM measurements and mechanical measurements. They agree well within 3 mm displacement. Due to the coupling between X and Y electrodes, BPM gives larger results at larger beam offset.

Even though, it is interesting to study the source of the errors. Note that this discrepancy is a systematic error and it is due to the coupling between the X and Y electrodes, which is the third term in Equation (5.7). We expect this systematic error will be smaller if we optimize the electrode angle to 77^{o}.

After all, it is important to point out that, in the bench test, the signal on the rod is a TEM wave with transverse electric or magnetic field, travels at the velocity of light, which emulates highly relativistic particles. For a 10 keV beam, the particle velocity is about 0.2 of the speed of light. As was shown in the formula, the response of the BPM to a real beam will be larger than in the bench test case.

5.2.4 BPM Data Acquisition and Electronics

In the bench test, four BPM signals are hooked up to an oscilloscope directly and are digitized for processing. In the UMER, there are 18 BPMs altogether, so we have to design a data acquisition system to digitize and process the totally 64-channel signals. Basically, there are two methods to process the signal. A wide band system will contain all the frequency component of the signal; while a narrow band system will only pick up certain frequency component of the signal and process it. Each of the system has its own advantages and disadvantages. Because it keeps all the frequency components, the wide band system can record the system waveform faithfully. However, in this kind of system, the signal-to-noise ratio is relative poor and the beam position accuracy is not as good as a narrow band system. On the other hand, the narrow band system has better signal-

to-noise ratio and can measure the beam position as accurately as micrometers. The disadvantage is that it can not reproduce the beam waveform because of its narrow bandwidth.

In the UMER, the required beam position is about 0.3 mm within 3 mm displacement. We are also very interested in using the BPM to measure the beam current and beam waveform. So wide band system is used in the UMER BPM system. For the design purpose, a very important thing is to determine the bandwidth requirement of the system. The system should have enough bandwidth to keep the fine structure of the beam signal, for example, the perturbation of space-charge wave. Figure 5.12 is a typical beam current with perturbation and its Fourier transform. Figure 5.12b shows that the frequency spectrum drops to –70dB at 400 Mhz. A low pass filter with bandwidth 400 Mhz is designed to see how it will affect the beam signal. Figure 5.13 is the spectrum of an ideal low pass filter. Applying this filter to the original beam current signal, we get the signal after filtering. Figure 5.14 plots both original signal and the filtered signal. We find that there is little difference between two signals. This shows that the bandwidth of 400 Mhz is good enough for the BPM system.

Because, intrinsically, the BPM output has high impedance, we need a buffer to transform its high impedance to 50 Ω impedance, which is the impedance of the rest of the system. For this purpose, we use a preamplifier with high input impedance and unity gain. The preamplifier was developed by Electronics Group at

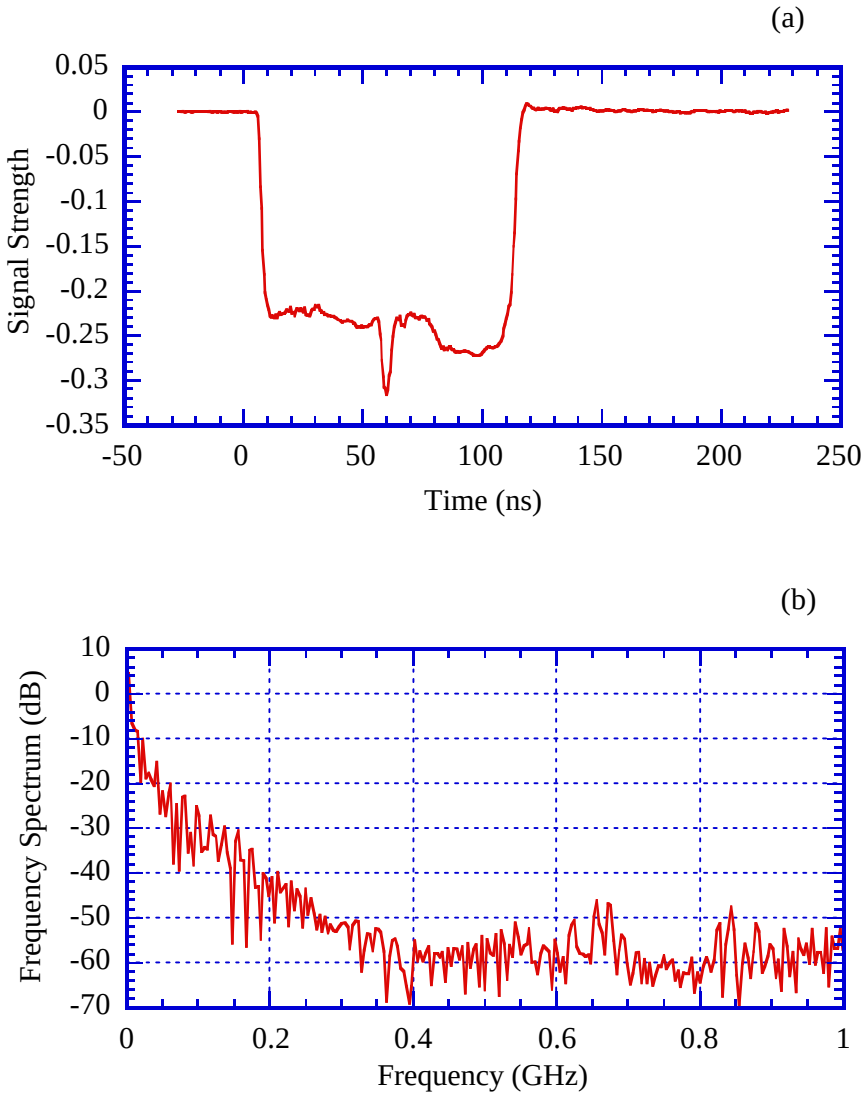

Figure 5. 12. (a)A typical beam signal in the experiment. (b) Frequency spectrum of the signal.

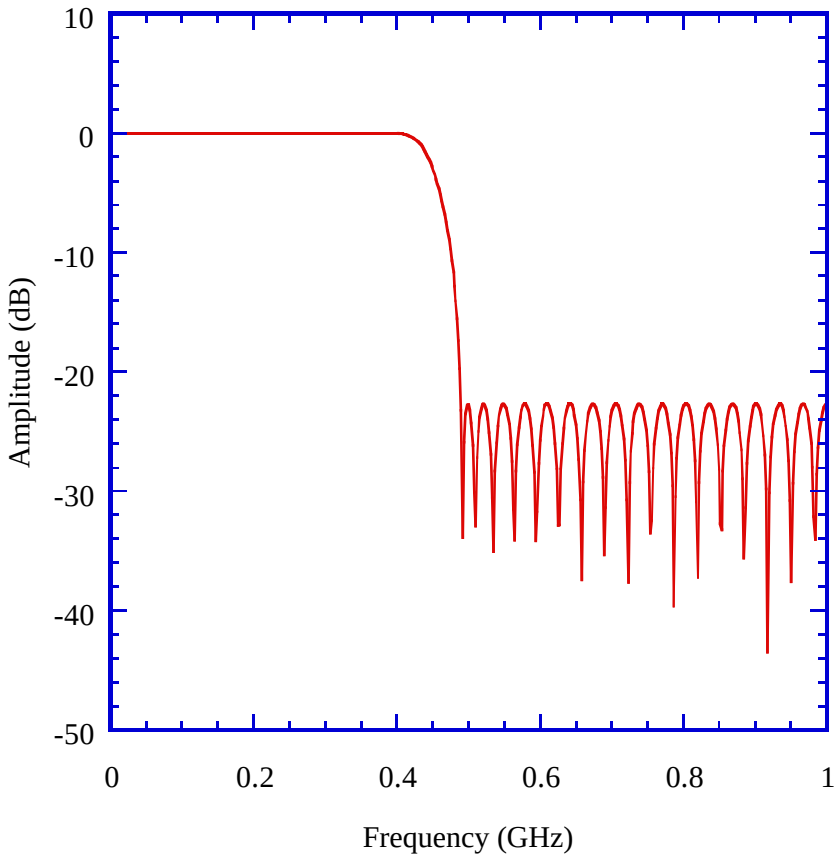

Figure 5. 13. Frequency response of an ideal low pass filter with pass bandwidth 400 MHz.

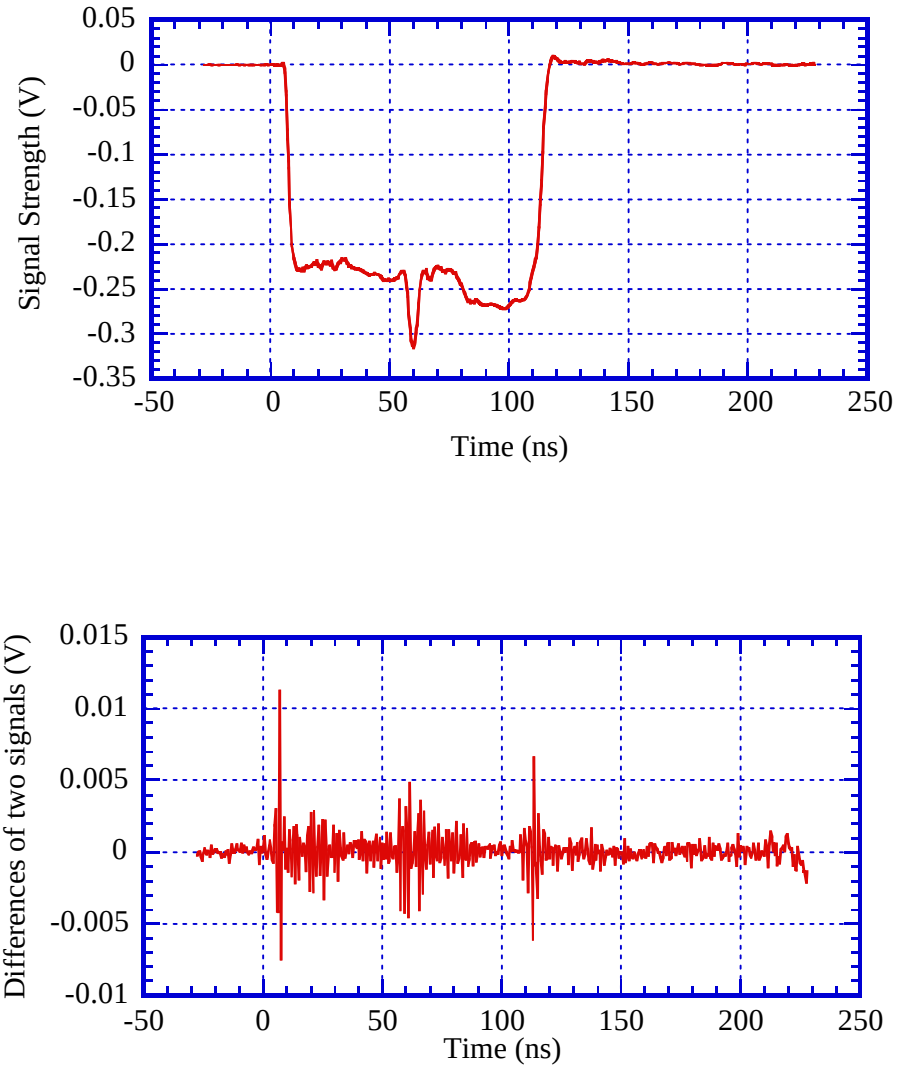

Figure 5. 14. (a) The original signal and its filtered signal. They are almost identical. (b) The difference of the original signal and filtered signal.

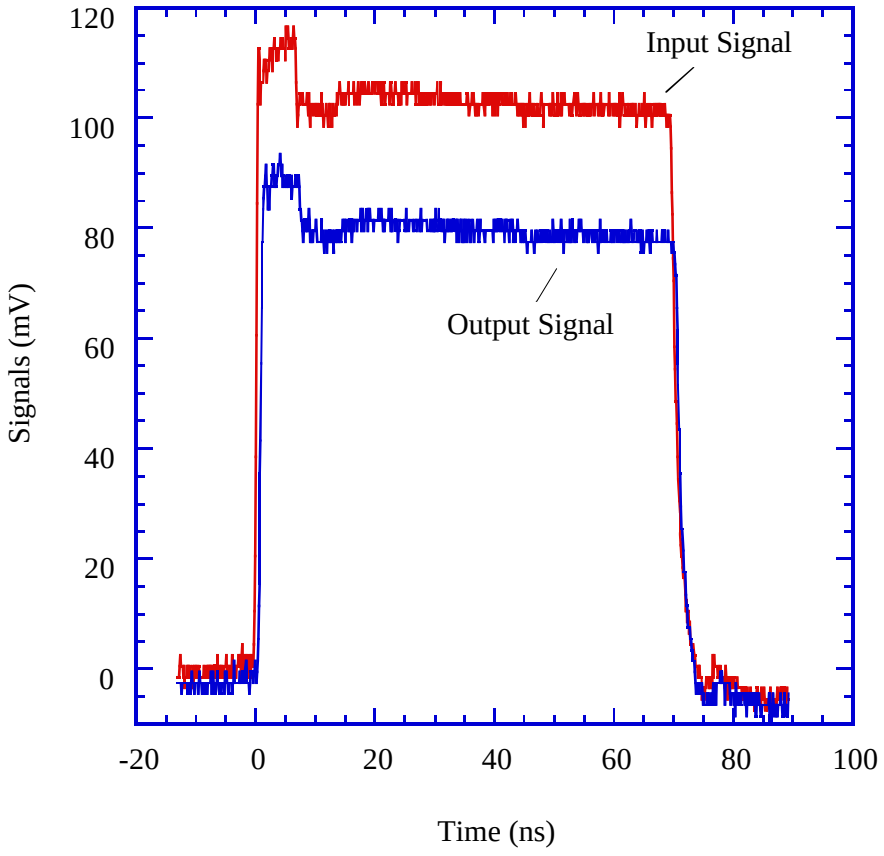

Figure 5. 15. Signals at input and output of the preamplifier. The gain of the preamplifier is about 0.8 due to impedance mismatch.

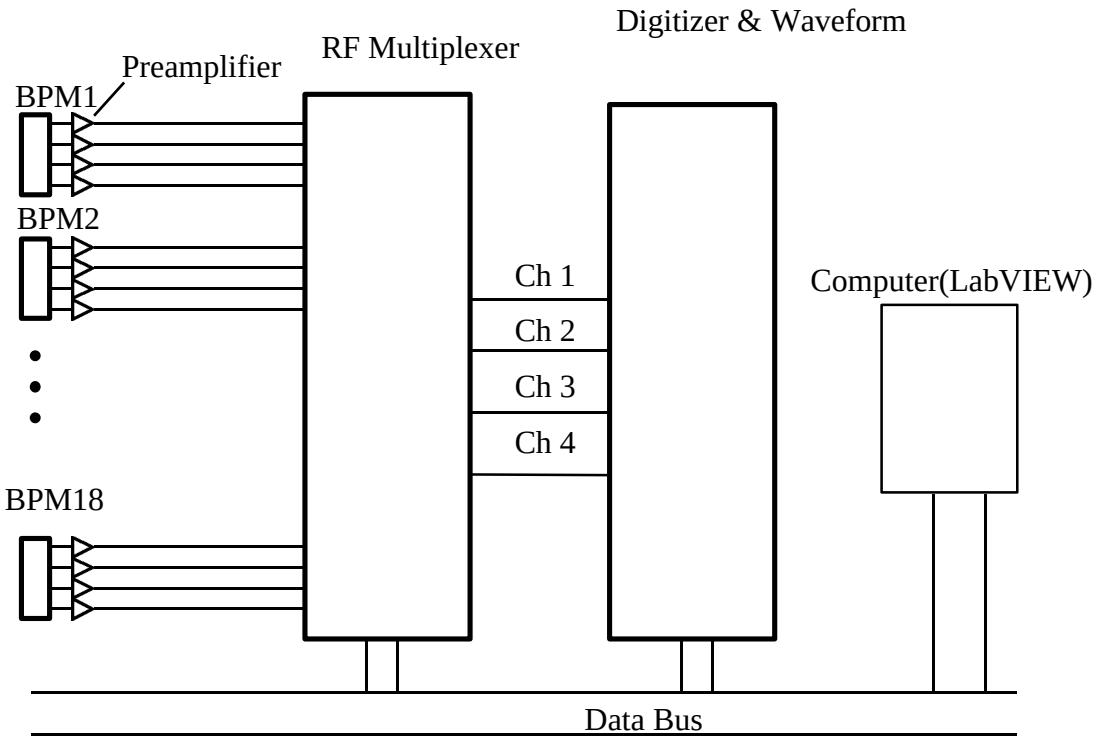

Figure 5. 16. Layout for BPM data acquisition system.

Physics department, University of Maryland. The main part of the circuit is a MAX 4005 single-ended unity-gain buffer. The input is a high impedance JFET and the output impedance is 75 Ω. By the data sheet, this buffer can also drive 50 Ω transmission line with only a slight loss in amplitude. This preamplifier is tested using a fast signal generator. Figure 5.15 plots the results. In the figure, the input signal and output signal are plotted together. We can see this preamplifier has very good bandwidth and fast rise-time. The tested gain is about 0.8.

Figure 5.16 shows the lay out for BPM data acquisition system. Right after the BPM is a preamplifier described above. There are totally 64 channels of signal, so a commercial RF multiplexer is used to multiplex the signals into a four-channel digitizer. The digitized signals are thereafter transferred to the computer for processing.

5.3 Study of a Fast Rise-time Deflecting Dipole

5.3.1 Motivation

In the UMER, the injection line has an angle of 20^{o} with respect to the main ring. Figure 5.17 shows the junction part of the injection line and the ring. When the beam is injected into the ring, it will be deflected by -10^{o}. After one turn, when the beam comes back to the injection position, it has to be deflected by $+10^{o}$, which

is the regular deflecting angle in the ring. At this junction part, we need a fast rise-time dipole, which can flip its polarity in about 100 ns. This requires that the dipole must have very small inductance so that its rise-time is within 50 ns. This imposes the main challenge to the design of this dipole. Figure 5.18 gives the time sequence of the field produced by the dipole. In the figure, we assume that the beam will run 10 turns in the ring. So the total time for the dipole to be on is about 2 μs.

5.3.2 Basic Configuration

It is well known that accurate multipole fields can be generated using conductors placed in parallel to the axis in such a way that the current distribution follows a cos(nθ) distribution, where n=1 for dipole and 2 for quadrupole, and θ is the azimuthal angle. The main dipoles in the UMER are based on this principle and were designed by FMT Inc.[40]. In the study of this fast dipole, we adopted the same method using printed-circuit wires to produce the desired field. In order to obtain small inductance, we use a combination of parallel and series structure. The whole region is divided into four quadrants. In each quadrant, the conductors are connected in parallel and the four quadrants are connected in series.

In the real design, each conductor carries equal current, and we have to locate the position of the conductor sinusoidally to achieve the dipole field. Suppose we use total number of n_t conductors in one quadrant. First, we divide the

Figure 5. 17. Injection line of UMER.

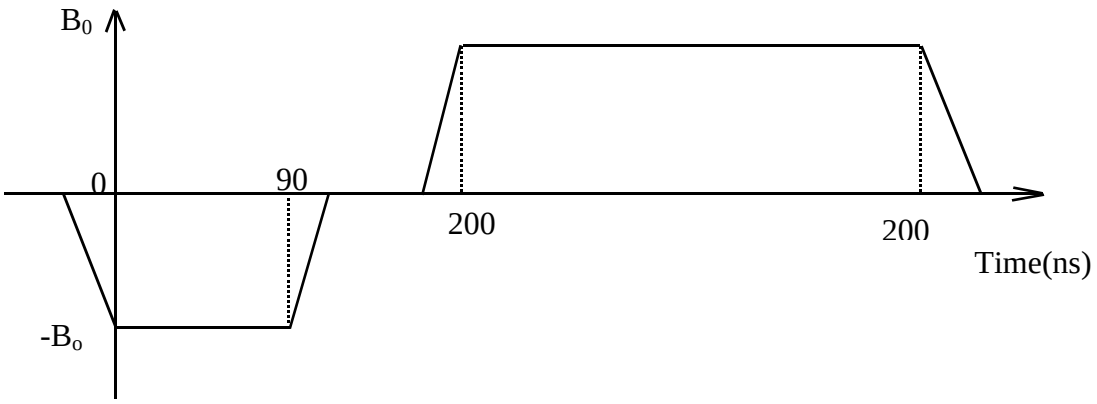

Figure 5. 18. Timing sequence of the magnetic field produced by the fast rise-time dipole.

first quadrant into n_t regions, and the edge of each region is defined by following formula

$$q_i = \begin{cases} \arcsin(k_1 i / n_t), & q < 45^o \\ \arcsin(k_2 i / n_t) & q > 45^o \end{cases}. \qquad (5.\ 10)$$

Here, i is the number of regions, n_t is the total region number. k_1 and k_2 are the empirical parameters for fine adjustment of the field. In each region, the current density distribution is sinusoidal, and we find the weighted-mean position of the current using the following formula

$$q_{i0} = \frac{\int_{q_i}^{q_{i+1}} I(q) q dq}{\int_{q_i}^{q_{i+1}} I(q) dq}. \qquad (5.\ 11)$$

In the equation, θ_{i0} is the mean position of the current in this small region, which is also the location of the conductor. θ_i and θ_{i+1} are the lower and upper edges of the ith region.

The figure of merit in the design is the uniformity of the integral of the magnetic field along z-axis. A 3-D magnetic program, Mag-PC, is used to calculate the magnetic field produced by the conductors. In the calculation, k_1 and k_2 are adjusted to obtain the best uniformity of the dipole field. Table 5.3 gives a set of conductor locations from the above formula, where k_1=0.997 and k_2=0.988 are used. The geometry of the conductor locations including the end conductors is

shown in Figure 5.19. Table 5.4 is the integrated non-uniformity of the dipole at different radius and angles. It shows that this geometry has very good uniformity comparable with the regular PC dipole.

Table 5. 3. Location of conductors in the first quadrant of fast dipole

Number of the Conductor	Angular Position of the Conductor
1	2.86^o
2	8.60^o
3	14.4^o
4	20.4^o
5	26.5^o
6	33.0^o
7	40.1^o
8	48.1^o
9	57.7^o
10	72.3^o

Table 5. 4. Deviation of integrated magnetic field from axis field of fast dipole

Angle	r/R				
	0.2	0.4	0.6	0.7	0.8
0^o	0.013%	0.045%	0.072%	0.050%	-0.012%
45^o	0.003%	0.006%	0.010%	0.049%	0.150%
90^o	0.00%	0.007%	0.140%	0.27%	0.026%

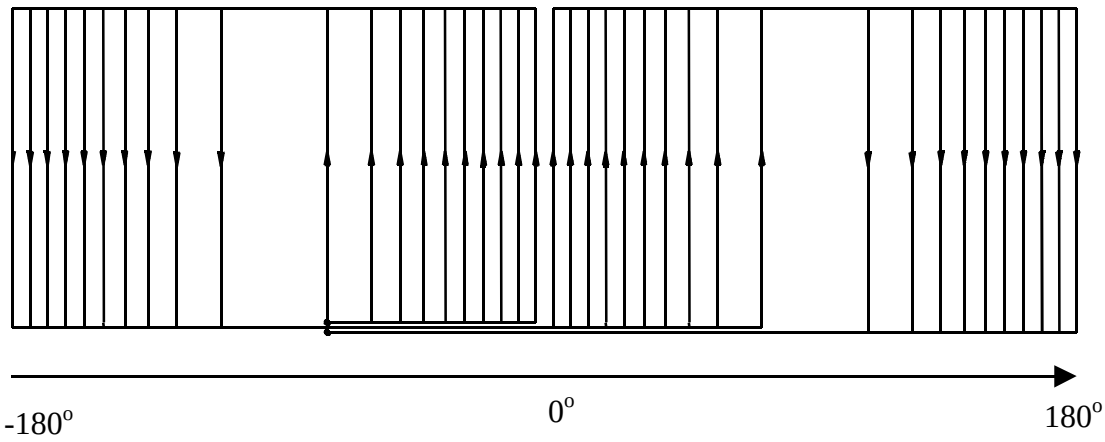

Figure 5. 19. Position of conductors along the azimuthal angle.

The inductance of this geometry is very small. Based on the two dimensional classical electrodynamics, we can estimate that the inductance of the dipole is about 1.23×10^{-7} H/m. The detailed derivation of the inductance is shown in Appendix II.

Figure 5.20 is a typical magnetic field profile on axis. The radius of the dipole is 2.5 cm and the length of the dipole is 5 cm, which yields an aspect ratio of one. The peak magnetic field of the dipole is 0.195 Gauss/A and the integrated field along the axis is 58.8 Gauss-cm.

5.3.3 Inductance and Magnetic Field Measurement of a Prototype Model

To test the inductance and the field quality of this geometry, a prototype fast dipole is made. The conductor distribution of the model is the same as in Table 5.3. But the aspect ratio is larger, which is about 1.75. To guarantee that each conductor carries the same current, there is an accurate resistor connected in series with each conductor. The total effective resistance of the dipole is 50 Ω for the matching purpose.

A low voltage testing was performed to measure the inductance of this prototype model. The circuit is shown in Figure 5.21. In the figure L and R are the inductance and resistance of the dipole respectively. A fast pulse generator drives the dipole with a fast rise-time, rectangular pulse, as shown in Figure 5.22a. The signal is picked up from the resistor and is transmitted to the scope. Due to the

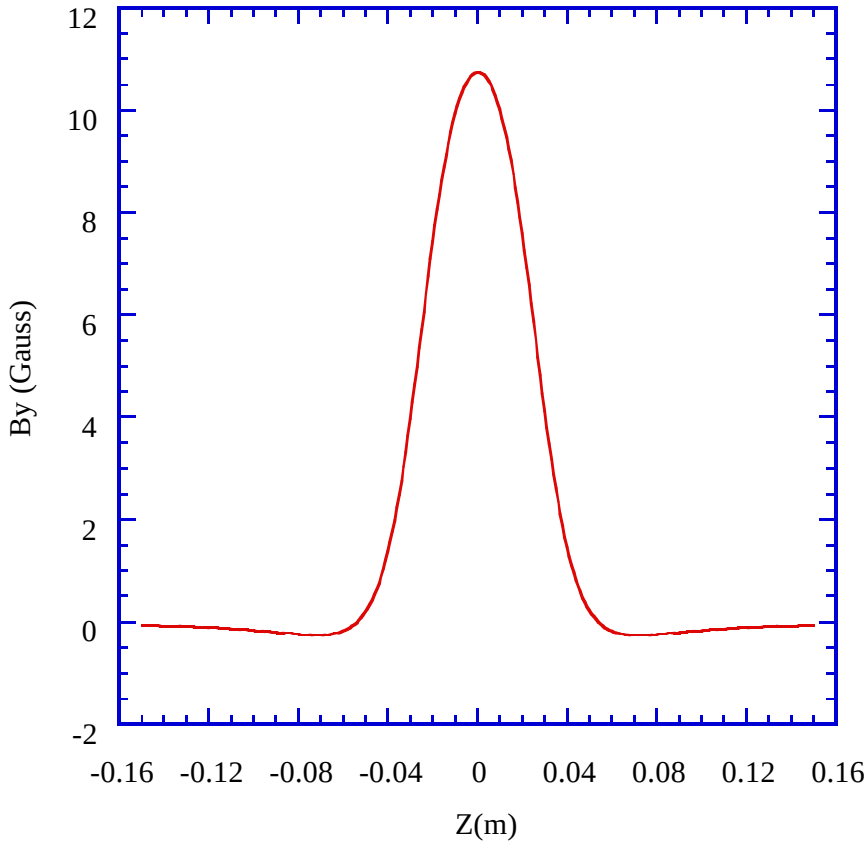

Figure 5. 20. Vertical magnetic field along the z-axis.

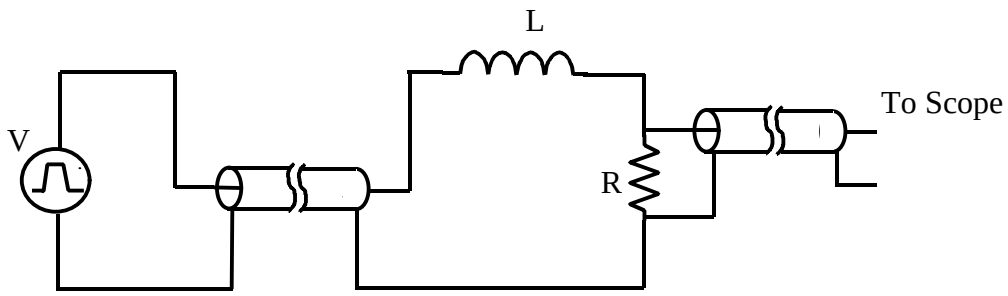

Figure 5. 21. Circuit for inductance measurement.

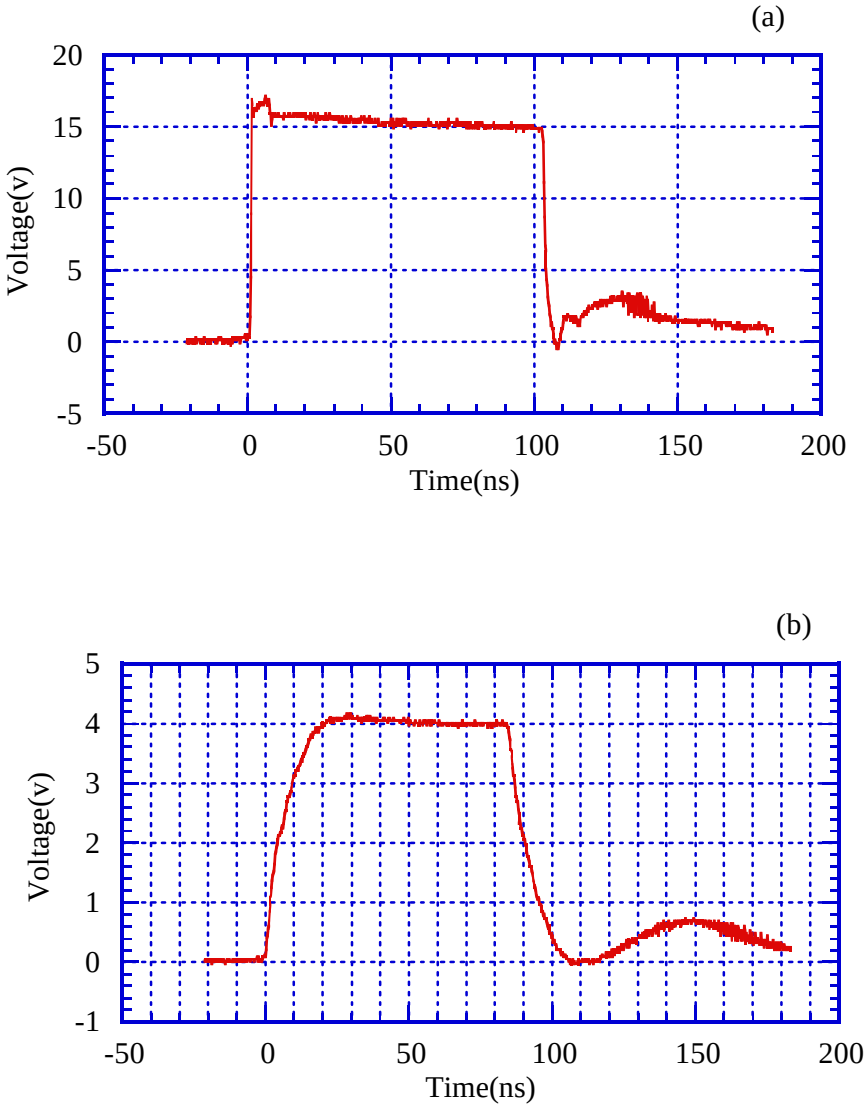

Figure 5. 22. Inductance measurement. (a) The input signal to the dipole. (b) Time response of the dipole to a rectangular impulse. The rise-time constant is about 6.3 ns.

inductance of the dipole, the rise time in the dipole is longer than the original signal. From the rise-time of the current in the dipole, we are able to measure the inductance of the dipole. Figure 5.23b shows the current signal in the dipole. The rise-time constant of the current τ is about 6.4 ns. The resistance of the circuit is 50 Ω, which yields the inductance of the dipole $L=R\tau$ is about 0.32 μH. As was discussed previously, the calculated inductance per unit length for this dipole is 1.23×10^{-7} H/m, and because we connect the four quadrants in series, the inductance is 16 times larger. The length of the dipole is 0.16 m, so the total calculated inductance of the prototype dipole is about 0.315 μH, very close to the measurement.

The measurement of the magnetic field of the dipole is tricky. Because the inductance of the dipole is so small, the magnetic field is very difficult to measure if we drive the dipole with a DC current, as we usually do. In this measurement, we use a high frequency sinusoidal signal to modulate the dipole field, and pick up the modulated field using a small coil. By using this method, we are able to measure the magnetic field as small as 20 mGauss.

Assume that we modulate the dipole magnetic field as following

$$B(t) = B_0 Sin(wt) . \qquad (5.\ 12)$$

Here, B_0 is the amplitude of the field and ω is the frequency of the signal. If we put a small probe coil with n turns into this time-varying field, the induced voltage in the probe is

$$U(t) = pr^2 nwB_0 Sin(wt) = U_0 Sin(wt), \qquad (5.13)$$

where, r is the radius of the probe, n is the turns of the probe and U_0 is the amplitude of the induced signal on the probe. By measuring the induced voltage, we are able to measure the magnetic field produced by the dipole. Figure 5.23 shows the circuit diagram of the measurement. In the figure, V_1 is a sinusoidal wave signal generator, R_1 is the effective resistance of the dipole, L_1 is the inductance of the dipole. L_2 and R_2 are the internal inductance and resistance of the probe coil. The signal is picked up from the probe directly to the scope. Table 5.5 gives the parameters for the measurement.

Table 5. 5. Experimental parameters for field measurements of fast dipole

Modulating frequency f	Coil turns	Coil inductance	Coil internal resistance	Coil radius
1.515 MHz	20	2.1μA	0.3 Ω	2.6 mm

Notice that because we use 50 Ω channel of the scope, the voltage reading in the scope is not the total voltage induced in the coil. Even though the coil resistance is very small, its reactance will affect the results at this frequency range.

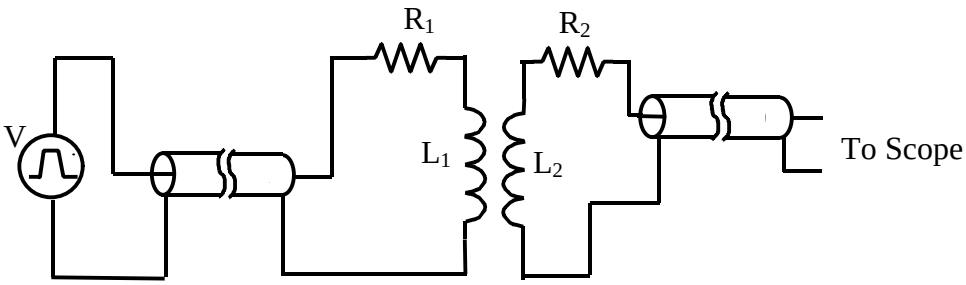

Figure 5. 23. Equivalent circuit of magnetic field measurement for fast dipole.

From Figure 5.23, we can relate the voltage on the scope to the total induced voltage by

$$U_0^{'} = U_0 * \frac{\sqrt{(R_0 + R_2)^2 + w^2 L_2^{\,2}}}{R_0}. \qquad (5.\ 13)$$

Here, R_0 is the characteristic impedance of the transmission line. If we plug the numbers into this equation, the two voltages differ by about 8%, which is noticeable in the experiment.

An experimental facility is set up to measure the magnetic field at different location of the prototype dipole. Figure 5.24 shows the magnetic field on the axis. The dots are the measurement data and the curve is the calculation from MagPC. They agree very well. Figure 5.25 gives the measurements at 0^0 and at the 0.4R and 0.68R respectively. Figure 5.26 is the measurements at 45^0 and at 0.4R and 0.68R. Figure 5.27 gives the measurement at 90^0 and at 0.4R and 0.68R. We can see at 0.68R, the agreement between the measurement and the calculation is not as good as in the small radius case.

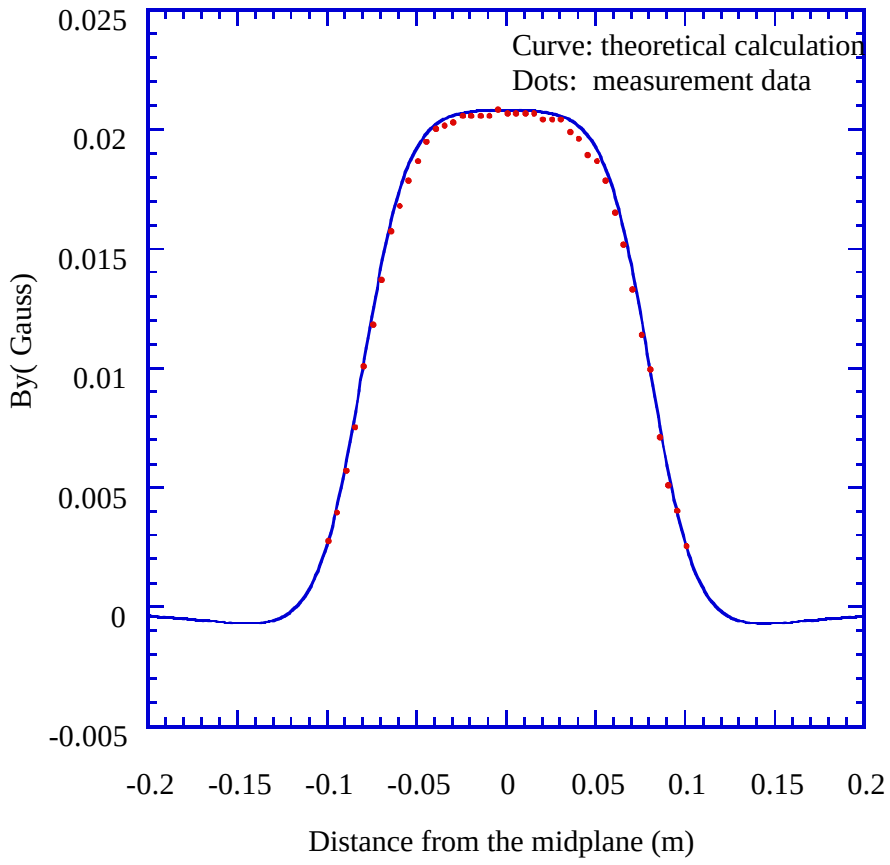

Figure 5. 24. Measurement and Mag-PC calculation of the vertical magnetic field on axis.

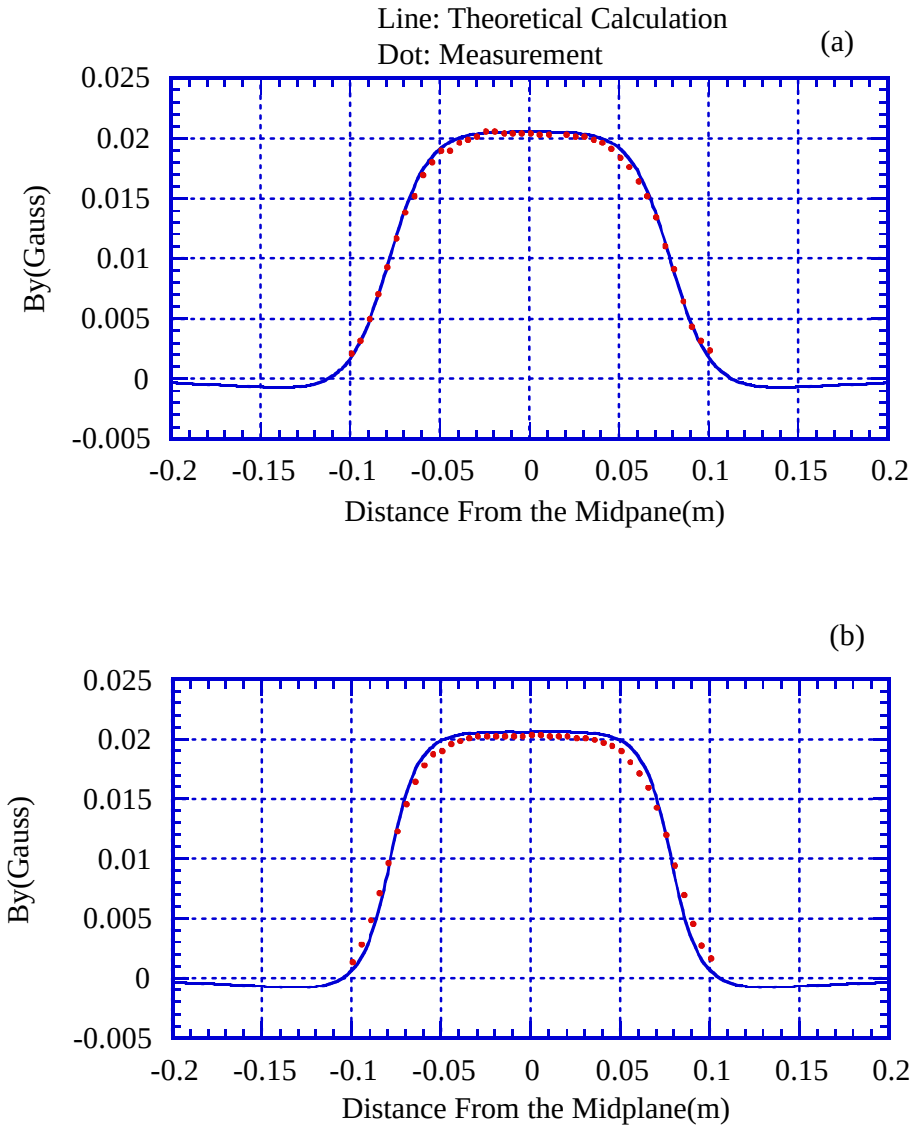

Figure 5. 25. Vertical magnetic field measurement. (a) Field measurement at 0^0 and 0.4R. (b) Field measurement at 0^0 and 0.68R.

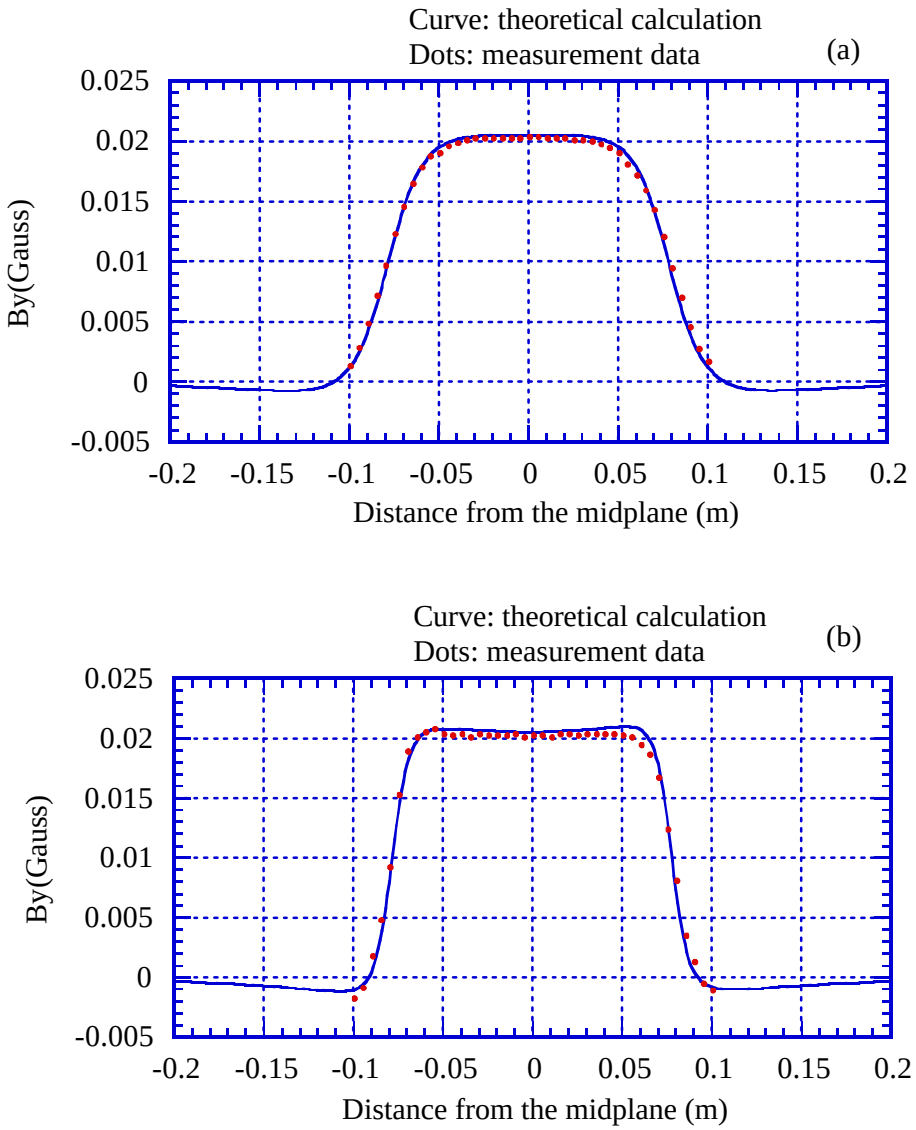

Figure 5. 26. Vertical magnetic field measurement. (a) Field measurement at 45^0 and 0.4R. (b) Field measurement at 45^0 and 0.68R.

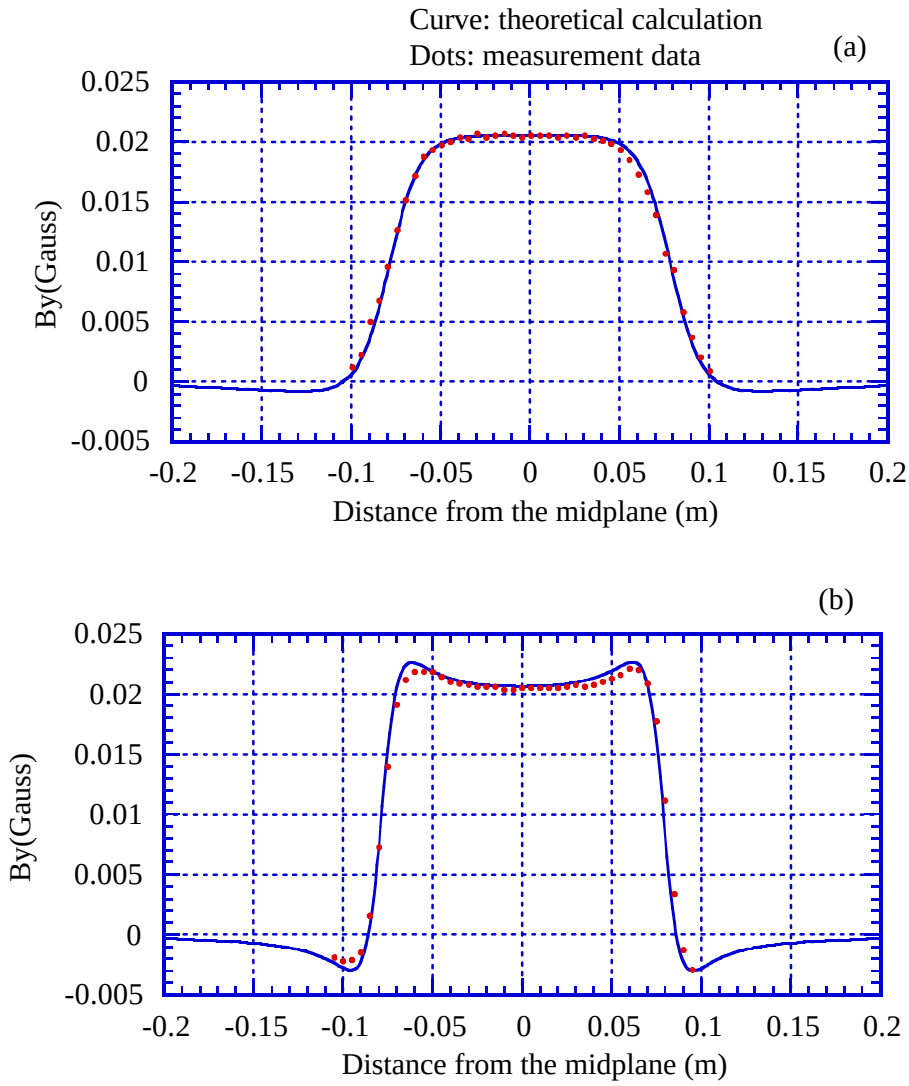

Figure 5. 27. Vertical magnetic field measurement. (a) Field measurement at 90^0 and 0.4R. (b) Field measurement at 90^0 and 0.68R.

5.4 Summary

In this chapter, the overall design of the UMER was introduced and discussed. The principle of capacitive BPM was studied and a prototype capacitive BPM was designed and tested. The test result showed that our understanding of the capacitive BPM is correct and the accuracy of the BPM is good enough to be used in the UMER. Work has also been conducted to study a fast rise-time dipole. By using the combination of parallel and series structure, we demonstrated that the rise-time and the field profile of this kind of dipole could meet the requirements of the UMER.

Chapter 6

Conclusion

Systematic and pioneering experimental work has been performed to study the resistive-wall instability of space-charge waves in space-charge dominated electron beam. In the linear regime, we were able to observe the propagation and growth or decay of space-charge waves in the resistive environment. However, in the nonlinear regime, we observed the abnormal increase of the fast wave amplitude and the growth or decaying rate of the fast waves is amplitude dependent. By doing the same experiments in the conducting wall, we demonstrated that this abnormal phenomenon only occurs in the resistive pipe. So far, there are no analytical theories or simulations that would predict this phenomenon.

The energy spread measurement of the space-charge dominated beam is a challenge and mystery in our lab. People always observed large energy spread from the beam. In this thesis, it was demonstrated that this large energy spread is due to the imperfection of the energy analyzer itself. As a consequence, a new structure of the energy analyzer was designed. Both simulation and experimental test showed that the new energy analyzer has much better resolution and can be used to characterize the energy profile of electron beam with high resolution.

So far, all the experiments were performed on a linear transport system. The short distance of the system limits a lot experiment work. UMER, which is being designed and built at the University of Maryland, will offer a much better tool to study and bench test the space-charge-dominated beam. Even if the beam only propagate by several turns, it already has a much longer transport distance than the linear system that we currently are using. To guarantee the success of the UMER, we must be able to measure the beam position accurately and steer the beam back to the orbit. A prototype capacitive BPM has been designed and bench tested. The results showed that this kind of BPM has good enough time response and accuracy for the UMER. A real BPM is being designed and will be tested.

At the junction of the injection line and the UMER main ring, we need a fast rise-time dipole to steer the beam into the ring. Some work has been performed to study a method to reduce the inductance, therefore, the rise-time, of this dipole. The test of a prototype structure of this kind of dipole showed that it is possible to reduce the inductance to the desired value by using a combination of parallel and series structure. Of course, there is a lot of engineering work to do to design a real fast dipole for the UMER.

For the future work, more experiments could be done to study the resistive-wall instability. For example, the capacitive effect on the growth rate is a very interesting topic. The experiments on the slow waves were limited due to the cathode condition. With the new cathode, more work can be done to study the

amplitude related growth rate of the slow wave. In addition, the measurement of the possible emittance growth due to resistive wall is also very interesting and challenging. After the UMER is completed, we are also able to study the beam instability due to the induction gap impedance in a much longer distance and more valuable results could be obtained.

The newly designed energy analyzer will be a promising tool to study the beam energy profile in different situations. For example, we are able to measure the energy spread increase due to the Boersch effect and the longitudinal-longitudinal relaxation effect etc.

After all, many achievements have been presented in the thesis. However, more valuable and challenging work can be done in this area with facilities already developed in our lab and with the completion of UMER.

Appendix I

Study the Higher Order Term of BPM Responses to Beam Position

From Equations

$$V_R(t) = \frac{I_b(t)\ln(b/a)}{2pev}[1 + \frac{4}{\Phi}\sum_{n=1}^{\infty}\frac{1}{n}(r/b)^n Cos(nq)Sin(\frac{n\Phi}{2})] \quad \text{(A1. 1)}$$

and

$$V_L(t) = \frac{I_b(t)\ln(b/a)}{2pev}[1 + \frac{4}{\Phi}\sum_{n=1}^{\infty}\frac{1}{n}(r/b)^n Cos(nq)Sin[n(p + \frac{\Phi}{2})]], \quad \text{(A1. 2)}$$

we can get the ratio of two voltages up to 3rd order,

$$Ln\frac{V_R}{V_L} = Ln\frac{1 + \frac{4}{f}\frac{r}{b}\cos(q)\sin(\frac{f}{2}) + \frac{4}{f}\frac{1}{2}\left(\frac{r}{b}\right)^2\cos(q)\sin(\frac{f}{2}) + \frac{4}{f}\frac{1}{3}\left(\frac{r}{b}\right)^3\cos(3q)\sin(\frac{3f}{2})}{1 - \frac{4}{f}\frac{r}{b}\cos(q)\sin(\frac{f}{2}) + \frac{4}{f}\frac{1}{2}\left(\frac{r}{b}\right)^2\cos(q)\sin(\frac{f}{2}) - \frac{4}{f}\frac{1}{3}\left(\frac{r}{b}\right)^3\cos(3q)\sin(\frac{3f}{2})} \quad \text{(A1. 3)}$$

Assume ρ=r/b is small and use the approximation

$$Ln(1+x) \approx x - \frac{x^2}{2} + \frac{x^3}{3}, \quad \text{(A1. 4)}$$

The numerator of Equation (A1.4) becomes

$$
\begin{aligned}
&Ln\left(1+\frac{4}{f}\,r\cos(q)\sin(\frac{f}{2})+\frac{4}{f}\frac{1}{2}\,r^{2}\cos(q)\sin(\frac{f}{2})+\frac{4}{f}\frac{1}{3}\,r^{3}\cos(3q)\sin(\frac{3f}{2})\right)\\
&\approx\frac{4}{f}\,r\cos(q)\sin(\frac{f}{2})+\frac{4}{f}\frac{1}{2}\,r^{2}\cos(q)\sin(\frac{f}{2})+\frac{4}{f}\frac{1}{3}\,r^{3}\cos(3q)\sin(\frac{3f}{2})\\
&-\frac{1}{2}\left(\frac{4}{f}\,r\cos(q)\sin(\frac{f}{2})+\frac{4}{f}\frac{1}{2}\,r^{2}\cos(q)\sin(\frac{f}{2})+\frac{4}{f}\frac{1}{3}\,r^{3}\cos(3q)\sin(\frac{3f}{2})\right)^{2}\\
&+\frac{1}{3}\left(\frac{4}{f}\,r\cos(q)\sin(\frac{f}{2})+\frac{4}{f}\frac{1}{2}\,r^{2}\cos(q)\sin(\frac{f}{2})+\frac{4}{f}\frac{1}{3}\,r^{3}\cos(3q)\sin(\frac{3f}{2})\right)^{3}\\
&=\frac{4}{f}\,r\cos(q)\sin(\frac{f}{2})+\frac{4}{f}\frac{1}{2}\,r^{2}\cos(q)\sin(f)+\frac{4}{f}\frac{1}{3}\,r^{3}\cos(3q)\sin(\frac{3f}{2})\\
&-\frac{1}{2}\left(\frac{4}{f}\right)^{2}\left[\,r^{2}\cos^{2}(q)\sin^{2}(\frac{2}{f})+r^{3}\cos(q)\cos(2q)\sin(\frac{2}{f})\sin(f)\,\right]\\
&+\frac{1}{3}\left(\frac{4}{f}\right)^{3}\left[\,r^{3}\cos^{3}(q)\sin^{3}(\frac{2}{f})\,\right]
\end{aligned}
$$

(A1. 5)

Similarly, the denominator of Equation (A2.3) becomes

$$
\begin{aligned}
&Ln\left(1-\frac{4}{f}\,r\cos(q)\sin(\frac{f}{2})+\frac{4}{f}\frac{1}{2}\,r^{2}\cos(q)\sin(\frac{f}{2})-\frac{4}{f}\frac{1}{3}\,r^{3}\cos(3q)\sin(\frac{3f}{2})\right)\\
&\approx-\frac{4}{f}\,r\cos(q)\sin(\frac{f}{2})+\frac{4}{f}\frac{1}{2}\,r^{2}\cos(q)\sin(f)-\frac{4}{f}\frac{1}{3}\,r^{3}\cos(3q)\sin(\frac{3f}{2})\\
&-\frac{1}{2}\left(\frac{4}{f}\right)^{2}\left[\,r^{2}\cos^{2}(q)\sin^{2}(\frac{2}{f})-r^{3}\cos(q)\cos(2q)\sin(\frac{2}{f})\sin(f)\,\right]\\
&+\frac{1}{3}\left(\frac{4}{f}\right)^{3}\left[-\,r^{3}\cos^{3}(q)\sin^{3}(\frac{2}{f})\,\right]
\end{aligned}
$$

(A1. 6)

Plug Equations (A1.5) and (A1.6) into (A1.3), we find

$$Ln\frac{V_R}{V_l} = 8\frac{\sin(\frac{f}{2})}{f} r\cos(q) + \frac{8}{3} r^3 \cos(3q)\frac{\sin(\frac{3f}{2})}{f}$$
$$-16\frac{\sin(f)\sin(\frac{f}{2})}{f^2} r^3\cos(q)\cos(2q) + \frac{128}{3}\frac{\sin^3(\frac{f}{2})}{f^3} r^3\cos^3(q)$$

(A1. 7)

Using the relationships

$r\cos(q) = x/b$,

$r^3\cos(3q) = \left(x^3 - 3xy^2\right)/b^3$,

$r^3\cos(q)\cos(2q) = \left(x^3 - xy^2\right)/b^3$, and

$r^3\cos^3(q) = x^3/b^3$,

Equation (A1.7) becomes

$$20Log\frac{V_R}{V_l} = \frac{20}{Ln10}\ln\frac{V_R}{V_L}$$
$$= \frac{160}{Ln10}\frac{\sin(\frac{f}{2})}{f}\frac{x}{b} + \frac{20}{Ln10}\left(\frac{8}{3}\frac{\sin(\frac{3f}{2})}{f} - 16\frac{\sin(f)\sin(\frac{f}{2})}{f^2} + \frac{128}{3}\frac{\sin^3(\frac{f}{2})}{f^3}\right)\frac{x^3}{b^3}$$
$$+\left(-8\frac{\sin(\frac{3f}{2})}{f} + 16\frac{\sin(f)\sin(\frac{f}{2})}{f^2}\right)\frac{xy^2}{b^3}$$

(A1. 8)

This is Equation (5.7) in Chapter 5.

Note if we want the coupling term to vanish, we let

$$-8\frac{\sin(\frac{3f}{2})}{f}+16\frac{\sin(f)\sin(\frac{f}{2})}{f^2}=0\,, \qquad \text{(A1. 9)}$$

We have ϕ=76.99^o.

Appendix II

Estimating the Inductance of the Fast Dipole

If there is a current sheet distributed on the surface of a cylinder with sinusoidal distribution, it can be expressed as following

$$J(r,f) = \frac{I}{4a}\cos fd(r-a)\hat{e}_z, \qquad \text{(A2. 1)}$$

here, I is the total current, a is the radius of the cylinder. The z-component of vector potential cab be expressed as

$$\Delta^2 A_z = -\frac{m_0 I}{4a}\cos fd(r-a). \qquad \text{(A2. 2)}$$

Using appropriate boundary condition at ρ=a, we can solve the equations in both regions. The solutions for both regions is

$$A_z = \begin{cases} \frac{am_0 I}{8} r^{-1}\cos f, & r > a \\ \frac{m_0 I}{8a} r\cos f & r < a \end{cases}. \qquad \text{(A2. 3)}$$

From A_z, we are able to find the magnetic fields in both regions. They are

$$\vec{B} = \begin{cases} -\frac{m_0 I}{8a}\hat{e}_y & r < a \\ \frac{am_0 I}{8r^2}[-Sin2f\hat{e}_x + \cos 2f\hat{e}_y] & r > a \end{cases}. \qquad \text{(A2. 4)}$$

Associated the magnetic field, the energy in the space can also be found, it is

$$W = \int_0^{2p}\int_0^{\infty} B^2/(2m_0)2prdrdf = \frac{m_0 p}{64} I^2. \qquad \text{(A2. 5)}$$

The total energy is related to the inductance of the system by

$$W = \frac{1}{2} L_0 I^2, \qquad \text{(A2. 6)}$$

here, L_0 is the inductance per unit length of the system, and I is the current. From this relation, we can find the inductance per unit length as

$$L_0 = \frac{m_0 p}{32} = 1.23\times10^{-7} \qquad (H/m) \qquad \text{(A2. 7)}$$

The dipole length D is 0.05 m, and if we connect the four quadrants in series, the total inductance of the dipole is

$$L = L_0 D \times 16 = 9.84\times10^{-8} \qquad (H) \qquad \text{(A2. 8)}$$

References

[1] M. Reiser, *Theory and Design of Charged Particle Beams* (John Wiley & Sons, Inc, New York, 1994).

[2] E. P. Lee, Nuovo Cimento, **106A** (1993).

[3] T. C. Marshall, *Free Electron Lasers* (Macmillan Pub. Co., New York, 1985).

[4] D. Kehne, Ph.D. Dissertation, Department of Electrical Engineering, University of Maryland, 1992.

[5] J. G. Wang, S. Bernal, P. Chin, *et al*., Nucl. Instr. & Meth. in Phys. Res., **A**(415) 422 (1998).

[6] J. G. Wang and M. Reiser, Phys. Plasmas, **5**(5) (1998).

[7] H. Suk, Ph.D. Dissertation, Physics Department, University of Maryland at College Park, 1996.

[8] C. K. Birdsall, G. R. Brewer, and A. V. Haeff, Proc. of The I.R.E., **41**(7) 865 (1953).

[9] M. Sarstedt, P. Herz, W. B. Kunkel, *et al*. PAC, 1995, Dallas, Texas.

[10] V. V. Aleksandrov, N. S. Dikansky, N. C. Kot, *et al*., Phys. Rev. A, **46**(10) 6628 (1992).

[11] D. Habs, J. Kramp, P. Krause, *et al*., Phys. Scr., **T22** 269 (1988).

[12] H. Poth, Phys. Rep., **196** (1990).

[13] J. G. Wang, E. Boggasch, P. Haldemann, *et al*., IEEE Tran. Elec. Dev., **37**(12) 2622 (1990).

[14] J. G. Wang, D. X. Wang, and M. Reiser, Nucl. Instr. & Meth. in Phys. Res., **A316** 112 (1992).

[15] C. K. Birdsall and J. R. Whinnery, J. Appl. Phys., **24**(3) 314 (1953).

[16] E. Lee. Proceedings of the 1981 Linear Accelerator Conference, Santa Fe, NM, 1981.

[17] D. A. Callahan, A. B. Langdon, and A. Frideman, J. Appl. Phys., **81**(8) 3398 (1997).

[18] J. G. Wang, Y. Zou, H. Suk, *et al*. PAC Conference, 1999, New York.

[19] H. Suk, J. G. Wang, Y. Zou, *et al*. PAC Conf., 1997, Vancouver.

[20] H. Suk, J. G. Wang, M. Reiser, *et al*., J. Appl. Phys., **86**(3) 1699 (1999).

[21] J. G. Wang and M. Reiser, Phys. Fluids B, **5**(7) 2286 (1993).

[22] J. G. Wang, H. Suk, and M. Reiser, Phys. Rev. Lett., **79**(6) 1042 (1997).

[23] J. G. Wang, M. Reiser, W. M. Guo, *et al*., Pat. Accel., **37-38**(181) (1992).

[24] J. G. Wang and M. Reiser. IEE Particle Accelerator Conference, 1991, San Francisco, CA.

[25] D. C. Davidson, *Theory of Nonneutral Plasmas* (Addison-Wesley, Menlo Park, CA, 1989).

[26] D. A. Callahan, Ph.D. Dissertation, University of California, DAvis, 1989.

[27] J. G. Wang, D. X. Wang, and M. Reiser, Phys. Rev. Lett., **71**(12) 1836 (1993).

[28] J. G. Wang, D. X. Wang, H. Suk, *et al*., Phys. Rev. Lett., **74**(16) 3153 (1995).

[29] V. I. Kudelainen, V. A. Lebedev, and I. N. Meshkov, Sov. Phys. JETP, **56**(6) 1191 (1982).

[30] M. Reiser, P. G. O'Shea, R. A. Kishek, *et al*. PAC Conference, 1999, New York.

[31] N. Brown, Ph.D. Dissertation, Physics Department, University of Maryland at College Park, 1995.

[32] J. A. Simpson, Rev. Sci. Instr., **32**(12) 1283 (1961).

[33] A. B. El-Kareh and M. A. Simither, Journal of applied Physics, **50**(9) 5596 (1979).

[34] A. Faltens, E. P. Lee, and S. S. Rosenblum, J. Appl. Phys., **61**(12) 5219 (1987).

[35] G. H. Jansen, *Coulomb Interactions in Particle Beams* (Academic Press, INC., Boston, 1990).

[36] M. Reiser, S. Bernal, A. Dragt, *et al*., Fus. Eng. Des., **00** (1996).

[37] T. J. Fessenden, B. W. Stallard, and G. G. Berg, Rev. Sci. Instr., **43**(12) 1789 (1972).

[38] H. Suk, J. G. Wang, S. Bernal, *et al*. PAC, 1997, Vancouver, Canada.

[39] F. J. Deadrick, J. J. Barnard, T. J. Fessenden, *et al*. PAC, 1995, Dallas, TX.

[40] T. F. Godlove, S. Bernal, and M. Reiser. PAC, 1995.

[41] A. Friedman, D. P. Grote, and I. Haber, Phys. Fluids, **B 4**(7) 2203 (1992).

[42] I. Haber, D. A. Callahan, A. Friedman, *et al*. 1995 Particle Accelerator Conference and International Conference on High-Energy Accelerators, 1995, Dallas, Texas.

[43] Y. Zou, J.G. Wang, H. Suk, M. Reiser, Accepted for publication at Phys. Rev. Lett., May 2000.

[44] C.D. Child, Phys. Rev. Ser. *I* **32**, 492 (1911).

[45] I. Langmuir, Phys. Rev. Ser. *II*, **2**, 450 (1913).